We would like to thank the reviewers for their valuable comments and suggestions. It took more time than expected to go through all of the individual points, in particular as some of them required a significant extension of our original investigations. E.g., we included additional evaluations of ceilometer data to provide consistency checks for the MAX-DOAS retrievals, as well as additional examples of synthetic data retrieval. As a consequence we want to apologize for the delay of our point to point responses.

Reply to RC1

We thank reviewer #1 for the quick response and the detailed comments. We appreciate the comments and we understand that these comments have a positive effect on the scientific content of the manuscript while improvement of the descriptions and further clarifications are necessary. We have further clarified the retrieval procedure and improved the description of the look-up table parameterization. A point to point basis response to the reviewer's comments is provided in the following for consideration. Our answers are presented in blue texts. Please note that all the page and line numbers mentioned below refer to the pages and lines in the manuscript with revision marks.

Anonymous Referee #1

Received and published: 4 September 2019

The manuscript entitled "A MAX-DOAS aerosol profile retrieval algorithm for high altitude measurements: application to measurements at Schneefernerhaus (UFS), Germany" by Wang et al. presented a new look-up table based aerosol extinction profile retrieval algorithm for MAX-DOAS observations at Schneefernerhaus (UFS), Germany. Details of the parameterization of the look-up table, retrieval procedure and error analysis are presented. In addition, the authors also investigated the sensitivity of different input parameters to the retrieval results. The new retrieval technique is applied to synthetic data for validation. The long term observations of aerosol optical depth are also validated by comparing to sun-photometer measurements. The validated MAX-DOAS measurements are then used to investigate the temporal variation of aerosol at UFS. The manuscript is in general well organized and scientifically interesting for the community. Therefore, I recommend publishing the manuscript after addressed the following comments.

Sect.1 para 2: the authors summarize the main methodologies for aerosol monitoring, however, these mentioned AERONET, Lidar and MAX-DOAS are very different in the measured parameters, detection range, etc. I suggest the authors could introduce a little bit about the measured aerosol

parameters of these methods, and their advantages and disadvantages for aerosol monitoring.

Response: We have added brief comments to these measurement instruments in Sect. 1 Para. 2 (see Page 2, Lines 25-30).

Sect. 2.2: the sun-photometer measured AOD were interpolated to obtain the AOD at 360 nm and 477 nm. Which kind of the interpolate method? Linear or non-linear? Any large difference due to different interpolate method?

Response: The data were interpolated following the Angström exponent method. As the AODs at 360 and 477 nm were both interpolated from the data at two nearby wavelengths (340 & 380 nm and 440 & 500 nm, respectively), the difference due to different interpolation method is expected to be small. We have compared our results with the data derived using linear interpolation. For most of the data, the difference is less than 1%. We have supplemented the information about data interpolation in Sect. 2.2 (see Page 5, Line 20).

Why only time period between10:00-14:00 UTC and stable aerosol abundance were considered?

Response: It is because the calibration uncertainty is very high under low SZA. This has been further clarified in the text (see Page 5, Line 21).

What does the intensity means in P.5 L.2?

Response: It means (spectral) radiances. This has been clarified in the text (see Page 5, Line 23).

The aerosol optical properties required for MAX-DOAS inversion were collected from the AERONET site at Hohenpeißenberg. It is located at an altitude of 980 m and approximately 43 km north of the UFS. As the authors introduced, the aerosol vary strongly with time and location. How to estimate the uncertainties on the retrieved results due to the difference of aerosol optical properties between Hohenpeißenberg and UFS site?

Response: We realize the different aerosol optical properties between UFS and Hohenpeißenberg. Therefore, we examined the sensitivity of O_4 DSCD to aerosol optical properties, and the influence was estimated to be less than 3%. Some other studies also showed that aerosol optical properties only show a small (1.5-4%) impact on the retrieval of aerosol extinction profiles (e.g. Chan et al., 2019). We have supplemented this information to Sect 2.2 Para. 2 (see Page 5, Line 34 to Pate 6, Line 3).

Sect. 3.1: How the DOAS fit windows were determined? Are they based on sensitivity analysis? Please clarify.

Response: The fit windows were determined according to both the absorption signal of O_4 and the SNR of our spectrometers. We have added some explanations in Sect 3.1 (see Page 8, Lines 4-11).

How about the performance of spectral analysis? The levels of RMS and SCD errors? Any filtering for O_4 DSCDs was applied before being introduced to the retrieval scheme?

Response: We have added further descriptions about the performance of spectral analysis in Sect 3.1 (see Page 8, Lines 20-23). The results with residual RMS larger than 10^{-3} are filtered out. This is also supplemented in Sect. 3.1 (see Page 8, Lines 19-20).

Please add a reference to QDOAS: http://uvvis.aeronomie.be/software/QDOAS/

Response: The reference has been supplemented in Sect 3.1 Para. 1 (see Page 7, Line 33).

Sect. 3.3: How did the authors obtain the topography? And how did the authors distinguish snow or rock and vegetation? Is it taken from a digital elevation map (DEM) and albedo map? Please clarify.

Response: Both the altitude data and surface type are obtained from Google Earth. This has been clarified in the caption of Fig. 2 and Sect. 3.3 (see Page 10, Fig. 2 and Line 9).

How to define the pseudo-reality topography usingTRACY-2?

Response: This is described in Sect. 3.3 Para. 4 (see Page 10, Lines 8-14).

What's kind of the parameters were included in the pseudo-reality topography?

Response: These are described in Sect. 3.3 Para. 5 (see Page 10, Line 19 to Page 11, Line 1).

It would be useful to compare radiative transfer simulation results from the two radiative transfer models with the same setting to quantify the differences between the two models.

Response: We have supplemented the comparison result in Sect. 3.3 Para. 3 (see Page 10, Lines 5-7).

Sect. 3.5: It is difficult to understand the parameterization of aerosol extinction coefficient in Table 3. Please clarify.

Response: The description of the parameterization has been refined (see Pages 14-15).

I also think the vertical resolution of retrieval is very coarse in the design of the look-up table, in particularly compared with other ground based MAX-DOAS studies.

Response: The parameterization is based on the measurement sensitivity. Because the information content of the measurements is rather limited, a finer vertical grid would not really improve the accuracy of the retrieval, but would greatly increase the complexity as well as computational effort. In most of the OEM-based MAX-DOAS studies, although their vertical resolution is higher (usually 200 m per layer), the degree of freedom of the signal (DFS) is usually around 2. In addition, the vertical variation of the aerosol extinction at the UFS is expected to be low. Therefore, a coarse resolution setting would be sufficient. This information is supplemented in Sect. 3.5 (see Page 14, Lines 12-15).

Btw, there is only one sub-section of 3.5, I do not suggest to use the title of 3.5.1.

Response: These two sections have been rearranged as Sect. 3.5 and 3.6 (see Pages 14-17).

Sect. 3.6: What's the DOAS fitting error? How to evaluate it? There are so many sub-titles. In my opinion, 3.6.1 and 3.6.2 can be grouped as the errors on measured O4 DSCDs, while 3.6.3-3.6.6 can be regarded as the errors on simulated O4 DSCDs. So I suggest to re-organized this part.

Response: We have clarified the definition of the DOAS fitting error in the text. This section (now Sect. 3.7) has been rearranged following the reviewer's suggestion (see Pages 17-20).

Sect. 4.4, p. 26, l. 5-6: Any explanation about the seasonal pattern of AOD that higher in summer and lower in winter?

Response: This is explained in Sect 4.5 Para. 1 (see Page 36, Lines 15-16). It can be explained by the higher biogenic emissions in summer, as well as the stronger vertical transport of aerosols.

Also the systematic underestimation of MAX-DOAS AOD? Could the authors can present the co-located ceilometer observations or lidar measurements nearby to certificate the vertical structure of aerosol extinction?

Response: We have supplemented the ceilometer results in Sect. 2.3 (see Page 6, Fig. 1 and Page 7, Lines 13-16). The results indicate that the aerosols above 2 km contribute 30-50% to the total AOD. As the MAX-DOAS reports AOD only up to 2 km, an underestimation of total AOD is expected.

Please also discuss the possible reason for the high ratio of aerosol extinction coefficient between 360 and 477 nm in summer than in the other seasons.

Response: This is explained in Sect. 4.5 Para. 2-3 (see Page 36, Line 21 to Page 38, Line 7). It indicates that the particle size is smaller in summer.

Sect. 5: The conclusion is mostly repeating the results, please consider shorten the entire summary and conclusion section.

Response: We have shortened this section (see Page 38, Line 9 to Page 40, Line 3).

Minor comments: p. 6, l. 2-3: Did the authors observe any seasonal pattern of cloud cover? It might be important for the later analysis of aerosol temporal variation.

Response: We have supplemented a summary of the cloud screening results in Sect. 3.2 (see Page 8, Lines 31-34 and Page 9, Table 2). The percentage of cloudy measurements is highest in summer (67%) and lowest in winter (54%).

p. 7, l. 6: Which radiative transfer model the authors are referring to? Please clarify.

Response: It refers to LIDORT. This has been clarified in the text (see Page 9, Lines 8-9).

p. 9, l. 11: Please define all the terms in the equation.

Response: The missing definition of ΔS_s has been supplemented (see Page 15, Line 29).

p. 13, l. 10: I don't understand why should the surface albedo error dependent on aerosol profile?

Response: Maybe the previous description was a bit misleading. We have revised the description of Sect. 3.7.2 to avoid confusion (see Page 18, Line 31 to Page 19, Line 4).

p. 14, l. 9-13: If the authors already consider the error caused by aerosol above the retrieval height, then why the error bar of Fig. 9 still do not overlap with the sun-photometer observations most of the time?

Response: This is only a source of error that we consider in the retrieval, but the MAX-DOAS AOD in Fig. 9 only represents the AOD under 2 km. We have further clarified this issue in the text (see Page 17, Lines 3-4).

p. 17, l. 4-10: Radiative transfer model error also play a role in the discrepancy between measurement and simulation. Please revise the statement.

Response: We have revised the description (see Page 24, Line 1).

The elevation dependent O4 scaling factor also introduced in other studies, e.g. Irie et al., 2015; Zhang et al., 2019. Please review and cite.

Response: We have supplemented the two references (see Page 24, Lines 5-7).

p. 25, fig. 9: The error bars do not overlap with the sun-photometer measurements most of the time indicated that there are some significant error sources are not consider in the error analysis. Please clarify.

Response: The main reason is that the MAX-DOAS AOD only represents the AOD under 2 km. This has been further clarified in the text (see Page 34, Line 33 to Page 35, Line 2).

p. 27, fig. 11: As mentioned before, cloud screening also play a role in the analysis, it is important to indicate the number of valid measurement used in the calculation.

Response: We have supplemented a summary of the cloud screening results in Sect. 3.2. The numbers of valid measurements are listed in Table 2 (see Page 9).

Reference:

Chan, K. L., Wang, Z., Ding, A., Heue, K.-P., Shen, Y., Wang, J., Zhang, F., Shi, Y., Hao, N., and Wenig, M.: MAX-DOAS measurements of tropospheric NO2 and HCHO in Nanjing and a comparison to ozone monitoring instrument observations, Atmospheric Chemistry and Physics, 19, 10 051–10 071, https://doi.org/10.5194/acp-19-10051-2019, https://www.atmos-chem-phys.net/19/10051/2019/, 2019.

Reply to RC2

We thank reviewer #2 for the detailed comments. These comments are useful for use to improve the quality of the manuscript. We have supplemented a more examples of synthetic data retrieval to support our statements. In addition, we have further evaluated the retrieved MAX-DOAS aerosol profile by comparing to ceilometer measurements. We have addressed the reviewers' comments on a point to point basis as below for consideration. Our answers are presented in blue texts. Please note that all the page and line numbers mentioned below refer to the pages and lines in the manuscript with revision marks.

Anonymous Referee #2

Received and published: 4 September 2019

General comments

Wang et al. introduce a new MAX-DOAS aerosol profiling algorithm for high altitude sites. The algorithm itself is based on a parameterized approach using a pre-calculated look-up table and is optimized to retrieve profiles from data measured at high altitudes. The authors include an extensive sensitivity study and discuss the most important errors thoroughly. Furthermore, an attempt to validate the performance of the algorithm with ancillary measurements is shown. The AMTD version of this manuscript was also added with one retrieval example of synthetic data and the comparison with an OEM algorithm.

First of all, I would like to comment that the manuscript has improved considerably since the first submission. Unfortunately, my main concern from the first manuscript assessment is still valid. The validation part and the retrieval of synthetic data is not enough to show that this algorithm is not only capable of retrieving accurate profiles but performs better than state-of-the-art OEM algorithms at high altitudes (as the authors claim). In order to solve this issue, I suggest to extend the

corresponding sections with the following tests:

1. The retrieval test of synthetic data (Section 4.3) should be complemented with further examples (different exponential profiles and elevated profiles).

Response: We have supplemented two more examples with different profile shapes, one exponential profile, and the other profile with a weak elevated layer. The result shows that our retrieval method can reproduce the true profiles within the measurement error. In addition, the synthetic data were also retrieved by an OEM based algorithm. The results are shown for reference. This result is supplemented in Sect. 4.3 (see Pages 32-34).

2. Comparisons of retrieved profiles with Ceilometer profiles should be added as well. This could be done in an additional section or with similarly averaged Ceilometer profiles in Fig. 10.

Response: We have supplemented the ceilometer results in Sect. 2.3. The ceilometer reports attenuated backscatter, while the MAX-DOAS measures aerosol extinction coefficients. As these parameters are not directly comparable, we have converted ceilometer measurement of attenuated backscatter profiles to aerosol extinction profiles using auxiliary AOD information from the co-located sun photometer. The ceilometer data and the comparison result are shown in Sect. 2.3 (see Pages 6-7).

3. Fig. 3, 6 and 7 are shown for one example only. It would be interesting to see how the depicted parameters look like for a not so ideal profile retrieval (e.g. smaller (larger) RAA (SZA) or different profile shapes).

Response: We have supplemented a few more examples with a smaller SZA and a larger RAA. The new results are shown in Fig. 5 (Page 20), Fig. 9 (Page 29) and Fig. 11 (Page 30).

Specific comments

P1, L4-5 and P3, L20-23 and P28, L22-23: The authors claim that commonly used MAX-DOAS algorithms are not suitable for profile retrievals at high altitudes. Since this is neither shown properly in this manuscript nor do the authors cite a publication which addresses this issue, I think that these sentences should be reworded or removed (see also comment to **Section 4.3**).

Response: We have revised the sentences (see Page 1, Lines 5-7, Page 3, Lines 31-34 and Page 38, Lines 14-16). In addition, we have added more examples of synthetic data retrieval. The retrieval of the synthetic data presented in Sect. 4.3 suggested that OEM-based retrievals cannot fully reproduce the true profile. The new results are shown in Sect. 4.3 (see Pages 32-34).

P3, L29: area → areas?

Response: This typo has been corrected (see Page 4, Line 7).

P4, L15-16: "The exposure time and number of scans of each measurement are adjusted automatically (...)." Could you please explain what the automatic adjustment of the number of scans of each measurement means?

Response: We have supplemented the information in Sect. 2.1 (see Page 4, Line 32 to Page 5, Line 4).

P5, L5-6: "(...) the derivation of Angström exponents is critical and thus omitted." If this is critical, why is it omitted? In Section 4.5, you derive Angström exponents from MAX-DOAS results. It appears inconsistent to me that Angström exponents are only discussed from MAX-DOAS alone without validating with sun photometer results. This is even more problematic as you found that the MAX-DOAS AODs are much smaller than the sun photometer results (when the AOD lower 0.02 is the main reason for the omission). You could also compare with AERONET data in case the derivation from the available sun photometer is problematic.

Response: We are sorry for the confusion. As the uncertainty of the AOD measured by the sun photometer is relatively large, the uncertainty of the derived Angström exponent would be further amplified. Consequently, the Angström exponent is not very reliable, and this is the reason, that they are not discussed in the results. We have supplemented the explanation to Sect. 2.2 (see Page 5, Lines 26-28).

P5, L13: preformed → performed

Response: This typo has been corrected (see Page 8, Line 1).

P7, L19-20: Which phase function and SSA values were used for the simulations? Which climatology was used?

Response: We have supplemented the definitions (see Page 10, Line 20 to Page 11, Line 1).

Section 3.5: Which climatology was used for the LUT creation? Are different pressure and temperature conditions/profiles are taken into account (in addition to the cross section temperature discussion)?

Response: We used the US Standard climatology (Anderson et al., 1986). We have supplemented this information in the text (see Page 17, Table 5). The variation of atmospheric profile (i.e. temperature and pressure) is not considered in the look-up table, while we consider this effect as 'other possible error sources' in the error estimation of the retrieval. We have done a sensitivity analysis with summer and winter atmospheric profiles to estimate the uncertainty related to temperature and pressure variation. We estimated the corresponding uncertainty is less than 2% which is well covered by the 'other possible error sources'. We have supplemented the discussion about this issue in Sect. 3.7.4 (see Page 21, Line 20 to Page 22, Line 3).

P10, L6: A fixed median phase function was used for the LUT but Fig. 3 and Section B3 tell me that it is quite important to use a proper phase function (especially for small RAA). Do you plan to add more dimensions to the LUT for different phase functions or how do you deal with this problem?

Response: Since accurate estimation of phase function is in general not available, it is not feasible to add phase function as an additional dimension. We have further clarified in Sect. 3.6 that only well-known input parameters are defined as dimensions of the look-up table (see Page 15, Line 30).

P11, L22: ceiometer → ceilometer

Response: This typo has been corrected (see Page 15, Line 11).

P13, L11-12: "(...) we found that O_4 DSCD at 5°is almost negatively correlated with AOD." This is new for me. Could you please show this in a plot (maybe in the appendix)? Something only valid for high altitude sites?

Response: Theoretically, aerosol reduces the optical path length for off-zenith measurements in the atmosphere due to enhanced Mie scattering, and the optical path is expected to be the longest under pure Rayleigh atmosphere. Therefore, O_4 DSCD is expected to reduce with enhanced

aerosol load. Fig. 1 show the correlation between O4 DSCD at 5° and AOD (0-2 km) for all the profiles in the look-up table (SZA = SAA = 60°). In each chart, the trend line is derived by moving average, and the *r* value is the Pearson correlation coefficient between the original data and the expected values obtained from the trend line. We have revised the description in Sect. 3.7.2 (see Page 18, Line 31 to Page 19, Line 4).

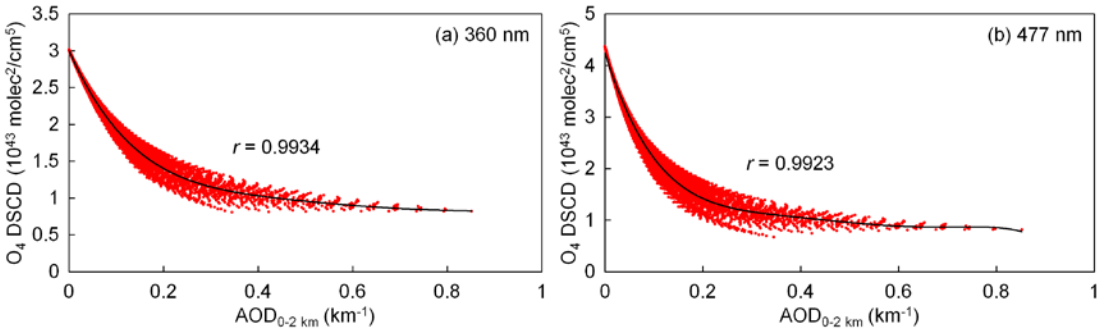

Fig. 1: Correlation between O4 DSCD at 5° and AOD (0-2 km) for all the profiles in the look-up table (SZA = SAA = 60°).

Fig. 3 Please add SZA and RAA values to the description of your example cycle as it is used throughout the manuscript.

Response: We have added SZA and RAA values to the captions of the figures (see Page 20, Fig. 5, Page 21, Fig. 6, Page 25, Fig. 7, Page 26, Fig. 8, Page 29, Figs. 9 and 10, Page 30, Fig. 11 and Page 31, Fig. 12).

P16, L14-15: "This is because the a priori profile is not needed in our retrieval algorithm". To be more accurate, you include a priori assumptions of aerosols above retrieval height in your total uncertainty. Furthermore, since your layer σ_3 and σ_2 depend on σ_1 you have another constrain for your solution which could be understood as a priori information. The question is how do you account for this kind of uncertainty?

Response: Maybe our description was confusing. In the profile set, we excluded profiles with strong elevated layers, but the aerosol extinction in different layers is independent in the retrieval. We have refined the description of the look-up table in Sect. 3.5 to make it easier to be understood (see Page 14, Line 17 to Page 15, Line 21).

P16, L17: In χ^2<1.5M, is M the number of LOS? From an OEM point of view, more LOS mean usually

a higher information content. But for your approach, more LOS mean a larger χ^2 criterium and therefore more possible profiles in your weighted mean calculation. Could you please explain this issue?

Response: Yes, M is the number of elevation angles, which is defined in the text (see Page 22, Line 19). According to the definition of χ^2, when M increases, χ^2 would also increase. Therefore, the criterion is not really changed. This is also the case for the stopping criterion of the OEM retrievals. For more details, please refer to Rodger, 2000.

Section 4.3: Please add information on the used OEM algorithm and the RTM including parametrization of the OEM retrieval (e.g the definition of a priori and measurement covariance matrices, climatology, vertical grid...). Maybe in a table? The OEM solutions do not seem to be constrained enough (too many oscillations).
Furthermore, box-like true profiles would also be problematic for lower altitude sites and higher AODs due to the a priori smoothing. Please add also a retrieval for an exponential true profile (an elevated true profile would also be interesting). One problem arises by saying that the shown true profile (nearly box-like) is representative for UFS but you use an exponential a priori profile for the OEM. Since the a priori profile is the best (first) guess of the true atmosphere, an exponential profile is insufficient here (in contrast to typical retrievals in the PBL). A better a priori would be a Boltzman distribution or maybe an exponential profile with an even larger scaling height.

Response: We have supplemented two more examples of synthetic data retrieval, one with an exponential profile and one with an elevated layer. The retrieval settings are also supplemented (see Page 34, Lines 5-14). Compared to the previous version, we set a stronger constraint to the a priori profile for the OEM retrieval. However, further optimization of the OEM retrieval is beyond the scope of this paper.

Additionally, please add a graph showing the simulated and retrieved DSCD including an RMS value of the difference between both DSCD as I don't think that the noise-free OEM solutions are that bad but might describe the measurement well.

Response: The simulated and retrieved DSCDs as well as the RMS of the difference are shown in Fig. 2. Since the manuscript is already very long and the OEM retrieval is not the main focus of the paper, we only briefly summarized the results in the text (see Page 34, Lines 17-18) without showing the plots in the manuscript.

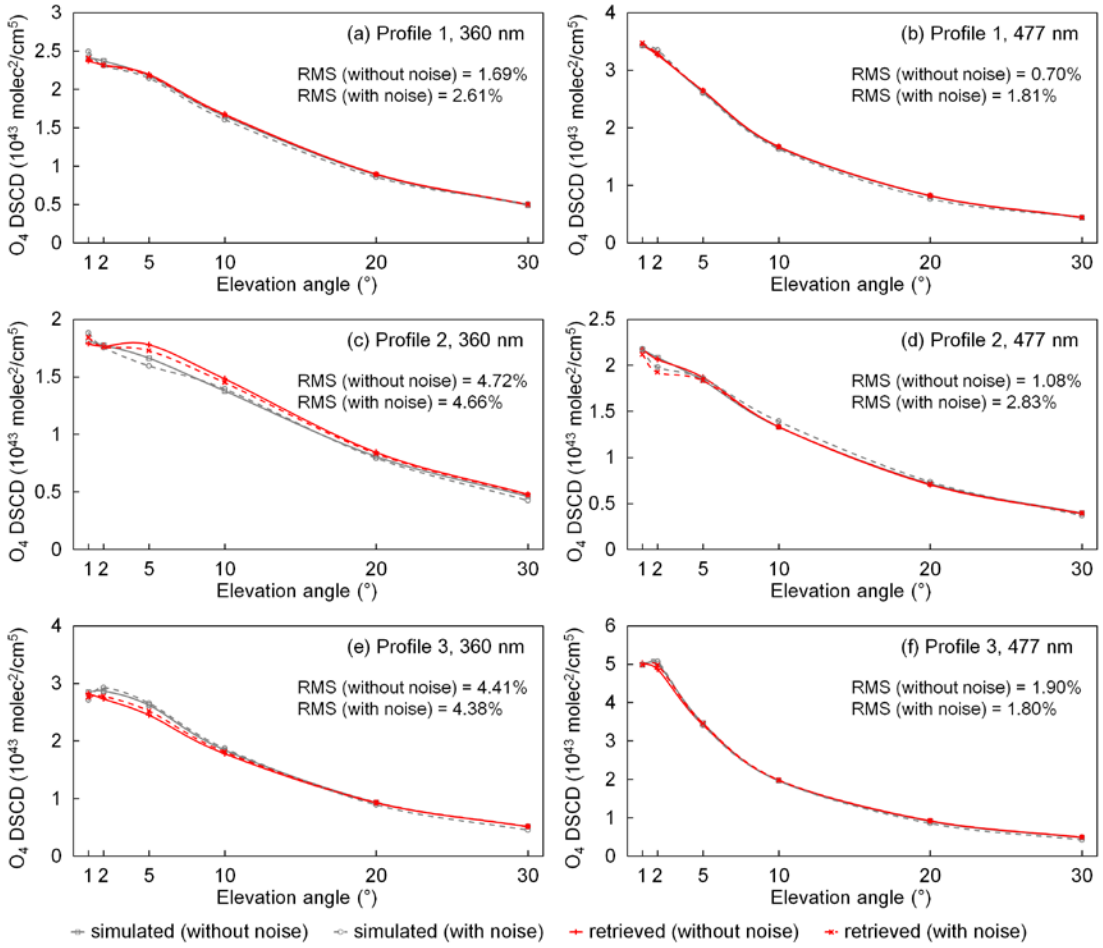

Fig 2. Simulated and retrieved DSCDs and the RMS for the symthetic study.

Section 4.4 and Fig. 9: The reason for such a large difference between sun photometer and MAX-DOAS AOD is still unclear to me. I agree that aerosols in higher altitudes might be responsible for a difference but this is true as well for measurements in the PBL. But here, the introduction of a scaling factor leads to a much better agreement. The relative amount of aerosols in altitudes higher than 2km might be responsible but this is just a guess without prove. Could the authors please take a look at the Ceilometer profiles to solve this issue (see also the following comment for Fig.10)?

Response: From the averaged ceilometer profiles we observed that there are significant amounts of aerosols above the MAX-DOAS retrieval height, see Fig. 1. The results indicate that the aerosols above the retrieval height contribute 30-50% to the total AOD. We have supplemented this result in Sect 2.3 (see Page 7, Lines 15-16).

Furthermore, which kind of scaling factor (SF) is needed to bring the MAX-DOAS AOD to the sun photometer level and how large is the difference to the actually applied SF? Is there also a clear seasonal pattern in your SF? If yes, maybe your way of how to retrieve LOS depending SF is not

optimal?

Response: As we assume that the scaling factors are constant (for each elevation angle), it is impossible to derive a scaling factor which can bring the MAX-DOAS measurements to the sun photometer observations for all conditions. In addition, since the scaling factors were derived based on a huge amount of data and the AOD varies within a relatively narrow range in a single season, data within a single season are insufficient to derive a representative scaling factor. For example, our determination method for the scaling factors at high elevation angles requires measurements under low aerosol load (AOD<0.03), but such measurements are not available in summer. Therefore, it is not feasible to derive a seasonal pattern of the scaling factors. We have further clarified in Sect. 3.9 (see Page 26, Lines 9-10).

Fig. 10: Please add also similarly averaged Ceilometer profiles and an error range for your profiles. Since a validation instrument is available, a comparison should be shown. The ceilometer backscattering signal could be scaled with the sun photometer AOD (see e.g. Wagner et al. 2019 for details). With this kind of comparison you could also assess how much aerosol is located at even higher altitudes than 2km.

Response: Please note, that the retrieval of the AOD from ceilometer data is *per se* not possible, at least with a sufficient accuracy to allow a strict validation. To cover the reviewer's point, we can however use ceilometer measurements for a consistency check by considering the paper suggested by the reviewer: we have supplemented the ceilometer profiles scaled using the method described in Wagner et al. 2019 in Fig. 1, and also supplemented error ranges for Fig. 15 (Fig. 10 in the discussion paper). The ceilometer profiles show that the aerosols above retrieval height contribute in the order of 30-50% to the total AOD. This explains the differences between MAX-DOAS and sun photometer AODs. This result was supplemented in Sect 4.4 (see Page 34, Line 32 to Page 35, Line 1).

Section 4.5: See comment to **P5, L5-6**.

Response: The uncertainty of AOD measured by sun photometer is relatively large, and the deviation of Angström exponent would further amplify the uncertainty. We have clarified in Sect. 2.2 (see Page 5, Lines 26-28).

P29, L6: profile → profiles

Response: This typo has been corrected (see Page 38, Line 22).

Appendix B: Here, important information are missing. For example, when you use aerosols in B1, which SSA and phase function is used? In B3 which SSA? In general, which climatology.

Response: We have supplemented the settings in the text (see Page 41, Lines 11-14 and Page 42, Table B1).

P34, L8-9: "using phase functions from Hohenpreißenberg should not have a significant impact on the aerosol retrieval". But the results are only shown for RAA = SZA = 60°. For other geometries it might be important to have an accurate phase function. Especially since you show in Figure 3 that the phase function is one of the largest error sources.

Response: Fig. B3 only shows an example. In our retrieval, the error caused by phase function is estimated using a look-up table which considered all possible solar and viewing geometries. We have revised the description in Sect. B3 (see Page 45, Lines 12-13).

P35, L5-6: the averaging kernels (...) are all close to zero at the altitudes above 2km. That is correct but OEM based aerosol retrievals are iterative approaches which might still get an elevated layer more or less correct even though the kernels look like that. The sensitivity in these altitudes is lower for sure but if there is a dominant elevated aerosol layer, your retrieval is not capable of retrieving it accurately due to the dependencies of the individual layers while OEM algorithms might find an accurate solution (see also comment to **Section 4.3** for a test of an elevated layer).

Response: Our look-up table does not consider extreme cases, i.e. strong elevated layers, as the measurement site is located at a high altitude (2650 m a.s.l.), strong elevated layer is typically either close to our instrument or above the retrieval height. Strong elevated layers can also be included in the look-up table if it is used for the retrieval of aerosol profiles at low altitude sites. In order to reduce computational efforts, we have limited the formulations of the look-up table with only weak elevated layers. On the other hand, the retrieval of the synthetic data showed that OEM based retrieval cannot fully reproduce the elevated layer, either (see Page 32, Fig. 13). We have revised the descriptions in Sect. 3.5 (see Pages 14-15).

References:

Anderson, G. P., Clough, S. A., Kneizys, F., Chetwynd, J. H., and Shettle, E. P.: AFGL atmospheric constituent

profiles (0.120 km), Tech. rep., AIR FORCE GEOPHYSICS LAB HANSCOM AFB MA, 1986.

Chan, K. L., Wang, Z., Ding, A., Heue, K.-P., Shen, Y., Wang, J., Zhang, F., Shi, Y., Hao, N., and Wenig, M.: MAX-DOAS measurements of tropospheric NO2 and HCHO in Nanjing and a comparison to ozone monitoring instrument observations, Atmospheric Chemistry and Physics, 19, 10 051–10 071, https://doi.org/10.5194/acp-19-10051-2019, https://www.atmos-chem-phys.net/19/10051/2019/, 2019.

Rodgers, C. D.: Inverse methods for atmospheric sounding: Theory and pr

A MAX-DOAS aerosol profile retrieval algorithm for high altitude measurements: application to measurements at Schneefernerhaus (UFS), Germany

Zhuoru Wang[1, 2], Ka Lok Chan[1], Klaus-Peter Heue[1], Adrian Doicu[1], Thomas Wagner[3], Robert Holla[4], and Matthias Wiegner[5]

[1]Remote Sensing Technology Institute, German Aerospace Center (DLR), Oberpfaffenhofen, Germany
[2]Faculty of Civil, Geo and Environmental Engineering, Technical University of Munich (TUM), Munich, Germany
[3]Max Planck Institute for Chemistry, Mainz, Germany
[4]German Meteorological Office (DWD), Hohenpeißenberg, Germany
[5]Meteorological Institute, Ludwig Maximilian University of Munich (LMU), Munich, Germany

Correspondence: Ka Lok Chan (ka.chan@dlr.de)

Abstract. We present a new aerosol extinction profile retrieval algorithm for Multi-AXis Differential Optical Absorption Spectroscopy (MAX-DOAS) measurements at high altitude sites. The ~~study~~ algorithm is based on the look-up table method. It is applied to retrieve aerosol extinction profiles from the long-term ~~measurement~~ MAX-DOAS measurements (February 2012 to February 2016) at the Environmental Research Station Schneefernerhaus (UFS), Germany, (47.417°N, 10.980°E) which is located near the summit of Zugspitze ~~,~~ at an altitude of 2,650 m. ~~Due to the low signal to noise ratio, commonly used MAX-DOAS retrieval algorithms based on the optimal estimation method are not suitable for the retrieval of high altitude measurements. We developed a new retrieval algorithm using an O_4 differential slant column density (DSCD) look-up table.~~ The look-up table consists of simulated O_4 ~~DSCDs~~ differential slant column densities (DSCDs) corresponding to numerous possible aerosol extinction profiles. The sensitivities of O_4 absorption to several parameters were investigated for the design and parameterization of the look-up table. In the retrieval, ~~the~~ simulated O_4 DSCDs for each possible profile are derived by interpolating the look-up table to the observation geometries. The cost functions are calculated for each aerosol profile in the look-up table based on the simulated O_4 DSCDs, the O_4 DSCD observations as well as the measurement uncertainties. Valid profiles are selected from all the possible profiles according to the cost function, and the optimal solution is defined as the weighted mean of all the valid profiles. A comprehensive error analysis is performed to better estimate the total uncertainty. Based on the assumption that the look-up table covers all ~~the~~ possible profiles under clear sky conditions, we determined a set of O_4 DSCD scaling factors for different elevation angles and wavelengths. The ~~dependence of the scaling factors on elevation angle might be partly related to the specific properties of the high altitude station, e.g. the highly structured topography, horizontal gradients of the aerosol extinction and the systematic dependence of the surface albedo on altitude. The~~ profiles retrieved from synthetic measurement data can ~~well reproduce the true profileand the retrieval shows good stability~~ reproduce the synthetic profile. The result also shows that the retrieval is insensitive to measurement noise, indicating the retrieval is robust and stable. The aerosol optical depths (AODs) retrieved from the long-term ~~measurement~~ measurements are compared to ~~coincident~~ coinciding and co-located sun photometer observations. High correlation coefficients (R) of 0.733 and 0.798 are found for measurements at

360 and 477 nm, respectively. However, especially in summer the sun photometer AODs are systematically higher than the MAX-DOAS retrievals by a factor of ~2. The discrepancy might be related to the limited measurement range of the MAX-DOAS, and is probably also related to the decreased sensitivity of the MAX-DOAS measurements at higher altitudes. The MAX-DOAS measurements indicate the aerosol extinction decreases with increasing altitude during all seasons, which agrees with the co-located ceilometer measurements. Our results also show maximum AOD and maximum Ångström exponent in summer which is consistent with observations from an AERONET station located ~43 km of the MAX-DOAS.

1 Introduction

Atmospheric aerosols play an important role in the atmospheric physics and chemistry. They affect the atmospheric radiation budget by absorbing and scattering radiation, as well as providing nuclei for the formation of clouds (Haywood and Boucher, 2000; Bellouin et al., 2005; Li and Kou, 2011; Heald et al., 2014). Aerosols also have significant impacts on global climate change, local air quality and visibility (Bäumer et al., 2008; Levy II et al., 2013; Viana et al., 2014). Moreover, exposure to atmospheric aerosols can be harmful to human health (Valavanidis et al., 2008; Brook et al., 2010; Karanasiou et al., 2012). Besides primary aerosols which are directly introduced into the atmosphere, aerosols can also be secondarily formed through chemical reactions (Hinds, 2012). A significant increasing amount of anthropogenic aerosols and precursors have been released into the atmosphere since the industrial revolution (Liu et al., 1991; Junker and Liousse, 2008) which becomes a widely concerned environmental problem in recent years. Aerosols can be long-range transported and hence influence regions far from the sources (Wiegner et al., 2011; Almeida-Silva et al., 2013; Lee et al., 2013; Zhang et al., 2014; Chan and Chan, 2017; Chan, 2017; Chan et al., 2018). The properties and vertical distribution of aerosols vary strongly with time and location. Therefore, it is important to measure the spatial and temporal variations of aerosols for the better understanding of the role of aerosols in atmospheric processes. In addition, anthropogenic contribution to atmospheric aerosol load is one of the largest uncertainties in climate forcing assessments. Accurate measurements of aerosol optical properties are necessary for the further assessment of environmental and radiative effects of aerosols (Stocker et al., 2013).

Methodologies for aerosol monitoring are mature and well established: the backbone is certainly the AERONET network of sun photometers (Holben et al., 1998) providing e.g. the spectral aerosol optical depth (AOD) from direct sun observations. They might be complemented by active lidar remote sensing to provide range-resolved information. The latter includes research lidars (e.g., Pappalardo et al., 2014) and networks of ceilometers (e.g., Wiegner et al., 2014; Cazorla et al., 2017). These measurements provide – depending on the complexity of the system – the vertical distribution of the particle backscatter and extinction coefficient at typically one to three wavelengths with a very high vertical resolution in the order of 10 m, however, the uncertainty of the retrieved AOD is larger than that of sun photometers due to the restrictions of the measurement range. In the case of ceilometers inherent assumptions of the data evaluation further add to the uncertainty. Recently, the potential of Multi-AXis Differential Optical Absorption Spectroscopy (MAX-DOAS) for range-resolved aerosol retrievals was investigated as well (Platt and Stutz, 2008; Wagner et al., 2004; Frieß et al., 2006).

Ground-based MAX-DOAS is a remote sensing technique for measuring atmospheric aerosols and trace gases. MAX-DOAS instruments measure the spectra of scattered sunlight at several different viewing directions, and information of trace gas absorption along the light paths can be obtained by applying the differential optical absorption spectroscopy (DOAS) method to the ultraviolet-visible (UV-VIS) band. The retrieval of ~~aerosols~~ aerosol extinction profiles from MAX-DOAS measurements typically relies on the absorption signal of oxygen collision complex (O_4). As the vertical distribution profile of O_4 is well-known and stable, it is an ideal indicator ~~for~~ of the atmospheric distribution of photon paths. Photon paths of scattered sunlight can be influenced by aerosols and hence change the measured O_4 slant columns. Therefore, aerosol vertical extinction profiles can be retrieved by fitting the O_4 observations to radiative transfer simulations. Since the experimental setup is relative simple and inexpensive, ~~it has~~ MAX-DOAS instruments have been widely used to measure the vertical distribution of atmospheric aerosols and trace gases in the past two decades (e.g., Hönninger et al., 2004; Irie et al., 2008; Li et al., 2010; Clémer et al., 2010; Frieß et al., 2011; Halla et al., 2011; Irie et al., 2011; Vlemmix et al., 2011; Wagner et al., 2011; Li et al., 2013; Ma et al., 2013; Wang et al., 2014a; Chan et al., 2015; Jin et al., 2016; Wang et al., 2016; Chan et al., 2017).

In the retrieval of vertical profile information from MAX-DOAS measurements, the aerosol profile is usually regarded as the state vector ($\boldsymbol{x}$) and the measured O_4 differential slant column densities (DSCDs) of each scanning cycle are regarded as the measurement vector ($\boldsymbol{y}$). The radiative transfer model used to simulate the O_4 DSCDs is regarded as the forward model ($\boldsymbol{F}$). As the radiative transfer in the atmosphere is non-linear, the retrieval is a non-linear problem. Moreover, the retrieval is ill-posed, which means the information contained in the observation is insufficient to determine a unique solution. In many of the other MAX-DOAS studies (e.g., Frieß et al., 2006; Clémer et al., 2010; Frieß et al., 2011; Irie et al., 2011; Wang et al., 2014a, 2016; Chan et al., 2017), aerosol profiles are retrieved using the optimal estimation method (OEM) (Rodgers, 2000). The inversion of the aerosol profile is solved iteratively by minimizing the cost function. Vertical profile information can also be retrieved from MAX-DOAS observations using parameterized approaches (e.g., Lee et al., 2009; Li et al., 2010; Vlemmix et al., 2011; Wagner et al., 2011; Sinreich et al., 2013). These methods simplifies aerosol profiles ~~with~~ as limited parameters, e.g., aerosol optical depth (AOD), layer height, shape parameter and etc. (Wagner et al., 2011; Hartl and Wenig, 2013). The optimal solution is usually determined by minimizing the difference between simulations and measurements.

However, as the retrieval is ill-posed and errors exist in both ~~measurement and simulation~~measurements and simulations, the profile with the lowest cost function may not be the one closest to the true profile. Moreover, in the typical ~~OEM based~~ OEM-based algorithms, the iteration stops as soon as the cost function is smaller than a certain threshold. Therefore, the retrieved profile is not necessarily the one with the smallest cost function. At high altitude sites, the aerosol profile retrieval is more challenging, as the O_4 concentration ~~as well as~~ and the aerosol load ~~is~~ are both much lower than ~~at typical~~ that at low altitude sites. The vertical gradient of the aerosol extinction is also much smaller and the relative ~~contributions~~ contribution from aerosols above the retrieval height to the total AOD ~~are~~ is more significant. As a result, the signal to noise ratio (SNR) of ~~such~~ high altitude MAX-DOAS ~~measurement is often insufficient to get a stable retrieval . Therefore, it is necessary to develop a dedicated MAX-DOAS aerosol profile retrieval algorithm for high altitude sites.~~ measurements is much lower and hence affects the retrieval quality.

In this paper, we present a new MAX-DOAS aerosol profile retrieval algorithm ~~dedicated~~ suitable for high altitude measurements. It is based on an O_4 DSCD look-up table. The look-up table includes simulated O_4 DSCDs corresponding to a very large number of aerosol extinction profiles. Our retrieval algorithm is applied to MAX-DOAS observations at the Environmental Research Station Schneefernerhaus (Umweltforschungsstation Schneefernerhaus, UFS). The UFS is located close to the summit of Zugspitze (~~2962~~2,962 m above sea level), the highest mountain of Germany, at an altitude of 2,650 m. The O_4 concentration at Zugspitze is ~40% lower compared to ~~sea-level~~sea level. As the measurement site is surrounded by the mountainous area of the Alps and far from polluted ~~area~~areas, the aerosol load is much lower than at low altitude sites. The annual averaged AOD measured by the sun photometer at the UFS is around 0.1 at ~~350–500~~350 – 500 nm. Moreover, the surface around the UFS is very complex which complicates the radiative transfer simulation. As a result, the model errors are larger compared to the flat and simple surfaces. In the study, we first analyzed the simulation uncertainty caused by the simplification of topography definition (see Section 3.3). Then we studied the sensitivity of O_4 absorption to several parameters (see Section 3.4 and Appendix B). Based on the results, we designed the O_4 DSCD look-up table ~~(see Section 3.6). The error estimation and inversion method are presented in the following sections.~~ and the inversion method (see Sections 3.5 to 3.8). In Section 3.9, we present our method for determining the O_4 DSCD scaling factors based on the look-up table. Discussions of the retrieved aerosol profiles from the long-term measurements at the UFS are presented in Section 4.

2 Measurements

2.1 MAX-DOAS measurements

The MAX-DOAS instrument ~~was~~ is set up on the platform on the 5th floor of the UFS (47.417°N, 10.980°E), about 20 m above ground level which is about 2,650 m about sea level. The instrument consists of a scanning telescope, a stepping motor ~~controlling~~ which controls the viewing zenith angle of the telescope~~and~~ , as well as two spectrometers covering ~~both~~ ultraviolet (UV) and visible (VIS) wavelength bands. ~~Scattered sunlight collected by the telescope~~ Incoming sunlight is redirected by a prism reflector and a quartz fiber bundle to the spectrometers for spectral analysis. The field of view (FOV) of the instrument is about 0.95°. Two spectrometers (OMT Instruments, OMT ctf-60) each equipped with a CCD detector ~~were used to cover~~ are used to measure the spectra of both UV (320 – 478 nm) and VIS (427 – 649 nm) wavelength ranges. The full width half maximum (FWHM) spectral resolutions of the UV and VIS spectrometers are about 1.0 and 0.6 nm, respectively. The scanning direction of the telescope is controlled by the stepping motor.

As the ~~scanning~~ measurement geometry is limited by the topography, the viewing azimuth angle of the telescope was adjusted to the due south (180°) with the lowest elevation angle of 1°. ~~A measurement sequence~~ Each scanning cycle consists of measurements ~~of scattered sunlight spectrum~~ at elevation angles (α) of 90° (zenith), 30°, 20°, 10°, 5°, 2° and 1°. ~~The exposure time and number of scans of each measurement are adjusted automatically depending on the intensity of received scattered sunlight in order to achieve similar intensity levels for all the measurements. A full measurement sequence takes about~~ A single measurement at each elevation angle lasts for ~1 min, and a full scanning cycle takes about 10 ~~min.~~ min. The recorded spectrum of each measurement is the sum of the CCD readouts within ~1 min. In order to optimize the measurement

SNR, avoid saturation and achieve a constant signal level, the data acquisition software automatically adjusts the exposure time of each readout to make the maximum count close to 70% of saturation level (65,535 counts). Depending on the intensity of received light, the exposure time of each readout varies from tens of milliseconds to a few seconds. The measurements of UV and VIS bands are taken by the two spectrometers simultaneously, but their exposure times are adjusted individually. The instrument takes measurements continuously during daytime (solar zenith angle (SZA) < 85°), but during the noon (175° < solar azimuth angle (SAA) <185°) and twilight periods (85° < SZA < 92°), the instrument takes only zenith measurements.

The MAX-DOAS instrument is running since February ~~2012 until present.~~ 2012. However, the measurement was interrupted between February 2013 and July 2013 due to instrument maintenance. In February 2016, the measurement was interrupted again and the VIS spectrometer was found to be degraded. In this paper, we present four years of MAX-DOAS measurements from February 2012 to February 2016.

2.2 Sun photometer measurements

Next to the MAX-DOAS instrument, a sun photometer ~~was~~ is installed at the UFS, which provides measurements of ~~radiative intensities~~ radiances at 12 wavelengths between 340 and 1640 nm with a temporal resolution of 1 s. The instrument was developed at the Meteorological Institute of Ludwig Maximilian University of Munich (LMU) based on a system operated in the framework of the SAMUM campaigns (Toledano et al., 2009, 2011) but with improved electronics and data acquisition developed by Physikalische Messsysteme Ltd. In this study, the AODs ~~measured by the sun photometer~~ derived from sun photometer measurements applying the well-established Rayleigh calibration method were used for the inter-comparison with the MAX-DOAS retrieval. ~~The AOD was determined applying the well-established Rayleigh calibration method.~~ For this purpose, AOD measurements at 340 and 380 nm were interpolated to 360 nm while AODs at 477 nm were interpolated from the measurements at 440 and 500 nm. The interpolation followed the Ångström exponent method. Measurements were given as hourly averages~~in the time period~~. Due to the reduced accuracy under large SZA, only the measurements between 10:00 ~~UTC~~ and 14:00 UTC ~~. Only~~ each day were used. In order to ensure the data quality, only cloud-free conditions and periods of stable aerosol abundance (variability of ~~intensities~~ radiances below 5% within one hour) were considered. These requirements reduce the number of available sun photometer measurements considerably. Note ~~,~~ that the AOD is often below 0.02 at the relevant wavelengths with an uncertainty in the order of ±0.015 due to calibration errors, Rayleigh correction ~~, or radiometric accuracyin the order of ±0.015. As a consequence the derivation of~~ and radiometric accuracy. As the uncertainty of the AOD measured by the sun photometer is relatively large, the uncertainty of the Ångström ~~exponents is critical and thus omitted.~~ exponent would be further amplified. Consequently they are not used in this study.

Aerosol optical properties not available from UFS-measurements but required for our MAX-DOAS inversion scheme (single scattering albedo and phase function) were estimated from the AERONET measurements at Hohenpeißenberg, which is located at an altitude of 980 m and approximately 43 km north of the UFS. ~~These optical properties~~ The AERONET data were available at 440, 675, 870 and ~~1020~~1,020 nm, therefore, the data at 360 nm were extrapolated, and the data at 477 nm were interpolated. As Hohenpeißenberg and UFS are located at different altitudes, the aerosol optical properties might be slightly different. Therefore, we have analyzed the uncertainties caused by the differences in single scattering albedo and phase functions through

a sensitivity analysis. The result shows that the influences of aerosol optical properties are in general less than 3%, see Appendix B3. Some other MAX-DOAS studies also found that aerosol optical properties show only small impacts on aerosol profile retrieval (e.g., Chan et al., 2019).

3 ~~Data analysis~~

2.1 Ceilometer measurements

2.2 ~~Spectral analysis~~

The UFS is also equipped with a Lufft (previously Jenoptik) ceilometer (model: CHM15kx, see Wiegner and Geiß (2012)) operated by the German Weather Service (DWD). Ceilometers are single-wavelength backscatter lidars, and the received signals follow the well-known lidar equation (Wiegner et al., 2014). The CHM15kx is eye-safe and fully automated which allows unattended 24/7 operation. It can be used to monitor aerosol layers (e.g., volcanic ash, see Schäfer et al. (2011)), validating meteorological and chemistry transport models (see, e.g., Emeis et al. (2011)), and is foreseen for model assimilation (e.g., Wang et al., 2014b; Warren et al., 2018; Chan et al., 2018).

The ~~calibration of the spectrometers was preformed by fitting the measured solar spectra to the literature solar reference (Chance and Kurucz, 2010). All the measured spectra were first corrected for offset and dark current. The DOAS technique (Platt et al., 1979; Platt and Stutz, 2008) was applied to two wavelength ranges (338~~CHM15kx ceilometer is equipped with a diode-pumped Nd:YAG laser emitting laser pulses at 1,064 ~~–~~nm. The received backscatter signals are stored in 1,024 range bins with a resolution of 15 ~~370 nm for UV spectra and 440~~m. The temporal resolution is set to 15 ~~–~~s. The signals are corrected for incomplete overlap by a correction function provided by the manufacturer.

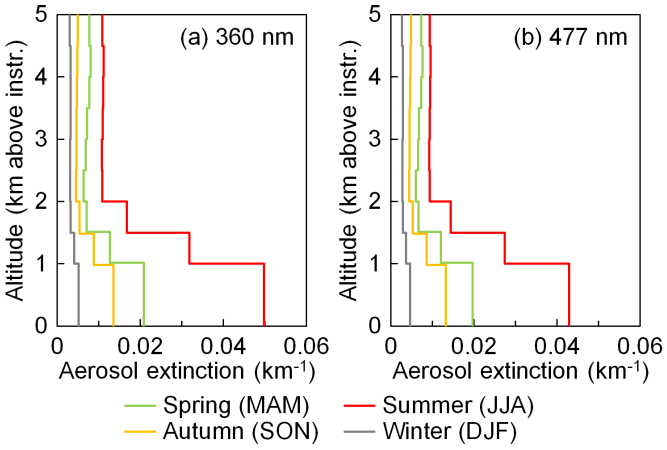

Figure 1. Seasonal average aerosol extinction profiles extracted from ceilometer measurements.

A strict retrieval of the particle extinction coefficient from ceilometer measurements is not possible due to the unknown lidar ratio; furthermore, exploitation of the signal in the range of incomplete overlap is subject to errors. Thus, in order to convert the ceilometer measurements to aerosol extinction profiles, we followed an approach mentioned in Wagner et al. (2019). The range corrected attenuated backscatter data from July 2016 to December 2017 were seasonally averaged. Data of the altitude between 500 ~~490~~m and 5 ~~nm for VIS spectra)each with strong~~ km above instrument were averaged with a vertical grid resolution of 500 m. Data below 500 m were assumed to be constant, following the values at 500 m. The extinction coefficients were first calculated by scaling the attenuated backscatter profiles (β^*) to the seasonal average AODs at 360 and 477 nm obtained from the sun photometer. The extinction profiles were then used to correct for the attenuation of the backscatter profiles following the lidar equation (Klett, 1981; Fernald, 1984). The corrected backscatter profiles (β) were then scaled to the AODs at 360 and 477 nm measured by the sun photometer to obtain the extinction profiles, see Fig. 1. Note that the ceilometer measures at 1,064 nm and the optical properties of aerosols depend on the wavelength. Therefore, the uncertainties of these profiles are very large and they should be considered as qualitative only.

The results shown in Fig. 1 indicate that the aerosol load at the UFS is highest in summer (June, July and August) and lowest in winter (December, January and February). The seasonal results also indicate large variations of the aerosol load from the surface up to 2 km. Above 2 km the variability is smaller, however, their contribution to the total column is still substantial (~30 – 50%).

3 Aerosol profile retrieval method

In this study, we developed an aerosol profile retrieval algorithm for MAX-DOAS measurements based on the look-up table method. According to the measurement sensitivity, we first parameterized the aerosol profile as the aerosol extinction coefficients of three altitude layers and defined a profile set which is assumed to include all possible profiles. O_4 DSCDs corresponding to each profile in the set were simulated and stored in the look-up table. In the retrieval, O_4 ~~absorption signal to retrieve the~~ DSCDs are calculated from the measured spectra and then compared to the simulated ones corresponding to each profile of the set using a cost function. According to the cost function, valid profiles are selected from the set, and the optimal solution is defined as the weighted mean of all the valid profiles.

3.1 O_4 DSCD calculation

The DSCDs of O_4 ~~. The~~ were derived from both UV and VIS spectra using the DOAS technique (Platt et al., 1979; Platt and Stutz, 2008). In the retrieval, DSCD is defined as the difference between the slant column ~~densities (SCDs) of the~~ density (SCD) of each off-zenith spectrum ($\alpha \neq 90°$) and the corresponding zenith reference spectrum ($\alpha = 90°$). ~~For each scanning cycle, the zenith spectra before and after the cycle were temporally interpolated to the measurement time of each off-zenith spectrum . The broad band spectral structures caused by Rayleigh and Mie scattering were removed by including a low order polynomial in the DOAS fit. Absorption cross sections of several trace gases as well as a synthetic ring spectrum were included in the DOAS fit.~~ The QDOAS spectrum analysis software (version 3.2) developed by BIRA-IASB (http://uv-vis.aeronomie.be/software/QDOAS/)

was used for the spectral fitting analysis. The calibration of the spectrometers was performed by fitting the measured solar spectra to the literature solar reference (Chance and Kurucz, 2010). All the measured spectra were first corrected for offset and dark current.

Details of the DOAS fit settings for both bands are listed in Table 1. The fitting windows were determined according to both the absorption signal of O_4 and the SNR of the spectrometers. For UV spectra, the fitting window is 338 – 370 nm, which is the same as most of the other MAX-DOAS studies (e.g., Clémer et al., 2010; Wang et al., 2014a; Kreher et al., 2019), and it covers the strong absorption peak at 360.8 nm and a weak absorption peak at 344 nm. For VIS spectra, because the spectral range of the spectrometer begins at 427 nm and the SNR close to the spectral edges is low, we therefore adapted a smaller fitting window of 440 – 490 nm, which is a bit narrower than the fitting window of 425 – 490 nm commonly used in other MAX-DOAS studies (e.g., Clémer et al., 2010; Chan et al., 2017; Kreher et al., 2019). The VIS fitting window covers the strong absorption peak at 477 nm and a weak absorption peak at 446.5 nm. As the temperature at the UFS typically varies between 263 K and 279 K (Risius et al., 2015), trace gas absorption cross sections measured at 273 K were used in the DOAS fit. Absorption cross sections of several trace gases as well as a synthetic ring spectrum were included in the DOAS fit. For each scanning cycle, the zenith spectra before and after the cycle were temporally interpolated to the measurement time of each off-zenith spectrum. The broad band spectral structures caused by Rayleigh and Mie scattering were removed by including a low order polynomial in the DOAS fit. Small shift and squeeze of the wavelengths were allowed in the wavelength mapping process in order to compensate small uncertainties caused by the instability of the spectrograph. ~~In this study, the spectra evaluation software QDOAS (version 3.2) developed by BIRA-IASB was used for the spectral fitting analysis.~~

The root mean square (RMS) of fit residual was used to evaluate the performance of the DOAS fit. DSCDs with residual RMS larger than 1×10^{-3} were not considered in the following analysis. Under cloud-free condition, the residual RMS of most of the UV spectra varies between 5×10^{-4} and 9×10^{-4}, while the residual RMS of most of the VIS spectra varies between 2×10^{-4} and 5×10^{-4}. This is because both the light intensity and the O_4 absorption are stronger at the VIS band, hence the measurement SNR is higher.

3.2 Cloud screening

The aerosol profile retrieval requires the forward simulation of the radiative transfer in the atmosphere. As the radiative transfer is rather complicated for cloudy sky condition, the forward simulation usually assumes a cloud-free atmosphere. The aerosol retrieval might result in large uncertainty under cloudy or foggy conditions. Therefore, it is important to filter out the measurements taken under cloudy or foggy conditions. In this study, a colour index (CI) (Wagner et al., 2014, 2016) based cloud screening approach was applied to filter out cloudy measurements. The CI is defined as the ratio of radiative intensities at 330 and 390 nm in this study. Larger CI indicates the UV/VIS intensity ratio is higher, hence, the sky is more blue. Our cloud screening method is presented in Appendix A. ~~Based on our approach, ~~The cloud screening results during the entire measurement period are summarized in Table 2. Among the four seasons, the percentage of cloudy measurements is highest in summer and lowest in winter. In total, about 60% of the zenith measurements were determined as cloudy scenes, and the corresponding scanning cycles were not used in the ~~following analysis~~aerosol profile retrieval.

Table 1. The DOAS fit settings for UV (338 – 370 nm) and VIS (440 – 490 nm) bands.

Species	Temperature	Fitting window		Reference
		338 – 370 nm (UV)	440 – 490 nm (VIS)	
CHOCHO	296 K		✓	Volkamer et al. (2005)
HCHO	273 K	✓		Chance and Orphal (2011)
H_2O	296 K	✓	✓	HITEMP 2010, Rothman et al. (2010)
NO_2 [(a)]	273 K	✓	✓	Bogumil et al. (2003)
NO_2 [(a)]	220 K	✓	✓	Bogumil et al. (2003)
O_3 [(b)]	273 K	✓	✓	Serdyuchenko et al. (2014)
O_3 [(b)]	223 K	✓	✓	Serdyuchenko et al. (2014)
O_4	293 K	✓	✓	Thalman and Volkamer (2013)
Ring		✓	✓	Chance and Spurr (1997)
Polynomial		5^{th} order	5^{th} order	
Intensity offset		linear	linear	

[(a)] I_0 correction is applied with SCD of 10^{17} molec/cm^2 (Aliwell et al., 2002).

[(b)] I_0 correction is applied with SCD of 10^{20} molec/cm^2 (Aliwell et al., 2002).

Table 2. Summary of cloud screening results.

Season	Number of measurements	Number of cloudy measurements	Percentage of cloudy measurements
Spring (Mar, Apr, May)	17,728	10,677	60.2%
Summer (Jun, Jul, Aug)	21,360	14,259	66.8%
Autumn (Sep, Oct, Nov)	24,259	13,519	55.8%
Winter (Dec, Jan, Feb)	17,007	9,264	54.5%
Annual	80,354	47,719	59.4%

3.3 Topography effect and the simplification in radiative transfer model

The topography around the UFS is quite complex, which complicates the radiative transfer simulations. As shown in Fig. 2~~shows the topography under the viewing direction of the MAX-DOAS. The~~ , the surface altitude varies between 600 and 2,800 m a.s.l. along the viewing direction of the MAX-DOAS instrument. ~~Surface types include~~ Fig. 2 also shows the type of surface in different colours which includes forests, meadows, rocks, etc. Some parts of the surface are seasonally or permanently covered by snow, while some steep slopes cannot be covered by snow even in winter.

Three-dimensional radiative transfer models (RTMs) can consider such a complex terrain, but they are computational expensive and unaffordable for retrieval. Due to the limitation of ~~our RTM~~ the two-dimensional RTM LIDORT (Spurr et al., 2001; Spurr, 2008) us in the study, we simplified the ground topography to a flat surface at an altitude of 2,650 m a.s.l ~~. when calculating the look-up~~

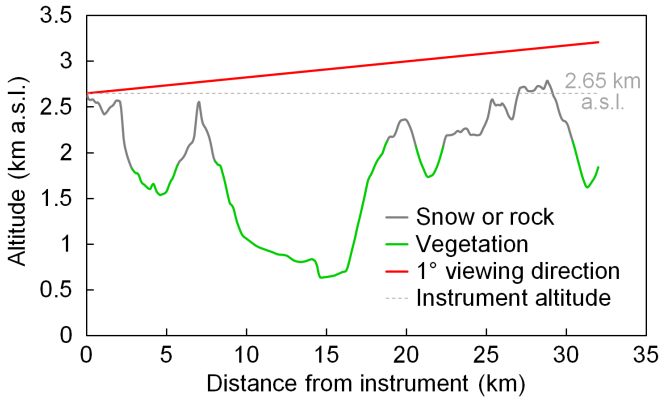

Figure 2. Altitude and type of the ground surface under the viewing direction (due south) of the MAX-DOAS at the UFS. Both the altitude data and surface type are obtained from Google Earth.

~~table described in Section 3.6~~in the radiative transfer simulations. In order to ~~compensate~~ estimate the error caused by this simplification, we investigated ~~the error~~ using the three-dimensional RTM TRACY-2.

TRACY-2 is a full spherical Monte-Carlo atmospheric RTM (Deutschmann, 2008; Wagner et al., 2007), which allows to simulate ~~3-dimensional~~ three-dimensional radiative transport as well as ~~2-dimensional~~ two-dimensional variation of the surface height. The model was compared to other RTMs and very good agreement was found (Wagner et al., 2007). ~~For the~~ We also did an inter-comparison with LIDORT. The result shows that with the same definition of topography and atmosphere, the difference between the O_4 DSCDs simulated by the two RTMs is less than 3%.

For the three-dimensional simulations carried out in this study, a pseudo-reality topography was defined with the exact ground altitude (obtained from Google Earth) in the azimuth direction of the MAX-DOAS measurements taken into account, whereas in the dimension orthogonal to this direction, the surface altitude was set constant. This simplification was chosen to reduce the computational effort. We feel that this approach is justified since the atmospheric light paths in the viewing direction of the instruments can be very large (up to several tens of kilometers), it is most important to take this variation of the surface altitude along this direction into account, whereas the influence of the orography ~~perendicular~~ perpendicular to this direction is expected to be small.

Simulations were performed with all the combinations of three different SZAs (30°, 50° and 70°), three different relative solar azimuth angles (RAAs) (30°, 60° and 90°) and two different aerosol extinction profiles (an aerosol-free profile and a box-shape profile with AOD = 0.12 and box height = 3 km), i.e. altogether 18 cases. For each case, O_4 DSCDs at 360 and 477 nm were simulated with both the flat surface at 2,650 m and the pseudo-reality topography using TRACY-2. The relative errors of O_4 DSCDs simulated with the flat surface compared to those simulated with the pseudo-reality topography are calculated. A fixed surface albedo of 0.07 was used in the simulations. For both wavelengths, the single scattering albedo was set to 0.93 and the phase function was defined as a Henyey-Greenstein phase function with the asymmetry parameter set to 0.68. The

atmospheric profile was defined as the US standard mid-latitude atmosphere (Anderson et al., 1986). Fig. 3 shows the results of some of the cases: (a) and (b) ~~shows~~ show the results of six cases with SZA = 50° and different RAAs and ~~the~~ both aerosol extinction profiles; (c) and (d) ~~shows~~ show the results of six cases with RAA = 60° and different SZAs and ~~the~~ also both aerosol extinction profiles.

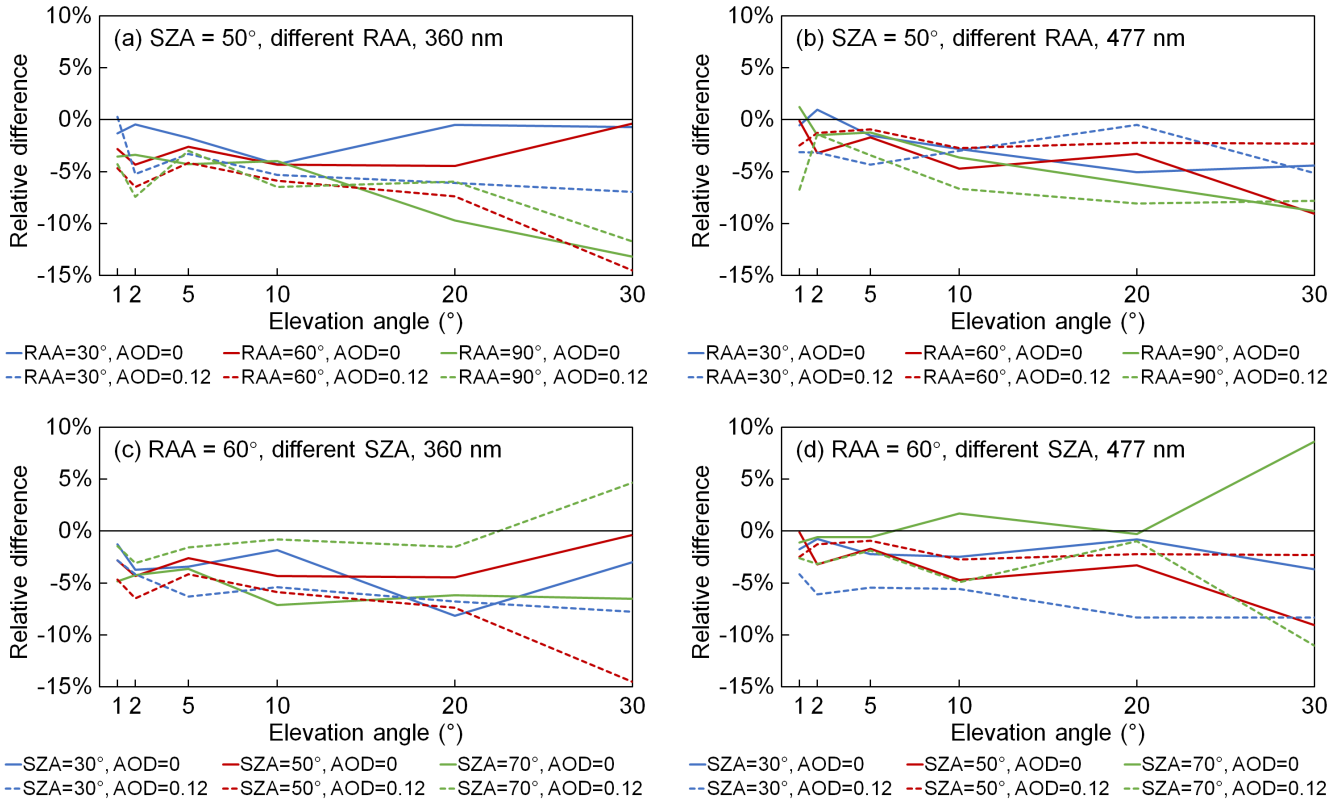

Figure 3. Relative differences of O_4 DSCDs at (a, c) 360 nm and (b, d) 477 nm simulated with a flat surface at 2,650 m comparing to the O_4 DSCDs simulated with the pseudo-reality topography. (a) and (b) show the results simulated with the same SZA of 50° and different RAAs (relative solar azimuth angles) of 30°, 60° and 90°; (c) and (d) show the results simulated with the same RAA of 60° and different SZAs of 30°, 50° and 70°. Solid curves are the results simulated under aerosol-free condition, and dashed curves are the results simulated with a box-shape profile with AOD = 0.12 and box height = 3 km.

As shown in all the panels of Fig. 3 as well as in all the other cases ~~which are~~ not shown, O_4 DSCDs simulated with the flat surface are in general slightly underestimated compared to the pseudo-reality topography. The difference could be explained by the scattering in the valleys where the concentration of O_4 is higher. For the flat surface at 2,650 m, the light paths below 2,650 m would not be taken into account, and hence the O_4 DSCDs would be underestimated. Moreover, the relative error has no obvious correlation with elevation angle, SZA, RAA and aerosol load. This is because the light path below 2,650 m is influenced by the topography, and the influence differs with the observation geometry. In addition, the light path is also

Table 3. Systematic and random errors caused by the topography simplification. Results are calculated from the relative differences of O_4 DSCDs simulated with a flat surface at 2,650 m comparing to those simulated with the pseudo-reality surface in 18 cases (see text). The mean of the relative difference for each elevation angle and each wavelength is considered as the systematic error. The standard deviation of the relative difference is considered as the random error.

Elevation angle	UV (360 nm)		VIS (477 nm)	
	Systematic error (%)	Random error (%)	Systematic error (%)	Random error (%)
1°	-3.19	1.99	-2.30	2.24
2°	-3.69	1.64	-1.90	2.21
5°	-3.42	1.60	-2.48	1.57
10°	-4.12	2.32	-3.51	2.24
20°	-4.74	3.09	-3.93	4.63
30°	-5.08	5.44	-3.91	5.84

influenced by the aerosols both below and above 2,650 m. Concerning the fact that only a pseudo-reality surface and a constant surface albedo is used in the study, the actual error caused by the topography simplification is expected to be much more complicated.

In order to make the compensation feasible, we consider the error as the combination of a systematic error and a random error. Based on the results of all the 18 cases of this study, the mean bias for each elevation angle and each wavelength is considered as the systematic error, while the standard deviation of the relative difference is considered as the random error, see Table 3. In the aerosol profile retrieval, systematic errors are first corrected from the measured O_4 DSCDs, while random errors are included in the error budget in the calculation of cost ~~function~~ functions (see Section ~~3.7~~3.7.2). In the following text, measured O_4 DSCDs refer to the values corrected by the systematic error unless otherwise mentioned.

3.4 Sensitivity analysis

In ~~this study, the look-up table method is applied for the aerosol profile inversion. The look-up table consists of a number of possible aerosol extinction profiles and the corresponding simulated~~ order to make full use of the measurement sensitivity and reduce unnecessary computational efforts, our retrieval algorithm was designed according to the sensitivity of O_4 ~~DSCDs for each elevation angle. In order to better formulate the look-up table,~~ absorption. We performed several sensitivity analyses ~~were performed~~ to determine the optimal vertical grid, step size of the aerosol extinction for each layer and the maximum aerosol extinction. In addition, these sensitivity analyses also help to ~~understand~~ estimate the measurement and model errors which are very important for the ~~aerosol profile inversion~~retrieval. The sensitivity analyses are based on ~~the~~ forward simulations of O_4 DSCDs using ~~the radiative transfer model (RTM) LIDORT(Spurr et al., 2001; Spurr, 2008)~~LIDORT. We tested the ~~sensitivity~~ sensitivities of O_4 absorption to surface albedo, aerosol optical properties ~~, and the vertical distribution of aerosols~~and aerosol vertical profile. The results of the sensitivity analyses are shown in Appendix B. The extreme and median values of the parameters are also discussed in that section.

3.5 Design of the look-up table

The basic idea of the look-up table method is to replace the repetitive time-consuming computation by a pre-calculated array. In this study, we replace the forward simulation of O_4 DSCDs by a look-up table, so that all the possible aerosol extinction profiles can be considered in the retrieval of each measurement cycle with an affordable computational effort.

We consider five input parameters for the forward simulation, which can be described as a function,

$$\Delta S_{\mathrm{s}} = f(\boldsymbol{x}, \lambda, \alpha, \theta, \phi),$$

where $\boldsymbol{x}$ is the aerosol extinction profile, λ represents the wavelength, α indicates the elevation angle, θ is the SZA, and ϕ represents the the RAA.

In order to create the look-up table, the input parameters need to be parametrized as a grid with finite nodes. We defined the grid based on the sensitivity and accuracy of the measurement. The aerosol extinction profile ($\boldsymbol{x}$) is parametrized as a profile set which consists of 7,553 possible profiles, see Section 3.5. As the simulated O_4 DSCDs are used to fit to the measured ones, only the data at 360 and 477 nm and at the six non-zenith elevation angles of our scanning cycle are included in the look-up table. SZA (θ) and RAA (ϕ) are parameterized as a grid with $1^\circ \times 1^\circ$ resolution. The look-up table includes 5,005 combinations of SZA and RAA, which can cover all the possible solar positions at the UFS. When we obtain data from the look-up table, as the input SZA and RAA are not integers, the output ΔS_{s} is interpolated from the data of the four adjacent nodes of the SZA-RAA grid. In total, the five input parameters are parametrized as a grid with $7,553 \times 2 \times 6 \times 5,005 = 453,633,180$ nodes.

As discussed in Appendix B, O_4 DSCDs are also affected by other parameters such as the ground albedo, aerosol optical properties and etc. , since their influences are relatively small and accurate data are not available, they are considered as uncertainties. In creating the look-up table, these parameters were fixed to the median values.

Details of the parameterization of the look-up table are summarized in Table 5. O_4 DSCDs corresponding to all the nodes of the look-up table were simulated using LIDORT.

Parameters for calculating the O_4 DSCD look-up table. Number of grid points 0, 0.001, 0.002, ..., 0.009, (0.001/step)0.01, 0.0115, 0.013, ..., 0.0265, (0.0015/step)0.028, 0.03, 0.032, ..., 0.038, (0.002/step) 0.04, 0.0425, 0.045, 0.0475, (0.0025/step)0.05, 0.053, 0.056, ..., 0.077, (0.003/step)0.08, 0.085, 0.09, ..., 0.115, (0.005/step) 0.12, 0.13, 0.14, ..., 0.19, (0.01/step) 0.2, 0.215, 0.23, 0.245, (0.015/step) 0.26, 0.28, 0.3 (0.02/step) aerosol extinction coefficient of 0.5 – 1 km 14 ($\sigma_1 > 0$) above instrument (km^{-1}) 1 ($\sigma_1 = 0$) aerosol extinction coefficient of 1 – 2 km 9 ($\sigma_2 > 0$) above instrument (km^{-1}) 1 ($\sigma_2 = 0$) aerosol extinction coefficient of 2 – 4 km above instrument (km^{-1}) Wavelength (nm) λ 2 360, 477 Elevation viewing angle (°) α 6 1, 2, 5, 10, 20, 30 Solar zenith angle (SZA) (°) θ 63 24, 25, 26, ..., 86 (1/step)Relative solar azimuth angle (RAA) (°) Ground albedo 1 0.1 Single scattering albedo (SSA) 1 0.93 (360 nm) / 0.92 (477 nm) Phase function 1 Median phase function[(a)] at Hohenpeißenberg obtained from AERONET

3.4.1 ~~Parameterization of the aerosol extinction profile~~

3.5 Parameterization of the aerosol extinction profile

As discussed in Appendix B4, O_4 absorption is insensitive to ~~the~~ aerosols above 2 km. Therefore, our retrieval only focuses on aerosols between 0 and 2 km above the MAX-DOAS instrument (i.e. 2,650 – 4,650 m a.s.l.). In order to limit the complexity of the retrieval, avoid unreasonable results and make full use of the measurement sensitivity, we parameterize the aerosol extinction profile as aerosol extinction extinctions in three layers. The thicknesses of the two lower layers are defined as 0.5 km. Due to the lower sensitivity at high altitude, the thickness of the third layer is ~~defined as~~ set to 1 km. The aerosol profile is denoted as a 3-dimensional state vector $\boldsymbol{x}$,

$$\boldsymbol{x} = \begin{pmatrix} \sigma_1 \\ \sigma_2 \\ \sigma_3 \end{pmatrix}, \tag{1}$$

where σ_1 is the aerosol extinction coefficient between 0 and 0.5 km (2,650 – 3,150 m a.s.l.), σ_2 is the aerosol extinction coefficient between 0.5 and 1 km (3,150 – 3,650 m a.s.l.), and σ_3 is the aerosol extinction coefficient between 1 and 2 km (3,650 – 4,650 m a.s.l.). The definition of $\boldsymbol{x}$ is illustrated in Fig. 4 (a). The vertical resolution of our retrieval grid is lower comparing to many other studies (e.g., Clémer et al., 2010; Chan et al., 2017; Tirpitz et al., 2020), however, the vertical gradient of aerosol extinction at such a high altitude site is expected to be small and this is also proved by the ceilometer measurements. Therefore, the coarse resolution is considered to be sufficient for the retrieval of the UFS MAX-DOAS measurements.

~~A set of possible aerosol extinction profiles~~

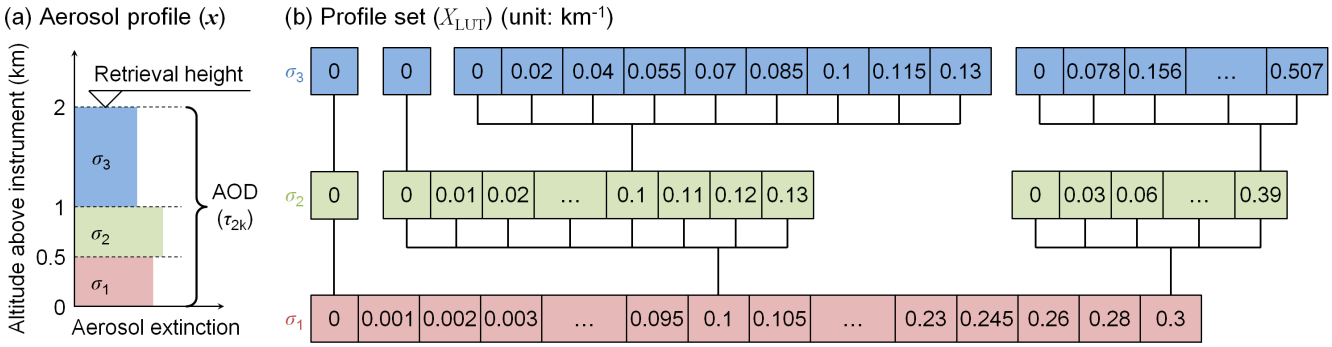

Figure 4. Definitions of (a) the parameterized aerosol profile ($\boldsymbol{x}$) and (b) the profile set (X_{LUT}). Note that only some representative nodes are shown in Panel (b).

In order to formulate the look-up table, we defined a profile set (denote as X_{LUT}) ~~is defined for the look-up table~~which is assumed to include all possible aerosol extinction profiles under cloud-free condition. X_{LUT} is a finite set of $\boldsymbol{x}$, and the

variation steps of σ_1, σ_2 and σ_3 ~~are decided~~ were determined according to the sensitivity and accuracy of measurement. X_{LUT} includes only the profiles with reasonable shapes, and the variation range of σ_1, σ_2 and σ_3 covers the actual aerosol load ~~under cloud-free condition.~~ at the UFS. In this way, unreasonable and unrealistic retrieval results can be avoided.

As discussed in Appendix B6, the measurement sensitivity decreases with increasing surface aerosol extinction, and the sensitivity is very low when the surface aerosol extinction coefficient exceeds 0.3 km^{-1}. Therefore, σ_1 is ~~set~~ defined to vary between 0 and 0.3 km^{-1}. The variation step increases from 0.001 km^{-1} per step to 0.02 km^{-1} per step with increasing aerosol extinction, so that the difference of O_4 DSCD per step is similar to the ~~typical~~ average spectral fitting error (~2%). In total, we define 65 values for σ_1, see Table ~~5~~4.

~~The~~ As illustrated in Fig. 4 (b), the values of σ_2 ~~are defined depending on~~ and σ_3 are defined as a tree, which means we define different values of σ_2 for each σ_1, and the values of σ_3 are also defined depending on σ_2. According to the ~~co-located~~ ceilometer observations at the UFS, strong elevated aerosol layers are unlikely to exist under cloud-free conditions, therefore we allow only weak elevated layers in designing the profile set. We assume that for reasonable profiles, σ_2 should not exceed σ_1 by more than 30%, and σ_3 should not exceed σ_2 by more than 30%, either. According to the sensitivity, for each value of σ_1 ($\sigma_1 > 0$), we define 14 possible values for σ_2 which varies ~~between~~ from 0 ~~and~~ to $1.3\sigma_1$ with a step size of $0.1\sigma_1$. In case $\sigma_1 = 0$, elevated layers are not considered, then σ_2 and σ_3 can only be 0.

~~Similarly, the values of~~ Similarly, σ_3 ~~are defined depending on σ_2, and σ_3~~ varies between 0 and $1.3\sigma_2$. Due to the lower measurement sensitivity at high altitude, we define 9 possible ratios between σ_3 and σ_2 (see Table ~~5~~4). In case $\sigma_2 = 0$, ~~then~~ σ_3 can only be 0.

X_{LUT} includes the profiles with all the combinations of σ_1, $\frac{\sigma_2}{\sigma_1}$ and $\frac{\sigma_3}{\sigma_2}$. For each of the 64 nonzero values of σ_1, there are $1+(13\times 9)=118$ corresponding profiles. For $\sigma_1=0$, there is only one profile with $\sigma_1=\sigma_2=\sigma_3=0$. Therefore, the profile set consists of $1+64\times 118=7,$~~which consists of $1+64\times[1+(13\times 9)]=7,553$~~ 553 aerosol extinction profiles in total.

3.6 Definitions of other dimensions of the look-up table

The basic idea of the look-up table method is to replace the repetitive time-consuming computation by a pre-calculated array. In this study, we replace the forward simulation of O_4 DSCDs by a look-up table, so that all the possible aerosol extinction profiles can be considered in the retrieval of each measurement cycle with an affordable computational effort.

Besides the parameterized aerosol extinction profile $\boldsymbol{x}$, we consider another four input parameters for the forward simulation which can be described as a function,

$$\Delta S_{\mathrm{s}} = f(\boldsymbol{x}, \lambda, \alpha, \theta, \phi), \tag{2}$$

where ΔS_{s} refers to the simulated O_4 DSCD, λ represents the wavelength, α indicates the elevation angle, θ is the SZA, and ϕ is the RAA. All the input parameters are well known in the retrieval.

In order to formulate the look-up table, the input parameters need to be parameterized as a grid with finite nodes. As already presented in Section 3.5, the aerosol extinction profile ($\boldsymbol{x}$) is parameterized as a profile set which consists of 7,553

Table 4. Definition of input parameters of the O_4 DSCD look-up table.

Parameter	Symbol	Number of grid points	Grid values
Aerosol extinction coefficient of 0 – 0.5 km above instrument (km^{-1})	σ_1	65	0, 0.001, 0.002, ..., 0.009, (0.001/step) 0.01, 0.0115, 0.013, ..., 0.0265, (0.0015/step) 0.028, 0.03, 0.032, ..., 0.038, (0.002/step) 0.04, 0.0425, 0.045, 0.0475, (0.0025/step) 0.05, 0.053, 0.056, ..., 0.077, (0.003/step) 0.08, 0.085, 0.09, ..., 0.115, (0.005/step) 0.12, 0.13, 0.14, ..., 0.19, (0.01/step) 0.2, 0.215, 0.23, 0.245, (0.015/step) 0.26, 0.28, 0.3 (0.02/step)
Aerosol extinction coefficient of 0.5 – 1 km above instrument (km^{-1})	σ_2	14 ($\sigma_1 > 0$) 1 ($\sigma_1 = 0$)	0, $0.1\sigma_1$, $0.2\sigma_1$, ..., $1.3\sigma_1$ ($0.1\sigma_1$/step)
Aerosol extinction coefficient of 1 – 2 km above instrument (km^{-1})	σ_3	9 ($\sigma_2 > 0$) 1 ($\sigma_2 = 0$)	0, $0.2\sigma_2$, $0.4\sigma_2$, $0.55\sigma_2$, $0.7\sigma_2$, $0.85\sigma_2$, σ_2, $1.15\sigma_2$, $1.3\sigma_2$
Wavelength (nm)	λ	2	360, 477
Elevation viewing angle (°)	α	6	1, 2, 5, 10, 20, 30
Solar zenith angle (SZA) (°)	θ	63	24, 25, 26, ..., 86 (1/step)
Relative solar azimuth angle (RAA) (°)	ϕ	122	0, 1, 2, ..., 121 (1/step)

possible profiles. As the simulated O_4 DSCDs are used to fit to the measured ones, only the data at 360 and 477 nm and at the six non-zenith elevation angles of the measurement cycles are included in the look-up table. SZA (θ) and RAA (ϕ) are parameterized as a grid with $1^\circ \times 1^\circ$ resolution. The grid includes 5,005 combinations of SZA and RAA, which can cover all possible solar positions for the daytime measurements at the UFS. When we obtain data from the look-up table, as the input SZA and RAA are not integers, the output ΔS_s is interpolated from the data of the four adjacent nodes of the SZA-RAA grid. In total, the five input parameters are parameterized as a grid with $7,553 \times 2 \times 6 \times 5,005 = 453,633,180$ nodes. Details of the parameterization of the input parameters are summarized in Table 4.

As discussed in Appendix ~~B4, the influence~~ B, besides the input parameters we defined, O_4 DSCDs can also be affected by other parameters such as the ground albedo, aerosol optical properties and others. Since accurate measurements of these parameters are not available and their influence is relatively small, they are considered as uncertainties. In creating the look-up table, these parameters were fixed to the median values. Details of the simulation settings are listed in Table 5. O_4 DSCDs corresponding to all the nodes of the look-up table were simulated using LIDORT.

As discussed in Appendix B5, the influence from the aerosols above 2~~km is~~ km is also considered as a kind of uncertainty ~~, and the aerosol extinction coefficient between 2~~ and ~~4 km is~~ treated in a similar way as the ~~ground albedo and aerosol optical~~

~~properties~~other unknown parameters. In the simulations for creating the look-up table, the aerosol extinction coefficient ~~in this layer is always~~ between 2 and 4 km was defined as $0.5\sigma_3$, so that this ~~'parameter ' is set~~ so-called parameter is fixed to the 'median' value. ~~It should be noted~~ Note that the aerosol extinction coefficient ~~in this layer is not~~ above 2 km is neither considered as a part of the retrieved profile nor counted in the retrieved AOD.

Table 5. Settings of fixed parameters in calculating the O_4 DSCD look-up table.

Parameter	Value or definition
Topography	Flat surface at an altitude of 2,650 m a.s.l.
Surface albedo	0.1
Single scattering albedo (SSA)	0.93 (360 nm) / 0.92 (477 nm)
Phase function	The 'median' phase function defined in Appendix B3
Climatology	US standard profiles for profile, temperature and trace gas profiles
Aerosol extinction coefficient of 2 – 4 km above instrument	50% of the aerosol extinction coefficient of 1 – 2 km above instrument (i.e. $0.5\sigma_3$)
Aerosol extinction coefficient above 4 km from instrument	0

3.7 Error estimation

Most of the other MAX-DOAS studies only consider the spectral fitting error in their retrieval. However, this fitting error only contributes to a small part of the total error. In addition, the total error is not directly proportional to the spectral fitting error. As the measurement and simulation uncertainties play an important part in our inversion method, we perform a comprehensive error analysis for the MAX-DOAS measurement and radiative transfer simulation of O_4 DSCDs. In this study, error from seven major sources are taken into account in estimating the total uncertainty.

3.7.1 ~~DOAS fitting error~~Error in measured O_4 DSCDs

~~The~~ Two error sources related to measured O_4 DSCDs are taken into account in the total uncertainty estimation, which are the DOAS fitting error ~~is denoted as~~ (ϵ_{fit}~~. In this study,~~) and the error caused by temperature variation (ϵ_{temp}).

ϵ_{fit} is ~~obtained from the fitting error reported by QDOAS which is based on the analysis of the spectral~~ the byproduct of the DSCD calculation, derived from the fit residual and the absorption cross section of O_4. It is proportional to the RMS of the fit residual. For ~~the~~ low elevation angles (1°, 2°, 5°), the percentage of ϵ_{fit} comparing to the DSCD typically varies between 1% and 3% at the UV band and between 0.3% and 0.7% at the VIS band, which is rather small compared to other sources of error. However, for the elevation angle of 30°, as the absolute DSCD value is much smaller, the percentage of ϵ_{fit} can be up to ~~10~~25% and ~~25~~10% at the UV and VIS bands, respectively.

3.7.2 ~~Error caused by temperature~~

~~The error caused by temperature is denoted as ϵ_{temp}.~~ As discussed in Section 3.1, O_4 absorption cross section measured at 273 K ~~is~~ was used in the DOAS fitting. However, the effective temperature of the MAX-DOAS measurements could be significantly different from 273 K. Previous studies show that O_4 absorption has a strong and systematic dependence on temperature ~~(Thalman and Volkamer, 2013; Wagner et al., 2018).~~

(Thalman and Volkamer, 2013; Wagner et al., 2019). In order to estimate ϵ_{temp}, we compared the O_4 DSCDs retrieved using ~~absorption~~ the cross sections measured at 253 K and 293 K to those retrieved with ~~cross section~~ the cross sections measured at 273 K. The comparison shows that the O_4 DSCDs are underestimated by 5.1% at the UV band and 2.5% at the VIS band when the effective temperature is 293 K. On the other hand, the O_4 DSCDs are overestimated by 6.9% at the UV band and 3.9% at the VIS band when the effective temperature is 253 K. These systematic errors are almost constant, regardless of the observation geometry. Between 253 and 293 K, the average variation rate of O_4 DSCD at UV band is 0.3% / K. This result is in general agreement with ~~Wagner et al. (2018)~~Wagner et al. (2019). They found that with the fitting window of 352 – 387 nm, O_4 DSCDs retrieved using the cross section at 203 K are reported to be 30% smaller than those retrieved using the cross section at 293 K, i.e. 0.33% / K in average.

Based on the fact that the temperature at the measurement site varies between ~258 and 288 K during daytime in most cases, we estimate the ϵ_{temp} of all measurements as 4.5% and 2.4% of the O_4 DSCD at UV and VIS band, respectively.

3.7.2 ~~Random error caused by the definition of the topography~~Error in simulated O_4 DSCDs

~~The~~ Five error sources related to simulated O_4 DSCDs are taken into account in estimating the total uncertainty. They are the random error caused by the simplification of the topography definition ~~is denoted as~~ (ϵ_{topo}~~.~~), the error caused by surface albedo (ϵ_{SA}), the error caused by single scattering albedo (ϵ_{SSA}), the error caused by phase function (ϵ_{PF}) and the error caused by aerosols above retrieval height ($\epsilon_{2\text{-}4\,km}$).

As discussed in Section 3.3, the ~~standard deviation of the relative errors at~~ random error caused by the simplification of the topography definition (ϵ_{topo}) of each elevation angle and each wavelength ~~from the~~ is derived from the standard deviation of the relative errors of the 18 cases ~~are treated as ϵ_{topo}.~~ simulated using the three-dimensional RTM TRACY-2. Values of ϵ_{topo} ~~for each elevation angle and each band is shown~~ are listed in Table 3.

3.7.3 ~~Error caused by surface albedo~~

~~The error caused by surface albedo is denoted as~~ For the uncertainties from the other four sources (ϵ_{SA}~~. As discussed in B1, ϵ_{SA} is different~~, ϵ_{SSA}, ϵ_{PF} and $\epsilon_{2\text{-}4\,km}$), as discussed in Appendix B, they can be estimated by radiative transfer simulations. Since they differ under different observation geometries and different aerosol loads~~. Therefore, we use a~~, we determine them using simple look-up ~~table to determine ϵ_{SA}.~~

~~According to further sensitivity tests, ϵ_{SA} is insensitive to vertical distribution of aerosols.~~ tables in the retrieval. In order to simplify the error estimation process, we assume that ~~it is~~ the uncertainties from the four sources are only influenced by the

AOD, while the influence from different vertical distribution of aerosols is neglected. In addition, from the O_4 DSCD look-up table, we found that O_4 DSCD at 5° is almost negatively correlated with AOD, while it is insensitive to the shape of profile. Therefore, we use the O_4 DSCD measured at 5° as the indicator for estimating the AOD in deriving uncertainty values from the error look-up tables.

The ~~ϵ_{SA}~~ error look-up ~~table consists of the~~ tables consist of the values of ϵ_{SA}, ϵ_{SSA}, ϵ_{PF} and $\epsilon_{2\text{-}4\,km}$ for all the combinations of SZA and RAA (with $1° \times 1°$ resolution) and 65 profiles of the X_{LUT} with $\sigma_1 = \sigma_2 = \sigma_3$. ~~Same as the O_4 DSCD~~ The calculation of the error look-up ~~table, the aerosol extinction coefficient between 2 and 4 km is set as $0.5\sigma_3$.~~ tables was similar as the sensitivity study. In order to estimate the uncertainty caused by each parameter, O_4 DSCDs were simulated ~~with both the~~ under both median and extreme values~~of surface albedo (0.1 and 0.2, respectively)~~, while all the other parameters were fixed as the median settings listed in Table 5. The relative difference between the two simulations is ~~considered as the error.~~

~~In order to determine ϵ_{SA} of each measurement, the AOD is first estimated using the O_4 DSCD measured at 5° of the corresponding scan. Subsequently, ϵ_{SA} is derived from the~~ treated as the uncertainty and stored in the look-up table~~according to the first approximation of AOD~~.

~~It should be noted that there is probably also a systematic effect of the surface albedo on the measurements at the high altitude station: due to the dependence of the snow coverage on altitude, the surface albedo close to the instrument is typically higher than at locations far away. Since the measurements at high elevation angles are usually more sensitive to air masses closer to the instrument, they are probably stronger affected by snow and ice than measurements at low elevation angles. In this study, this effect cannot be further quantified, but it might be one reason for the need of different O_4 DSCD scaling factors for different elevation angles, see Section 3.9.~~

3.7.3 ~~Error caused by single scattering albedo~~

~~The error caused by SSA is denoted as ϵ_{SSA}. Similar to~~ As discussed in Appendix B1, the uncertainty caused by surface albedo (ϵ_{SA}~~, ϵ_{SSA} is determined using a simple look-up table. The error values were also calculated~~) was derived from the relative ~~differences between~~ difference of the O_4 DSCDs simulated ~~under extreme and median values of SSA.~~ with the surface albedo set to 0.2 (extreme value) and 0.1 (median value).

As discussed in Appendix B2~~and shown in~~, in the estimation of the uncertainty caused by single scattering albedo (ϵ_{SSA}), the extreme value ~~is~~ was chosen as 0.997 for both the UV and VIS bands, while the median value ~~is~~ was chosen as 0.92 ~~for the UV band~~ and 0.93 for ~~the VIS band~~UV and VIS bands, respectively.

3.7.3 ~~Error caused by phase function~~

~~The error caused by phase function is denoted as ϵ_{PF}. ϵ_{PF} is also determined using a simple look-up table.~~ As discussed in Appendix B3, from all the phase functions measured by the AERONET station in Hohenpeißenberg during the period of 2013 – 2014, the phase function with which the simulated O_4 DSCDs at all elevation angles are closest to the median values ~~is~~ was chosen as the so-called 'median' phase function. The phase function with which the simulated O_4 DSCDs are closest to the rank of 95% (i.e. 2σ) ~~is~~ was chosen as the 'extreme' phase function. ~~The difference of~~ ϵ_{PF} was derived from the relative

difference between O_4 DSCDs ~~between the simulations~~ simulated with 'median' and 'extreme' phase ~~function is treated as ϵ_{PF}~~functions.

3.7.3 ~~Error caused by aerosols above retrieval height~~

~~The~~ As discussed in Appendix B5, the error caused by aerosols above ~~retrieval height (~~2 km ~~above instrument) is denoted as $\epsilon_{2\text{-}4\,km}$. As discussed in B5, $\epsilon_{2\text{-}4\,km}$ is~~ ($\epsilon_{2\text{-}4\,km}$) is treated similarly as ϵ_{SA}, ϵ_{SSA} and ϵ_{PF} ~~, and it is also determined using a simple look-up table. The error values are calculated from the relative differences between~~ in the study. The so-called 'median' O_4 DSCDs were simulated with profiles with the aerosol extinction coefficient between 2 and 4 km equals to ~~σ_3 and those simulated with profiles with~~ $0.5\sigma_3$ (50% of the aerosol extinction coefficient between 1 and 2 km), while the 'extreme' values were simulated with the aerosol extinction coefficient between 2 and 4 km ~~equals to $0.5\sigma_3$.~~ set equal to σ_3. $\epsilon_{2\text{-}4\,km}$ was derived from the relative difference between the 'extreme' and 'median' results.

3.7.3 Total uncertainty

We assume that ~~all~~ the seven kinds of ~~error~~ errors mentioned in Sections 3.7.1 and 3.7.2 follow the normal distribution, and the total uncertainty of each band and each elevation angle can be determined by the root mean square of the seven errors as

$$\epsilon = \sqrt{\epsilon_{\text{fit}}^2 + \epsilon_{\text{temp}}^2 + \epsilon_{\text{topo}}^2 + \epsilon_{\text{SA}}^2 + \epsilon_{\text{SSA}}^2 + \epsilon_{\text{PF}}^2 + \epsilon_{\text{2-4\,km}}^2}. \quad (3)$$

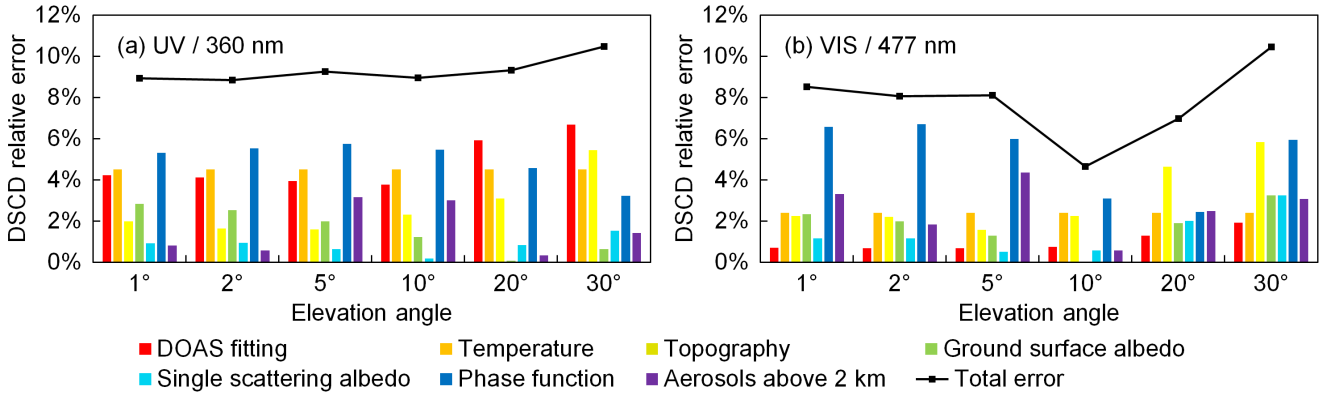

Figure 5. Error budget of (a) UV and (b) VIS bands of the scanning cycle on 05 Jul 2015 at ~16:26 UTC (SZA ~64°, RAA ~97°). Y-axes refer to the relative error of O_4 DSCDs.

~~shows an example~~ Examples of the error ~~budget of a scanning cycle~~ budgets of two measurement cycles for both wavelength bands are shown in Fig. 5 and Fig. 6. The cycle shown in Fig. 5 was measured in summer under relatively high aerosol load (AOD at 440 nm measured by the sun photometer around the noon of that day was ~0.2), while the cycle shown in Fig. 6

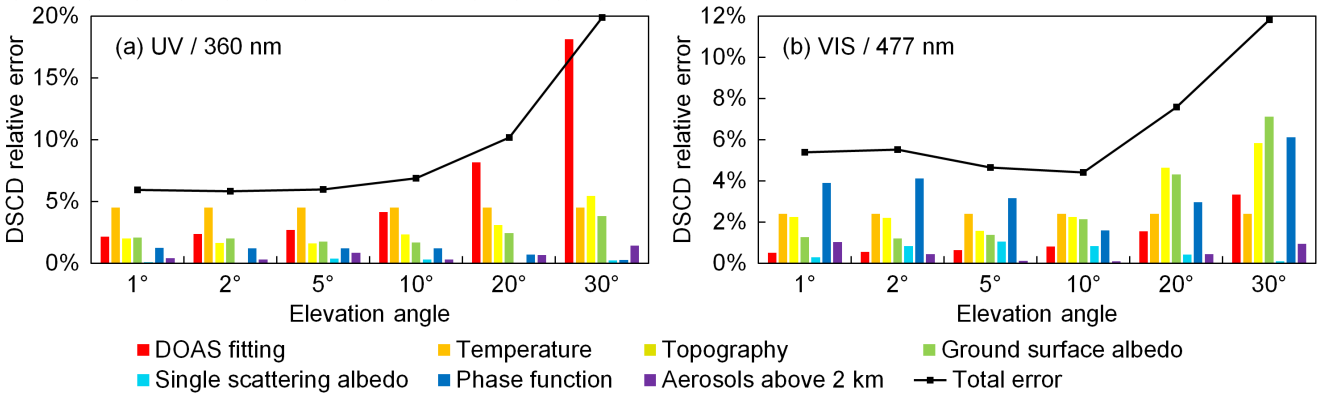

Figure 6. Same as Fig. 5, but for the scanning cycle on 07 Dec 2015 at ~13:55 UTC (SZA ~79°, RAA ~39°).

was measured in winter under relatively low aerosol load (AOD at 440 nm measured by the sun photometer around the noon of that day was ~0.015). In addition, The former cycle was measured under a smaller SZA comparing to the latter one (64° and 79°, respectively), while the RAA was much larger than the latter (97° and 39°, respectively). The results show that contributions from different error sources are quite different in different measurement cycles, at different wavelengths and at different elevation angles. ~~The result shows that the major source of error is different at different elevation angles and different wavelengths.~~

3.7.4 Other possible error sources

Besides the seven above-mentioned error sources, there are still some other sources of error which are difficult to be estimated and hence not included in the error estimation. For example:

a. Error in O_4 DSCD scaling factors: in this study, we found that an elevation dependent O_4 DSCD scaling factor is needed to bring measurements and ~~model~~ modeled results into agreement. We determined the factors based on the statistical analysis of the long-term ~~measurement~~measurements, see Section 3.9. However, as it is still difficult to estimate the uncertainties of the scaling factors, they are currently not taken into account in calculating the total uncertainty.

b. Error caused by horizontal gradients of the aerosol extinction: besides its direct effect on the measurements, the complex topography might also cause systematic horizontal gradients of the aerosol extinction. For example polluted air masses from the valleys might be transported to higher altitudes according to the vertical mixing and the prevailing wind direction. Such effects can be especially important for the measurements discussed here because of the rather low AOD. Further quantification of the effects of possible horizontal gradients is beyond the scope of this study, but might be one reason for the observed elevation dependence of the O_4 DSCD scaling factor.

c. Error caused by the variation of atmospheric profile: the O_4 DSCD look-up table was calculated using the US standard climatology data, but the change of atmospheric temperature and pressure can slightly affect the O_4 absorption. However,

since it is difficult to estimate the accurate uncertainty and real-time measurements of temperature and pressure profiles are not available, the error caused by the variation of the atmospheric profile is not taken into account in calculating the total uncertainty.

d. Systematic effect of the surface albedo on the measurements at the high altitude station: due to the dependence of the snow coverage on altitude, the surface albedo close to the instrument is typically higher than at locations far away. Since the measurements at high elevation angles are usually more sensitive to air masses closer to the instrument, they are probably stronger affected by snow and ice than measurements at low elevation angles. In this study, this effect cannot be further quantified, but it might be one reason for the need of different O_4 DSCD scaling factors for different elevation angles, see Section 3.9.

In order to avoid the underestimation of the measurement uncertainty, we set a relative relaxed threshold of cost functions for choosing valid profiles, see Section 3.8.

3.8 Inversion method

Aerosol extinction profiles are retrieved from the measured O_4 DSCDs of each scanning cycle. The measurements of the UV and VIS ~~band measurements~~ bands are retrieved separately. The measured O_4 DSCDs ~~of~~ at the UV and VIS bands are fitted to the simulated O_4 DSCDs at 360 and 477 nm, respectively. In the retrieval, we assume the state of atmosphere ~~is~~ being stable during a scanning cycle, and the distribution of aerosols ~~is~~ homogeneous in horizontal direction. For a single scanning cycle~~and a single O_4 wavelength band λ~~, the measured O_4 DSCDs at the wavelength λ are denoted as a measurement vector

$$\boldsymbol{y}_{\mathrm{m}} = \begin{pmatrix} \Delta S_{\lambda,1} \\ \Delta S_{\lambda,2} \\ \vdots \\ \Delta S_{\lambda,M} \end{pmatrix}, \tag{4}$$

where M is the number of off-zenith measurements in each scanning cycle, which is 6 in this study. $\Delta S_{\lambda,1}$, $\Delta S_{\lambda,2}$, ..., $\Delta S_{\lambda,6}$ are the O_4 DSCDs measured at O_4 wavelength band λ with the viewing elevation angles of 1°, 2°, 5°, 10°, 20° and 30°, respectively.

The simulated O_4 DSCDs corresponding to each possible aerosol extinction profile in X_{LUT} can be obtained from the look-up table. Similar to $\boldsymbol{y}_{\mathrm{m}}$, the simulation vector $\boldsymbol{y}_{\mathrm{s}}$ for each possible profile $\boldsymbol{x}$ is be denoted as

$$\boldsymbol{y}_{\mathrm{s}}(\boldsymbol{x}) = \begin{pmatrix} f(\boldsymbol{x},\lambda,\alpha_1,\theta_1,\phi_1) \\ f(\boldsymbol{x},\lambda,\alpha_2,\theta_2,\phi_2) \\ \vdots \\ f(\boldsymbol{x},\lambda,\alpha_M,\theta_M,\phi_M) \end{pmatrix}, \boldsymbol{x} \in X_{\mathrm{LUT}}. \tag{5}$$

Aerosol extinction profiles can be derived by fitting the forward simulation to the measured O_4 DSCDs. Typically, the optimal solution can be ~~detemined~~ determined by minimizing the cost function, which is defined as

$$\chi^2(\boldsymbol{x}) = [\boldsymbol{y}_{\mathrm{m}} - \boldsymbol{y}_{\mathrm{s}}(\boldsymbol{x})]^{\mathrm{T}} \cdot \mathbf{S}_{\epsilon}^{-1} \cdot [\boldsymbol{y}_{\mathrm{m}} - \boldsymbol{y}_{\mathrm{s}}(\boldsymbol{x})], \tag{6}$$

where $\mathbf{S}_{\epsilon}$ is the uncertainty covariance matrix. Assuming the measurements of each viewing elevation angle are independent, $\mathbf{S}_{\epsilon}$ is a diagonal matrix and its diagonal elements equal to the square of the ~~measurement~~ total uncertainties of each elevation angle defined in Eq. (3),

$$\mathbf{S}_{\epsilon} = \begin{bmatrix} \epsilon_1^2 & 0 & \dots & 0 \\ 0 & \epsilon_2^2 & \dots & 0 \\ \vdots & \vdots & \ddots & \vdots \\ 0 & 0 & \dots & \epsilon_M^2 \end{bmatrix}. \tag{7}$$

Our cost function definition is similar to the cost functions used in many of the MAX-DOAS studies based on the OEM (e.g., Clémer et al., 2010; Frieß et al., 2016; Wang et al., 2016; Chan et al., 2017), but only includes the item related to measurement error, while the item related to the a priori profile is omitted. This is because the a priori profile is not needed in our retrieval algorithm.

χ^2 indicates the difference between $\boldsymbol{y}_{\mathrm{s}}$ and $\boldsymbol{y}_{\mathrm{m}}$, however, as the retrieval is ill-posed and the SNR of the ~~measurement~~ measurements at the UFS is low, the single profile with the lowest χ^2 is not necessarily the one closest to the true profile. In order to overcome this limitation, we consider all the profiles in X_{LUT} with $\chi^2(\boldsymbol{x}) \leq 1.5M$ (9 in this study) as valid profiles and calculate the weighted mean profile as the optimal result. A profile with $\chi^2 \leq M$ indicates that the measured and simulated O_4 DSCDs agree within the measurement errors, but in order to avoid underestimation of the measurement errors, we ~~defined~~ define the threshold as $1.5M$. The weight of each valid profile for the calculation of the optimal solution is defined as

$$w(\boldsymbol{x}) = \frac{1/\chi^2(\boldsymbol{x})}{\sum[1/\chi^2(\boldsymbol{x})]}, \boldsymbol{x} \in X_{\mathrm{LUT}}, \chi^2(\boldsymbol{x}) \leq 1.5M, \tag{8}$$

and the optimal solution can be calculated as

$$\hat{\boldsymbol{x}} = \sum w(\boldsymbol{x}) \cdot \boldsymbol{x}, \boldsymbol{x} \in X_{\mathrm{LUT}}, \chi^2(\boldsymbol{x}) \leq 1.5M. \tag{9}$$

3.9 O_4 DSCD correction

Discrepancies between measured and simulated O_4 DSCDs are found in many other MAX-DOAS studies ~~(Wagner et al., 2009; Clémer et al~~ The discrepancies are often explained by the systematic ~~error in~~ errors of the absorption cross section of O_4 ~~, and therefore~~

~~correction is~~ as well as the radiative transfer simulation, and a correction is therefore necessary. Previous studies suggested to multiply a constant scaling factor (usually between 0.75 and 0.9) to the measured O_4 DSCD for all elevations to correct for the systematic error ~~(Wagner et al., 2009; Clémer et al., 2010; Chan et al., 2015; Wang et al., 2016). A recent study comparing modeled~~ (e.g., Wagner et al., 2009; Clémer et al., 2010; Chan et al., 2015; Wang et al., 2016). Some recent studies suggested elevation-dependent scaling factors. Irie et al. (2015) suggested a set of scaling factors for 477 nm which gradually decreases with increasing elevation angle, varying from 0.984 for 1° to 0.667 for 30°. Zhang et al. (2018) suggested a set of scaling factors for 360 nm which also decreases with increasing elevation angle, varying from from 1.02 for 1° to 0.909 for 30°. Chan et al. (2017) derived a set of elevation-dependent scaling factors for 477 nm by comparing modelled and measured (relative) intensity~~shows that the~~, varying from 0.792 for 1° to 0.957 for 30°. On the other hand, some other MAX-DOAS studies did not find it necessary to apply any correction to O_4 ~~scaling factor might be dependent on the measurement elevation (Chan et al., 2017). In all these studies,~~ DSCDs. For example, Frieß et al. (2011) reported that for the MAX-DOAS measurements in an Arctic area, the measured and simulated O_4 DSCDs ~~were reported to be underestimated comparing to the measured ones~~are in good agreement without any correction. Note that the scaling factor mentioned here refers to the ratio between simulated and measured O_4 DSCDs, which is opposite to some other studies.

In order to assess whether the O_4 DSCD correction is necessary for the MAX-DOAS ~~measurement~~ measurements at the UFS, we compared the measured O_4 DSCDs to the simulated ones in the look-up table. Assuming our profile set (X_{LUT}) covers all ~~the~~ possible aerosol profiles under cloud-free condition, we derived the O_4 scaling factor for each elevation angle and each ~~band~~ wavelength based on the statistical analysis. The AODs measured by the sun photometer were used to restrict the range of possible profiles.

Fig. 7 shows the scattered plots of measured and simulated O_4 DSCDs of the scanning cycle on 07 Dec 2015 at ~13:55 UTC. Both the measurements of (a) UV and (b) VIS bands are shown. According to the cloud screening as well as the skycam images, this day was absolutely cloud free. Total AOD measured by the sun photometer at that time is 0.02 and 0.017 for 360 and 477 nm bands, respectively. ~~The x-axes of the plots indicate~~ In each plot, the x-axis indicates the O_4 DSCDs measured (or simulated) at the elevation angle of 1°, while the ~~y-axes represent~~ y-axis represents the O_4 DSCDs ~~measured (or simulated) at~~ at the other elevation angles. Different colours indicate measurements at different elevation angles. The simulated O_4 DSCDs ($\boldsymbol{y}_{\mathrm{s}}(\boldsymbol{x})$) of all the possible profiles in X_{LUT} are shown as coloured dots. We assume the MAX-DOAS measurement of AOD between 0 and 2 km (denoted as $\tau_{2\mathrm{k}}$, $\tau_{2\mathrm{k}}(\boldsymbol{x}) = 0.5\sigma_1(\boldsymbol{x}) + 0.5\sigma_2(\boldsymbol{x}) + \sigma_3(\boldsymbol{x})$) varies between 50% and 100% of the total AOD measured by the sun photometer (denoted as $\tau_{\mathrm{sp},\lambda}$) in most cases, and the data points of the profiles fulfilling this assumption are highlighted. The measured O_4 DSCDs (already corrected for the systematic errors caused by the topography simplification) are plotted as square markers with error bars showing the total uncertainties. It is obvious that at most of the elevation angles, the measured O_4 DSCD does not agree with the simulations within the total error. As a result, at both UV and VIS bands, no profiles in X_{LUT} satisfy the selection requirement ($\chi^2 \leq 9$, see dashed curves in Fig. 8). No profiles matching the measurement is unlikely to happen under such clear sky condition, hence, implies a systematic error and correction of the error is necessary.

In order to determine whether the O_4 scaling factor is constant for all elevations or ~~it is~~ dependent on the viewing elevation angles, we ~~plotted the variation range of the~~ first assume it is constant and plot the corrected O_4 DSCD measurements in

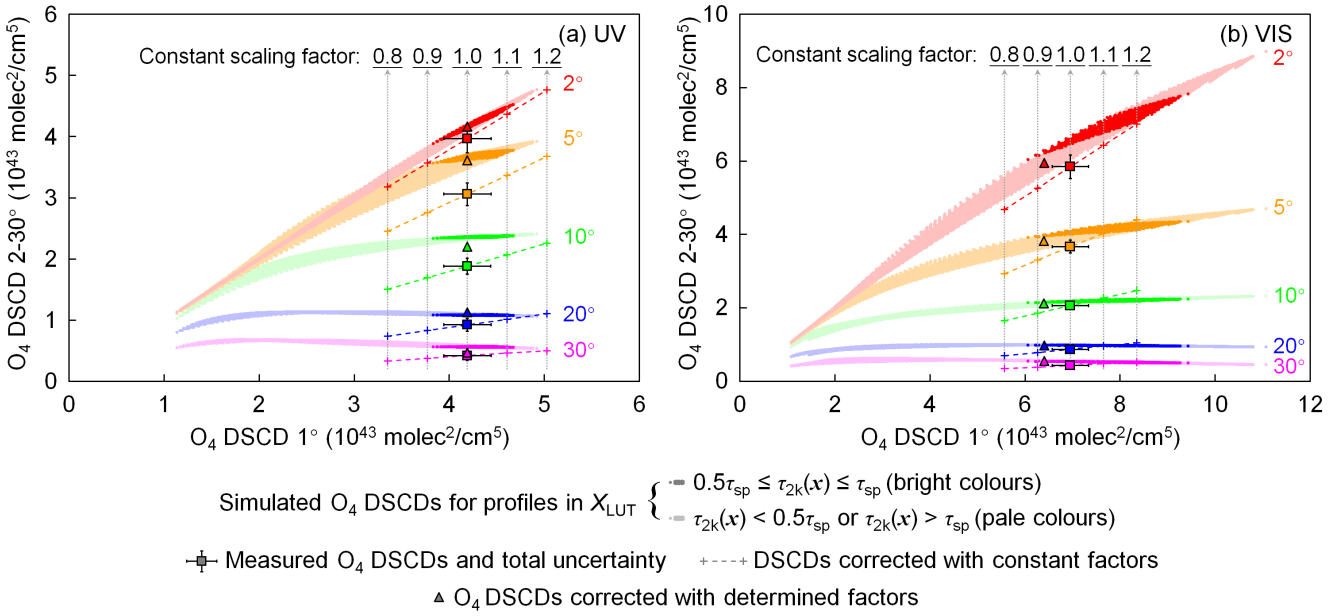

Figure 7. Distribution of simulated, measured and corrected O_4 DSCDs in (a) UV and (b) VIS bands of the scanning cycle on 07 Dec 2015 at ~13:55 UTC (SZA ~79°, RAA ~39°). X-axes indicate the O_4 DSCDs measured (or simulated) at the elevation angle of 1°, while y-axes represent the O_4 DSCDs measured (or simulated) at other elevation angles. Different colours indicate measurements at different elevation angles. The coloured dots show the simulated O_4 DSCDs of all the possible profiles in the profile set (X_{LUT}). The data points of the profiles with AOD between 0 and 2 km ($\tau_{2\mathrm{k}}(\boldsymbol{x})$) varies between 50% and 100% of the total AOD measured by the sun photometer ($\tau_{\mathrm{sp},\lambda}$) are shown in bright colours, while the dots of the other profiles are shown in pale colours. The square markers represent measured O_4 DSCDs, and the error bars show the total uncertainties. Systematic errors caused by the topography simplification are already corrected from the measured O_4 DSCDs. The plus signs along the dashed lines show the measured O_4 DSCDs corrected with constant factors of 0.8, 0.9, 1.1 and 1.2. The triangle markers show the measured O_4 DSCDs corrected with the finally determined scaling factors listed in Table 6.

Fig. 7~~assuming constant scaling factor for all elevation angles. The~~ . The plus signs indicate the measured O_4 DSCDs corrected with constant scaling factors of 0.8, 0.9, 1.1 and 1.2. Furthermore, the corrected O_4 DSCDs should vary along the coloured dashed lines if ~~a~~ any other constant scaling factor is applied to the measurements. ~~The plus signs indicate the O_4 DSCDs corrected with constant scaling factors of 0.8, 0.9, 1.1 and 1.2, respectively. The~~ However, the forward simulation of O_4 DSCDs does not overlap with the dashed lines in most of the cases (especially for 5° and 10° of the UV band), indicating that a constant O_4 scaling factor for all viewing elevation angles could not resolve the systematic error. Therefore, different scaling factors should be applied to different elevation angles.

In this study, the O_4 DSCD scaling factors for each viewing elevation angle and wavelength were determined through the statistical analysis of the long-term observations. We assume the scaling factor mainly depends on the viewing elevation

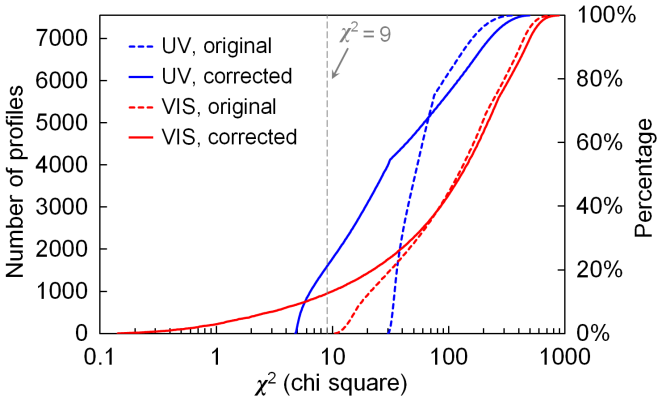

Figure 8. Cumulative distribution of the χ^2 of all the profiles in X_{LUT} for the scanning cycle at 07 Dec 2015 ∼13:55 UTC (SZA ∼79°, RAA ∼39°). Dashed and solid curves refer to the results before and after the O_4 DSCD correction, respectively. Blue and red curves refer to the results of the UV and VIS bands, respectively. Note that the x-axis is logarithmically scaled.

angle, while being less sensitive to other factors ~~, e.g., solar geometryand aerosol load~~such as solar geometry, aerosol load, temperature etc.

Fig. 7 shows that the simulated O_4 DSCDs at high elevation angles (e.g. 20° and 30°) vary in a very narrow range. Based on the assumption that X_{LUT} covers all possible aerosol profiles, the measured O_4 DSCDs should lie within the range. The scaling factor can be derived by taking the ratio of the simulated and measured values. As the simulated value varies in a narrow range, the uncertainty of the derived scaling factor should also be low. In order to have ~~a better statistic~~ better statistics of the scaling factors, this method was applied to the long-term measurements. In addition, only the measurements taken under cloud-free and low aerosol load ($\tau_{\mathrm{sp},\lambda} \leq 0.03$) conditions were used, so as to avoid accounting data contaminated by clouds in the analysis. Here it should be noted that measurements with AOD < 0.03 are almost entirely found during winter due to the strong seasonal variation of aerosol load at the UFS. Subsequently, for the wavelength λ and the i^{th} elevation angle of each scanning cycle, we calculate the variation range of the simulated O_4 DSCDs for all the profiles fulfilling $0.5\tau_{\mathrm{sp},\lambda} \leq \tau_{2\mathrm{k}}(\boldsymbol{x}) \leq \tau_{\mathrm{sp},\lambda}$, which can be described as a set,

$$Y^*_{\lambda,i} = \{f(\boldsymbol{x}, \lambda, \alpha_i, \theta_i, \phi_i) \mid \boldsymbol{x} \in X_{\mathrm{LUT}}, 0.5\tau_{\mathrm{sp},\lambda} \leq \tau_{2\mathrm{k}}(\boldsymbol{x}) \leq \tau_{\mathrm{sp},\lambda}\}. \tag{10}$$

Only if $\max(Y^*_{\lambda,i}) \leq 1.1 \times \min(Y^*_{\lambda,i})$, then the scanning cycle was taken into account. In most cases, measured O_4 DSCDs at high elevation angles are lower than simulated ones, therefore we calculate the scaling factor from the minimum value in $Y^*_{\lambda,i}$ to avoid over-estimation of the scaling factor. The scaling factor derived from this scanning cycle is denoted as

$$\gamma^*_{\lambda,i} = \frac{\min(Y^*_{\lambda,i})}{\Delta S_{\lambda,i}}, \tag{11}$$

where $\Delta S_{\lambda,i}$ is the measured O_4 DSCD (already corrected for the systematic errors caused by the topography). For the elevation angles of 5°, 10°, 20°, 30° ~~of~~ at UV band and 10°, 20°, 30° ~~of~~ at VIS band, numerous scanning cycles from the long-term ~~measurement~~ measurements fulfill the selection criterion, and hence there are sufficient samples of $\gamma^*_{\lambda,i}$ for statistical analysis. We analyzed the frequency distribution of ~~$\gamma^*_{\lambda,1i}$~~ $\gamma^*_{\lambda,i}$ of each elevation and each wavelength band. The result shows that the distributions of ~~$\gamma^*_{\lambda,1i}$~~ $\gamma^*_{\lambda,i}$ follow the normal distribution function with small standard deviation. For instance, for the elevation angle of 20°, the standard deviations of UV and VIS bands are both ~0.16. Subsequently, ~~$\gamma^*_{\lambda,1i}$~~ $\gamma^*_{\lambda,i}$ with the maximum frequency was derived by Gaussian fit. The peak value ~~is~~ was used as the scaling factor which is denoted as $\hat{\gamma}_{\lambda,i}$.

For the low elevation angles (1° and 2° ~~of~~ at UV band, 1°, 2° and 5° ~~of~~ at VIS band), as O_4 DSCD varies in a wide range, it is impossible to determine the scaling factor with the method mentioned above. However, it is found that in many scanning cycles, within the possible profiles in X_{LUT}, the simulated O_4 DSCDs at low elevation angles are well correlated to those at the neighbouring elevation angle. Therefore, once the scaling factor of the higher elevation angle is determined, we can derive an expected value of the O_4 DSCD at the lower elevation angle from the corrected O_4 DSCD at the higher ~~elevation angle~~one, and the scaling factor can be derived by ~~taikng~~ taking the ratio of the expected value and the measured value.

For the wavelength λ and for each scanning cycle, a subset of X_{LUT} is defined as

$$X^{\dagger} = \{\boldsymbol{x} \mid \boldsymbol{x} \in X_{\mathrm{LUT}}, 0 \leq \tau_{2\mathrm{k}}(\boldsymbol{x}) \leq 2\tau_{\mathrm{sp},\lambda}\}, \tag{12}$$

and the elements of $X^{\dagger}$ are denoted as $\boldsymbol{x}^{\dagger}_j$. The corresponding simulated O_4 DSCD at the i^{th} elevation angle is denoted as

$$\Delta S^{\dagger}_{i,j} = f(\boldsymbol{x}^{\dagger}_j, \lambda, \alpha_i, \theta_i, \phi_i), \boldsymbol{x}^{\dagger}_j \in X^{\dagger}. \tag{13}$$

A 3^{rd} order polynomial regression is applied between $\Delta S^{\dagger}_{i,j}$ and $\Delta S^{\dagger}_{i+1,j}$. The regression function is denoted as g. Only if the correlation coefficient $R^2 \geq 0.98$, this scanning cycle is taken into account. As the scaling factor of the $(i+1)^{\mathrm{th}}$ elevation ($\hat{\gamma}_{\lambda,i+1}$) is already determined, the expected value of the O_4 DSCD at the i^{th} elevation angle can be derived with the regression function:

$$E[\Delta S_{\lambda,i}] = g(\Delta S_{\lambda,i+1} \cdot \hat{\gamma}_{\lambda,i+1}), \tag{14}$$

and the scaling factor derived from this scanning cycle is

$$\gamma^{\dagger}_{\lambda,i} = \frac{E[\Delta S_{\lambda,i}]}{\Delta S_{\lambda,i}}. \tag{15}$$

Similar to the high elevation angles, the frequency distribution of $\gamma^{\dagger}_{\lambda,i}$ from all the available samples was analyzed by fitting to a Gaussian function. The peak value of $\gamma^{\dagger}_{\lambda,i}$ is used as $\hat{\gamma}_{\lambda,i}$. The scaling factor of the $(i-1)^{\mathrm{th}}$ elevation is then derived in the same way. The scaling factors of 1° and 2° ~~of~~ at UV band and 1°, 2°, 5° ~~of~~ at VIS band were determined using this method.

Table 6. The finally determined O_4 DSCD scaling factors.

Elevation angle	Factors for corrected O_4 DSCDs[(a)]		Factors for original O_4 DSCDs	
	UV (360 nm)	VIS (477 nm)	UV (360 nm)	VIS (477 nm)
1°	1.00	0.92	0.97	0.90
2°	1.05	1.02	1.01	1.00
5°	1.18	1.04	1.14	1.02
10°	1.17	1.03	1.12	0.99
20°	1.22	1.12	1.16	1.08
30°	1.12	1.27	1.06	1.22

[(a)] Means the O_4 DSCDs which are already corrected for the systematic errors caused by the topography simplification.

The determined scaling factors are listed in Table 6. The corrected O_4 DSCDs are indicated as triangles in Fig. 7. The result shows that except the elevation angle of 1°, the simulated O_4 DSCDs are overestimated comparing to the measured ones. It should be noted that the determination of the scaling factors is based on the measured O_4 DSCDs which are already corrected for the systematic errors caused by the topography simplification (discussed in 3.3). Comparing to the original measurements, the result still indicates that the simulated O_4 DSCDs at high elevation angles are overestimated. This result is opposite to the results of the other studies. ~~The difference might be caused by the high altitude or the complex topography~~At the moment we have no clear explanation for this finding, it might be related to the specific properties of the high altitude station, e.g. the highly structured topography, horizontal gradients of the aerosol extinction and the systematic dependence of the surface albedo on altitude.

Fig. 8 shows the cumulative distribution of χ^2 of all the profiles in X_{LUT} for the scanning cycle shown in Fig. 7. The distribution of χ^2 before and after the DSCD correction are shown as dashed and solid curves, respectively. ~~It can be seen~~ The result indicates that for both UV (blue curves) and VIS (red curves) bands, the χ^2 of most profiles in X_{LUT} are significantly lower after the correction. As a result, a number of profiles fulfill the selection criterion ($\chi^2 \leq 9$). Note that the AODs measured by MAX-DOAS are still expected to be lower than the sun photometer observations due to the fact that the MAX-DOAS only reports the AOD below 2 km while the sun photometer covers the entire atmosphere.

4 Results and discussion

Our retrieval algorithm was applied to the long-term measurement data of the UFS MAX-DOAS from February 2012 to February 2013 and from July 2013 to February 2016. The results are also compared to sun photometer ~~measurement~~measurements. This section presents the results as well as ~~the discussionbased on the results~~their discussion.

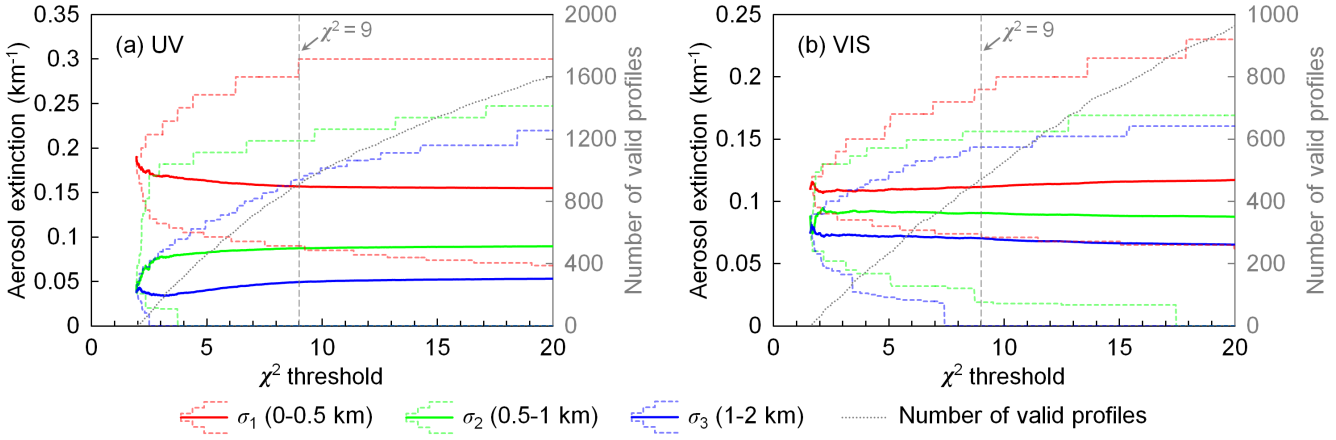

Figure 9. Weighted mean profiles, variation ranges of valid profiles and number of valid profiles of (a) UV and (b) VIS bands corresponding to different χ^2 thresholds, results of the scanning cycle on 05 Jul 2015 at ~16:26 UTC (SZA ~64°, RAA ~97°). The weighted mean profiles are shown as solid curves which indicate the aerosol extinction coefficients in the three layers (σ_1, σ_2 and σ_3). The variation ranges of valid profiles are shown as dashed curves which indicates the variation ranges of σ_1, σ_2 and σ_3. The grey dotted curves indicate the number of valid profiles corresponding to different thresholds of χ^2. Measured O_4 DSCDs are corrected with the scaling factors listed in Table 6.

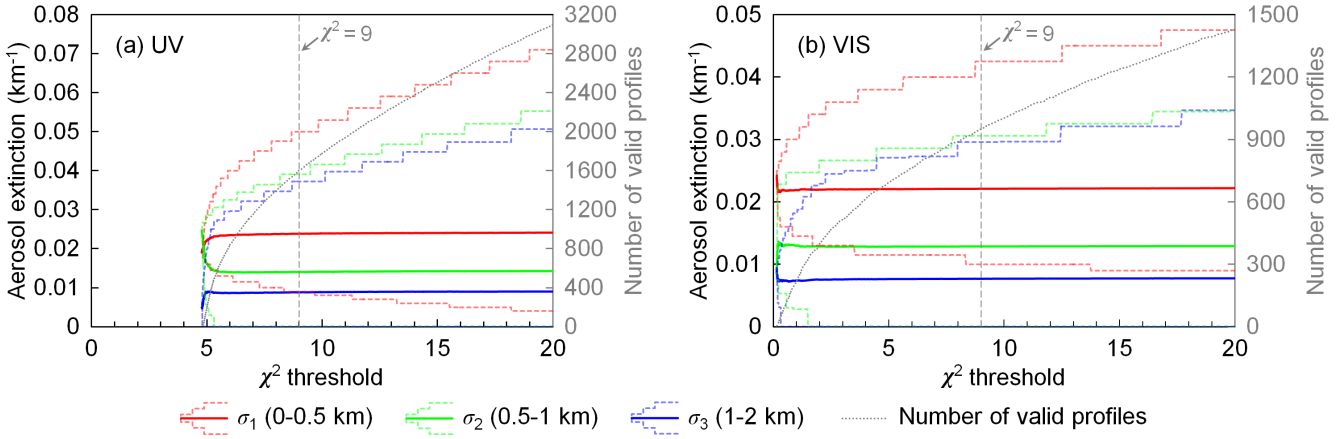

Figure 10. Same as Fig. 9, but for the scanning cycle on 07 Dec 2015 at ~13:55 UTC (SZA ~79°, RAA ~39°).

4.1 Dependency of retrieval result on the threshold of cost function

As presented in Section 3.8, we consider all the profiles with $\chi^2 \leq 9$ as valid profiles, and the retrieved profile is defined as the weighted mean of all the possible profiles. In this section, we investigate the dependency of the retrieval result on the threshold of χ^2 by comparing the results calculated with different different χ^2 thresholds. Take the ~~scanning cycle on~~ two

measurement cycles mentioned in Fig. 5 and Fig. 6 for example, Fig. 9 (05 Jul 2015 at ∼16:26 UTC) and Fig. 10 (07 Dec 2015 at ∼13:55 UTC~~as an example, shows~~) show the weighted mean profiles, the variation range of valid profiles and the number of valid profiles corresponding to different χ^2 thresholds. The profiles are shown as coloured curves which indicate the aerosol extinction coefficients in the three layers (i.e. σ_1, σ_2 and σ_3). ~~The distribution of χ^2 of this scanning cycle is already shown as the solid curves in .~~

~~The result shows~~

The results of both scanning cycles show that the retrieved profile is not sensitive to the threshold of χ^2 when there are sufficient number of valid profiles (~~for UV, χ^2 threshold exceeds ∼6 and~~ number of profiles exceeds ∼800 ~~, see the grey curve in (a); for VIS, χ^2 threshold exceeds~~ and ~~∼2 and number of profiles exceeds ∼~~400 ~~,~~ for UV and VIS, respectively, see the grey ~~curve in (b))~~curves in Fig. 9 and Fig. 10). This is because profiles with larger χ^2 have lower weight (w). In addition, when the threshold value is increased, more profiles with both higher and lower aerosol extinction coefficients are taken into account. As a result, the variation range of valid profiles becomes larger but the weighted mean remains similar. The result shows that the retrieval with a χ^2 threshold of 9 is stable, therefore, it is used in the study.

4.2 Estimation of the uncertainties of retrieved profiles

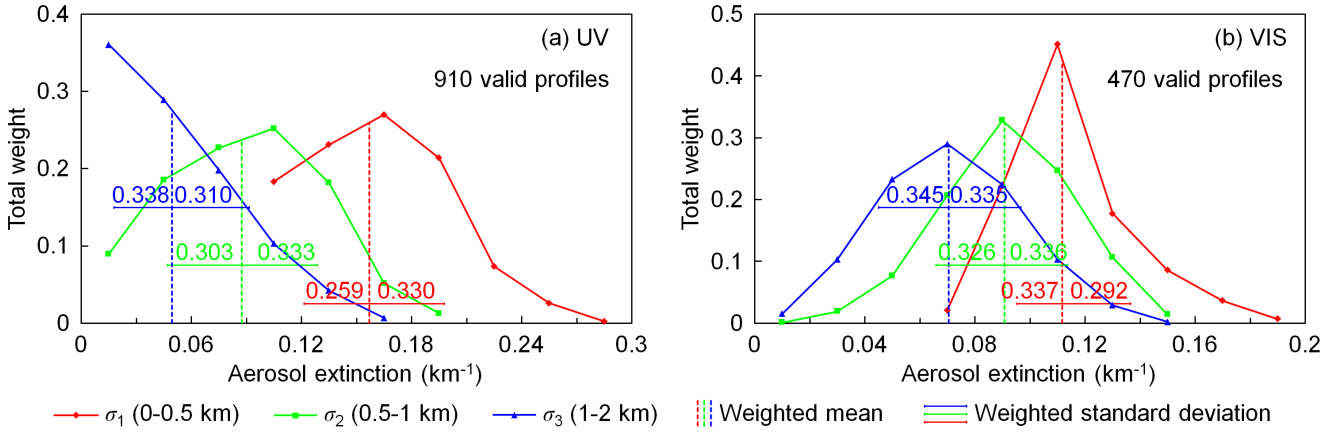

Figure 11. Weight distribution of valid profiles of (a) UV and (b) VIS bands, results of the scanning cycle on 05 Jul 2015 at ∼16:26 UTC (SZA ∼64°, RAA ∼97°). The weight distributions of the aerosol extinction coefficients of the three layers (σ_1, σ_2 and σ_3) are shown as solid curves with different colours. The vertical dashed lines indicate the weighted mean aerosol extinction coefficient of the three layers ($\sigma_1(\hat{\boldsymbol{x}})$, $\sigma_2(\hat{\boldsymbol{x}})$ and $\sigma_3(\hat{\boldsymbol{x}})$). The error bars indicate the weighted standard deviation calculated with Eq. (16) and (17). The numbers on the error bars refer to the total weight (w) of the profiles covered by each error bar.

~~Still taking the scanning cycle on 07 Dec 2015 at ∼13:55 UTC as an example~~

Still take the two measurement cycles mentioned in Section 4.1 as examples, we analyzed the weight distribution of valid profiles, see Fig. 11 and Fig. 12. The distributions of aerosol extinction coefficients in the three layers (σ_1, σ_2 and σ_3) are

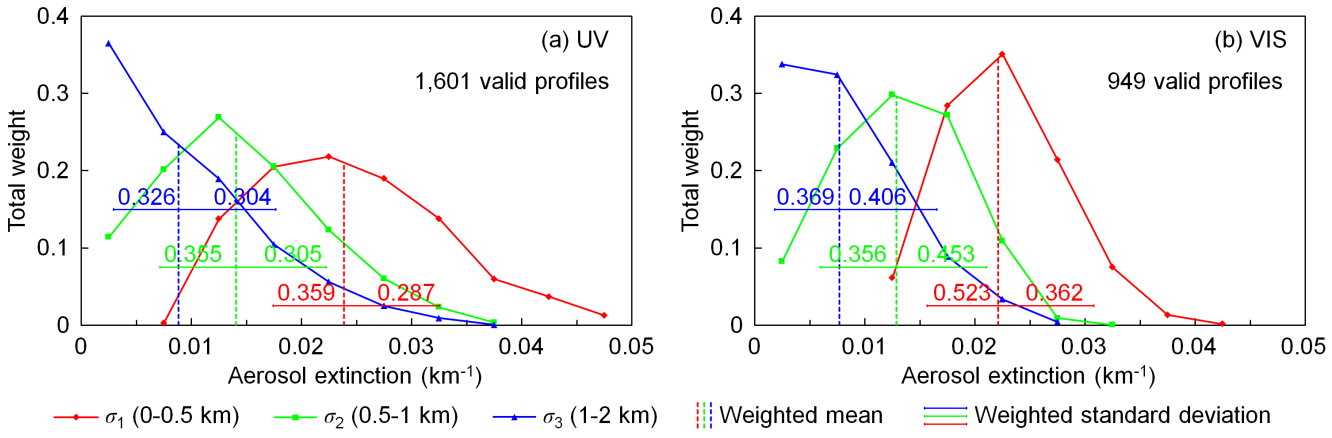

Figure 12. Same as Fig. 11, but for the scanning cycle on 07 Dec 2015 at ~13:55 UTC (SZA ~79°, RAA ~39°).

shown as solid curves. For each layer, aerosol extinction coefficients of all the valid profiles are grouped~~with a step size of 0.005 km^{-1}. The~~ , and he y-axis refers to the total weight of each group. The three vertical dashed lines indicate the weighted mean aerosol extinction coefficient of each layer (i.e. σ_1, σ_2 and σ_3 of $\hat{\boldsymbol{x}}$). The result shows that the distributions of σ_1, σ_2 and σ_3 are all asymmetric for both the UV and VIS bands. Especially for the layer of 1 – 2 km (σ_3) at UV band, the weight decreases monotonically with increasing aerosol extinction ~~. At UV band~~in both of the two cycles. Take the cycle shown in Fig. 12 (07 Dec 2015 at ~13:55 UTC) as example, there are altogether 205 (12.8%) and 120 (12.6%) valid profiles with $\sigma_3 = 0$ ~~, which contribute a total weight of~~ in UV and VIS bands, respectively. These profiles contribute total weights of 0.122 ~~. At VIS band, there are altogether 120 valid profiles with $\sigma_3 = 0$, which contribute a total weight of~~ and 0.101 for the UV and VIS retrievals, respectively.

In order to estimate the uncertainty of $\hat{\boldsymbol{x}}$, we calculate the weighted standard deviations of σ_1, σ_2 and σ_3 of all the valid profiles. Due to the asymmetric distribution, the weighted standard deviations are calculated separately for both left (negative) and right (positive) sides. For the l^{th} ($l = 1,2,3$) layer, denote the aerosol extinction coefficient of each profile as $\sigma_l(\boldsymbol{x})$, then the weighted standard deviation of the left side is calculated from all the valid profiles with $\sigma_l(\boldsymbol{x}) < \sigma_l(\hat{\boldsymbol{x}})$,

$$SD_l^- = \sqrt{\frac{\sum w(\boldsymbol{x}) \cdot [\sigma_l(\hat{\boldsymbol{x}}) - \sigma_l(\boldsymbol{x})]^2}{\sum w(\boldsymbol{x})}}, \boldsymbol{x} \in X_{\text{LUT}}, \chi^2(\boldsymbol{x}) \leq 1.5M, \sigma_l(\boldsymbol{x}) < \sigma_l(\hat{\boldsymbol{x}}), \tag{16}$$

and the weighted standard deviation of the right side is calculated from all the valid profiles with $\sigma_l(\boldsymbol{x}) > \sigma_l(\hat{\boldsymbol{x}})$,

$$SD_l^+ = \sqrt{\frac{\sum w(\boldsymbol{x}) \cdot [\sigma_l(\boldsymbol{x}) - \sigma_l(\hat{\boldsymbol{x}})]^2}{\sum w(\boldsymbol{x})}}, \boldsymbol{x} \in X_{\text{LUT}}, \chi^2(\boldsymbol{x}) \leq 1.5M, \sigma_l(\boldsymbol{x}) > \sigma_l(\hat{\boldsymbol{x}}), \tag{17}$$

The uncertainties of $\hat{x}$ are indicated as error bars in Fig. 11 and Fig. 12. For each layer, the total weight of the profiles covered by the error bar is labeled in the charts. At the UV band, the total weight of the valid profiles covered by the uncertainties is ~~63~~59 – 66%, which is close to the standard normal distribution. ~~At the VIS band~~However, the percentage ~~is 78 –~~ can be up to 90% at the VIS band. This is because the SNR of the measurement at the VIS band is higher. Therefore the retrieval of VIS band has higher selectivity, and the weight is more concentrated to the mean value.

4.3 Retrieval of synthetic measurement data

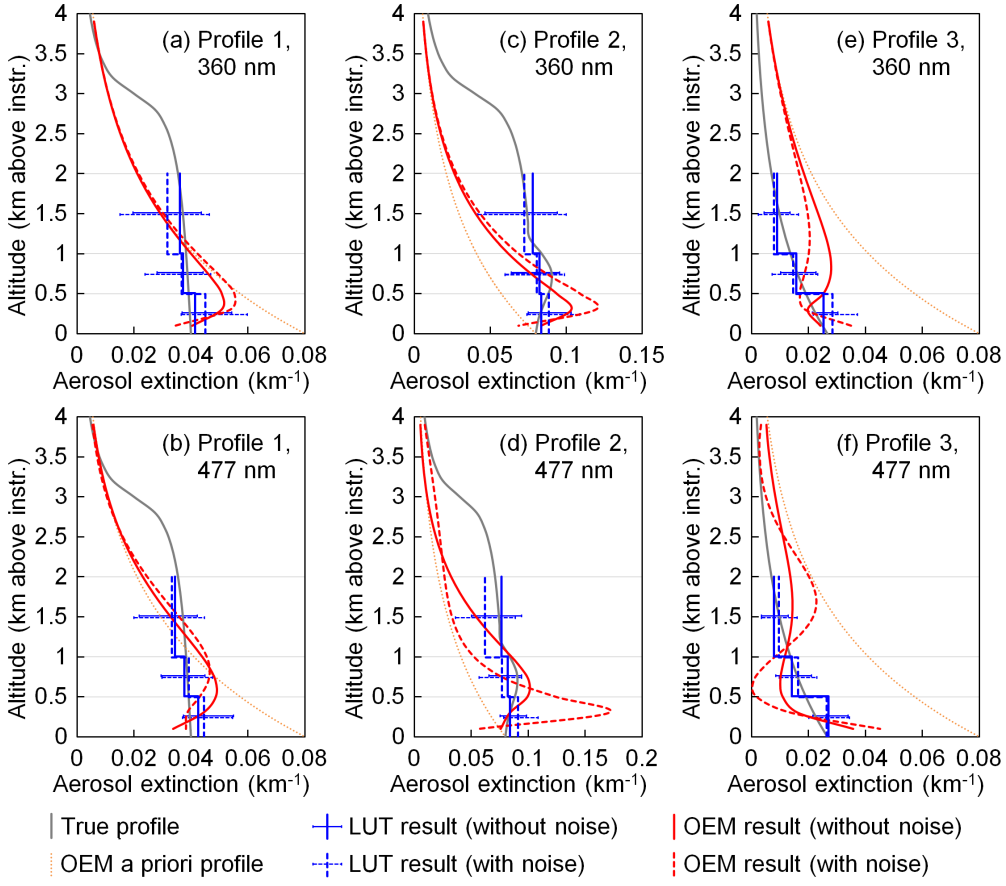

Figure 13. Retrieval results of three synthetic profiles. The gray curves show the true profiles, with which the synthetic O_4 DSCDs were simulated. The blue and red curves represent the profiles retrieved using our LUT (look-up table) algorithm and a typical OEM (optimal estimation method) algorithm, respectively. The sold blue and red curves represent the profiles retrieved from the original synthetic data, and the dashed curves represent the profiles retrieved from the synthetic data with random noised added. The error bars of the blue curves indicate the uncertainties calculated by Eq. (16) and (17). The dotted orange curves are the a priori profile used in the OEM retrieval.

In order to test the effectiveness of our retrieval algorithm, we generated some synthetic measurement data ~~and retrieved with~~ for the application to our algorithm. ~~shows the result of an artificial profile with the shape like a tangent curve. The~~ Fig. 13 shows the results of three representative synthetic profiles at 360 and 477 nm. In each chart, the true profile is shown as the gray ~~curves in . Aerosols are~~ curve. Profile 1 is a tangent curve with aerosols distributed between 0 and 6 km above instrument~~and the total AOD is 0.12~~. The aerosol extinction ~~coefficient~~ decreases with increasing altitude, which is 0.04 km^{-1} at surface level, ~~~96% of the surface aerosol extinction at 1 km above instrument, ~~89% at 2 km ~~,~~ and 50% at 3 km~~, and 0 at 6 km. As the aerosol extinction coefficient decreases slowly at low altitudes, ~~. The total AOD is 0.12, of which ~92% ~~of the total AOD~~ is contributed from the altitude below 3 km. ~~According to the long-term measurements of the co-located sun photometer and ceilometer, this profileis representative for the UFS~~Profile 2 has a similar shape as Profile 1, but the aerosol extinction between 0.5 and 1 km above instrument was enhanced. The aerosol extinction peaks at 0.75 km, and the average aerosol extinction coefficient between 0.5 and 1 km is larger than the bottom layer by ~10%. In addition, the aerosol extinction coefficients at other altitudes are increased by a factor of 2 comparing to Profile 1. Profile 3 is an exponential profile. The total AOD is 0.12, the scaling height is 1.5 km, and the surface aerosol extinction coefficient is 0.03 km^{-1}.

We first simulated O_4 DSCDs at 360 and 477 nm with ~~the profile, and the~~ each profile. The solar position was set as SZA = 60° and RAA = 60°~~. The solid blue curves in show the profiles retrieved with our algorithm~~, and the ~~error bars indicate the uncertainties calculated by Eq. (16)and (17)~~other parameters followed the settings used in calculating the look-up table listed in Table 5 (excluding the aerosol extinction coefficients above 2 km). In order to test the stability of the retrieval, we ~~added a~~ also generated a set of noisy data for each profile and each wavelength by adding random noise to the simulated O_4 DSCDs. We assume the measurement noise ~~of~~ at all elevation angles ~~are the same which~~ is the same and follows a normal distribution with ~~the~~ a standard deviation of 2% of the DSCD of the lowest elevation angle. This noise level is realistic for the measurements at the UFS. ~~The profiles retrieved from the noisy data are shown as~~

Aerosol profiles were then retrieved from both the original and noisy synthetic data using our algorithm. In the error estimation, the DOAS fitting error (ϵ_{fit}) was defined as the average values of the UFS measurements, while the other six kinds of errors followed the common settings presented in Section 3.7. O_4 DSCD correction was not applied. The solid and dashed blue curves in ~~. At both 360 and 477 nm, the retrieved profiles~~ Fig. 13 show the profiles retrieved from the original and noisy data, respectively, and the error bars indicate the uncertainties calculated by Eq. (16) and (17). The results show that for Profile 1 and Profile 3, our retrieval algorithm can well reproduce the true ~~profile. Our LUT based retrieval is considered to be stable, as the results are very similar for both cases with and without noise.~~ profiles from not only the original data but also the noisy data. For Profile 2, the retrieved profile cannot reproduce the elevated layer, but the error bar covers the aerosol extinction of the true profile. This is because the retrieval is ill-posed, which means the limited input information does not correspond to a unique profile with elevated layer, instead, many other profiles without the elevated layer can also fit the input information. Adding noise to the synthetic data can affect the retrieved aerosol extinction coefficients, however the influence is small in most cases. In addition, the noise can amplify the uncertainty of retrieved profile. The results indicate that our LUT-based retrieval is stable.

We also retrieved the synthetic data ~~with and without noise using a typical OEM profile retrieval algorithm . An~~ using the bePRO profiling tool developed by BIRA-IASB (Clémer et al., 2010; Hendrick et al., 2014). It is an OEM-based algorithm and uses LIDORT as the forward model. In the retrieval of all the six cases, the a priori profile was defined as an exponential profile with AOD~~of~~ = 0.12 and scaling height~~of~~ = 1.5 km~~was used as the a priori profile in the OEM retrieval, shown as the dotted orange curve in .~~, shown as the dotted orange curve in each panel of Fig. 13. The vertical grid was defined as 20 layers of 200 m thickness each. For Profile 1 and Profile 2, the uncertainty covariance matrix of a priori ($\mathbf{S}_a$) was defined as in Clémer et al. (2010) and Wang et al. (2014a): the diagonal elements corresponding to the bottom layer, $\mathbf{S}_a(1,1)$, was set as the square of a scaling factor β ($\beta = 0.2$) times the maximum partial AOD of the profiles; the other diagonal elements decrease linearly with increasing altitude to $0.2 \times \mathbf{S}_a(1,1)$; the off-diagonal elements of $\mathbf{S}_a$ were defined using Gaussian functions with correlation length $\gamma = 0.05$ km. For Profile 3, as the difference between the true and a priori profiles is quite large, we set $\beta = 0.4$ and $\gamma = 0.1$ km, so that the constrain from the a priori profile is weaker. The measurement uncertainty covariance matrix ($\mathbf{S}_\epsilon$) was also defined as in most of the other MAX-DOAS studies that $\mathbf{S}_\epsilon$ is a diagonal matrix with variances equal to the square of the DOAS fitting error (ϵ_{fit}^2). We defined ϵ_{fit} as same as in the LUT retrieval, but the other six error sources were not included. The retrieval parameters related to the radiative transfer simulation followed the settings of our LUT-based retrieval.

The results retrieved from the data with and without noise are shown in Fig. 13 as solid and dashed red curves, respectively. ~~For the noise-free case, the profiles retrieved with the OEM algorithm are unrealistic and aerosol extinction varies in a large range between adjacent layers. In addition, the profiles cannot~~ In all the 12 retrieval cases, the O_4 DSCDs simulated with retrieved profiles are well correlated to the input values (the relative root mean square error varies between 0.7% and 4.7%). However, as the retrieval is ill-posed, the retrieved profiles cannot well reproduce the true profile. Especially at high altitudes (above 1 km), the retrieved profiles are mostly dominated by the a priori profile. The OEM retrieval is also ~~unstable, as not only the aerosol extinction but also the shape of the profile is significantly changed when noise is added to the synthetic data. The result indicates~~ sensitive to measurement noise, which can be seen from the large variations of profile shape and aerosol extinction. The results indicate that the LUT based algorithm is much more suitable for ~~high altitude measurements~~ measurements with low SNR.

4.4 Comparison to sun photometer ~~measurement~~measurements

Fig. 14 shows the comparison of AOD measured by MAX-DOAS and sun photometer during the entire study period. The ~~seasonal average~~ seasonally averaged AOD measured by both instruments are listed in Table 7. ~~The~~ As the AOD measured by MAX-DOAS refers to the AOD between 0 and 2 km ~~(i.e. $\tau_{2k}(\hat{\boldsymbol{x}}) = 0.5\sigma_1(\hat{\boldsymbol{x}}) + 0.5\sigma_2(\hat{\boldsymbol{x}}) + \sigma_3(\hat{\boldsymbol{x}})$),~~ while the AOD measured by ~~the~~ sun photometer refers to the total AOD~~. Therefore, AODs measured by~~, the sun photometer results should be larger~~than AODs measured by the MAX-DOAS~~. Despite of the difference, the time series (panels ~~a and c~~ (a) and (c) of Fig. 14) show that the AODs measured by both instruments have a similar seasonal variation with higher AOD in summer and lower AOD in winter. The monthly average data show that the difference between the AODs measured by MAX-DOAS and sun photometer is much larger in summer, this coincides with the ceilometer profiles shown in Fig. 1 which indicate much higher aerosol

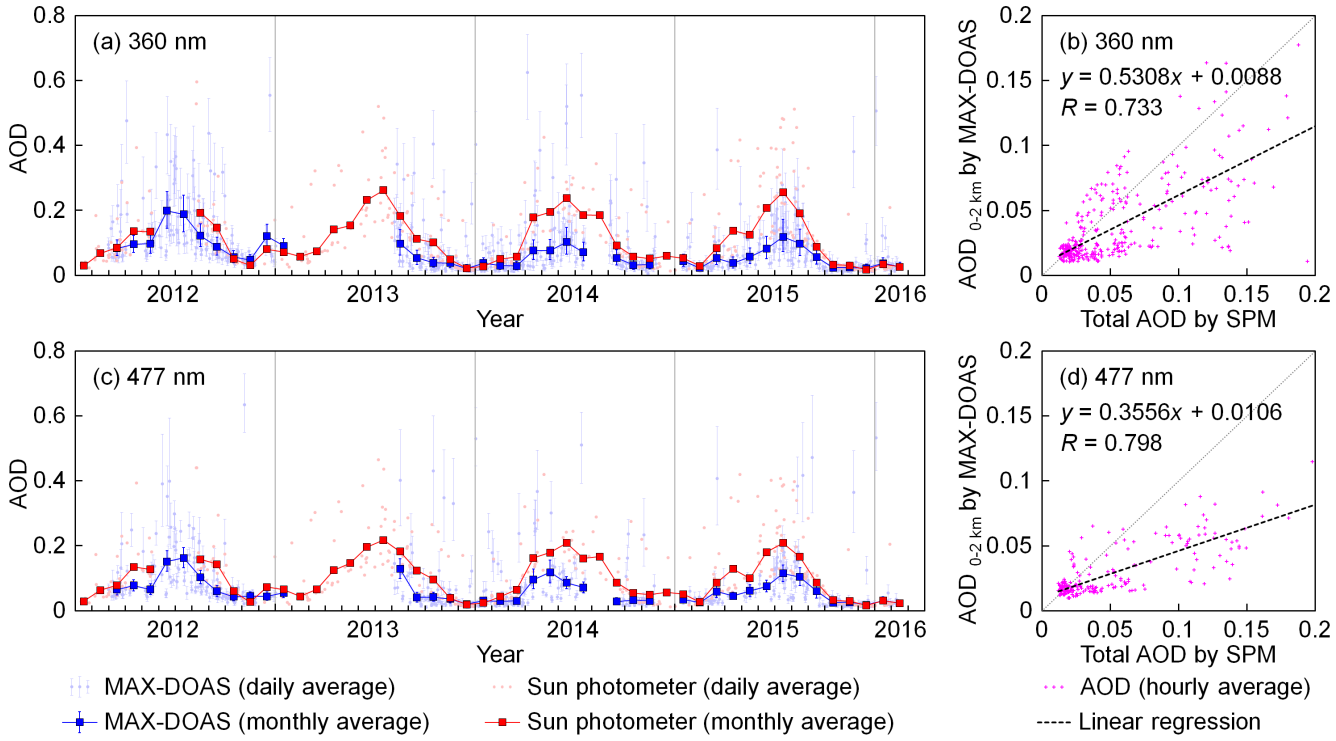

Figure 14. Comparison of AODs at (a, b) 360 nm and (c, d) 477 nm measured by MAX-DOAS and sun photometer. The charts on the left side (a, c) show the daily and monthly averaged time series, whereas the scatter plots on the right side (b, d) show the hourly averaged results. The AOD measured by MAX-DOAS refers to the vertical range between 0 and 2 km (i.e. $\tau_{2k}(\hat{\boldsymbol{x}}) = 0.5\sigma_1(\hat{\boldsymbol{x}}) + 0.5\sigma_2(\hat{\boldsymbol{x}}) + \sigma_3(\hat{\boldsymbol{x}})$) above the instrument (i.e. 2,650 – 4,650 m a.s.l.). The measurements were available during daytime with SZA < 85° and cloud-free conditions. The AOD measured by the sun photometer refer to the total AOD, and only the measurements during 10:00 – 14:00 UTC were used for reasons of their accuracy. The daily and monthly averaged results are calculated from all the available hourly averaged AODs, therefore they are not real monthly and daily averages. The error bars of the MAX-DOAS data refer to the averages of the uncertainties calculated by Eq. (16) and (17). A few data points are outside the scatter plots.

extinction coefficients above 2 km in summer. The underestimation of MAX-DOAS may also be related to the decreased sensitivity of measurement at higher altitudes.

The correlation between hourly averaged AODs measured by MAX-DOAS and sun photometer is shown in Fig. 14 (b, d). AODs ~~measured by MAX-DOAS~~ show a general agreement ~~with sun photometer measurements at both UV and~~ at the UV and the VIS bands with correlation coefficients of $R = 0.733$ and 0.798, respectively. However, AODs from MAX-DOAS are lower, consequently the slope of the regression lines are 0.5308 and 0.3556 for UV and VIS bands, respectively. As the MAX-DOAS only reports AODs below 2 km while the sun photometer measures the total AODs, the MAX-DOAS AODs are indeed expected to be lower. This is in particular true in cases of large AODs due to very strong convection of polluted air

Table 7. Seasonally averaged AODs measured by the MAX-DOAS and sun photometer at the UFS. The AODs measured by MAX-DOAS refer to the AODs between 0 and 2 km above instrument (i.e. 2,650 – 4,650 m a.s.l.), and the ~~meausrements~~ measurements were available during the daytime with SZA < 85° and no cloud; the AODs ~~meausred~~ measured by sun photometer refer to the total AOD, and the measurements were only available during 10:00 – 14:00 UTC. The results listed in the table are calculated from all the available hourly averaged AODs.

Season	AOD (0 – 2 km) measured by MAX-DOAS		Total AOD measured by sun photometer	
	360 nm	477 nm	360 nm	477 nm
Spring (MAM)	0.064	0.065	0.106	0.101
Summer (JJA)	0.121	0.114	0.214	0.184
Autumn (SON)	0.048	0.040	0.070	0.068
Winter (DJF)	0.028	0.024	0.037	0.033

masses from the valley and/or the presence of Saharan dust layers. Then, particles are often transported beyond the range of the MAX-DOAS measurements and the disagreement is largest. This feature might be strengthened by the decreased sensitivity of the MAX-DOAS measurement at higher altitudes, so that the upper part of an aerosol layer is missed. In addition, a few data points lie above the 1:1 reference lines~~, which indicates that the AODs measured by MAX-DOAS were occasionally higher than the sun photometer measurements~~. This might be explained by the inhomogeneous distribution of aerosols in horizontal direction. The light paths of the MAX-DOAS and the sun photometer are different. MAX-DOAS measures scattered sunlight while sun photometer derives ~~AODs~~ the AOD from direct sun measurements. Therefore, when the aerosol load along the light path of MAX-DOAS is higher than that of the direct sun measurement, the AOD measured by the MAX-DOAS may exceed the AOD measured by the sun photometer. ~~Moreover, for~~ For most of these points, the difference between the results of the two instruments is within ~~the uncertainty of the MAX-DOAS result defined by Eq.(16), therefore some of these points are~~ their uncertainty ranges, i.e., the disagreement is probably due to the measurement ~~error.~~ and retrieval errors.

4.5 Temporal variation ~~characteristic~~ of ~~aerosols~~aerosol characteristics

The seasonally averaged aerosol extinction profiles derived from the long-term measurements are shown in Fig. 15. The result indicates that the aerosol load is high in summer and low in winter~~. This~~ , which coincides with the ceilometer results shown in Fig. 1. The seasonal pattern can be explained by the higher biogenic emissions from vegetation in summer. Moreover, the mixing layer is higher in summer, thus anthropogenic aerosols are more likely dispersed to upper altitudes. The ~~result also shows that the~~ shape of the profiles also agree with the ceilometer results that the averaged aerosol extinction decreases with increasing altitude in all seasons – taking into account the coarse vertical resolution ~~.~~ of the MAX-DOAS. In addition, Fig. 15 shows a much larger vertical gradient at 360 nm in summer. This might be explained by the lower sensitivity of the UV measurement for higher altitudes due to the more decreased visibility at shorter wavelength.

We compared the ~~seasonal average~~ seasonally averaged aerosol extinction coefficients at 360 and 477 nm in the bottom layer (0 – 0.5 km above the instrument, σ_1), see Fig. 16. The averaged aerosol extinction coefficients are shown as bar charts. The

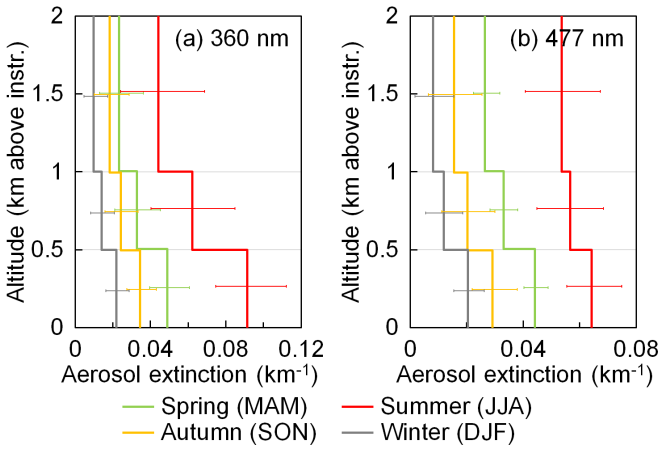

Figure 15. Seasonal average aerosol extinction profiles for (a) 360 and (b) 477 nm derived from the long-term measurement results. The error bars represent the averages of the uncertainties calculated by Eq. (16) and (17).

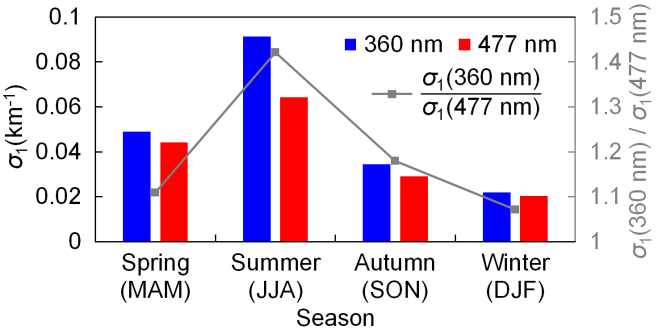

Figure 16. Comparison of seasonal average aerosol extinction coefficients at 360 and 477 nm in the bottom layer (0 – 0.5 km above instrument, σ_1). The coloured bars show the average aerosol extinction coefficients of the four seasons (equal to the bottom values shown in Fig. 15). The grey square markers indicate the ratios between the aerosol extinction coefficients at 360 and 477 nm.

ratio between the aerosol extinction coefficients at 360 and 477 nm is indicated by the grey curve. The result shows that the aerosol extinction coefficient ratio between 360 and 477 nm is significantly higher in summer than in the other seasons.

From these ratios the Ångström ~~exponents (AEs) can easily~~ exponent (AE) can be calculated using the seasonally averaged surface aerosol extinction coefficients at 360 and 477 nm. The results are listed in Table 8. The seasonal averaged AEs of 380 – 500 nm from the AERONET measurements at Hohenpeißenberg from ~~Apr~~ April 2013 to ~~Feb~~ February 2016 are also listed for comparison. The result shows that both the UFS and Hohenpeißenberg measured the highest AE in summer and the lowest in winter. The AE at the UFS is in general lower than that measured at Hohenpeißenberg with a smaller difference in summer. This can be explained by the different altitude of the two sites. As the AERONET station at Hohenpeißenberg is located at

~950 m a.s.l., larger contribution of anthropogenic aerosols is expected. The extremely low AE at the UFS in spring, autumn and winter agrees with the result measured at a plateau site (Lhasa, China, 3,688 m a.s.l.) reported in Xin et al. (2007). The annual mean AE at that site is reported to be 0.06 ± 0.31, which is significantly lower than those measured at low-altitude sites, especially urban and forest sites. In general, ~~smaller AEs imply~~ a smaller AE implies larger aerosol particle sizes (Dubovik et al., 2002). The increased AE at UFS in summer indicates a larger contribution of fine particles. The result is consistent with the fact that the particle size ~~is smaller in summer and implies larger contribution of fine particles being~~ of biogenic secondary aerosols is in general smaller than ice particles transported from the lower altitudes to upper altitudes ~~.~~ in summer.

Table 8. Seasonal average Ångström exponents (AEs) obtained from MAX-DOAS near-surface measurements (0 – 0.5 km above instrument) and from AERONET measurements at Hohenpeißenberg. The results of MAX-DOAS are calculated from the ratios between the seasonal average aerosol extinction coefficients at 360 and 477 nm (i.e. the ratios shown in Fig. 16). The results of AERONET are the seasonal average values of AEs (380 – 500 nm) at Hohenpeißenberg from Apr 2013 to Feb 2016.

Season	AE from UFS MAX-DOAS	AE from AERONET at Hohenpeißenberg
Spring (MAM)	0.37	1.26
Summer (JJA)	1.25	1.38
Autumn (SON)	0.59	1.05
Winter (DJF)	0.24	0.47

5 Summary and conclusions

We have developed a new MAX-DOAS aerosol profile retrieval algorithm ~~for MAX-DOAS measurements at high altitude sites. This is challenging as the AODs are typically quite low. The algorithm is~~ based on a parameterized O_4 DSCD look-up table. The algorithm is applied to the long-term MAX-DOAS ~~measurement~~ measurements at the UFS, ~~located at an altitude of~~ Germany, a high altitude site located at 2,650 m a.s.l. ~~Aerosol measurements from February 2012 to February 2016 are considered.~~

Observations of O_4 ~~absorption~~ absorptions at both 360 and 477 nm ~~are analyzed. Due to the low SNR, commonly used MAX-DOAS retrieval algorithms based on the optimal estimation method are not suitable for the retrieval of high altitude measurements. In order to better design the O_4 DSCD look-up table, we~~ were analyzed. We first investigated the sensitivities of O_4 absorption to ~~ground topography, surface albedo, single scattering albedo, scattering phase function, aerosols at different altitude and surface aerosol extinction. The O_4 DSCD look-up table was then parameterized based on the results of the sensitivity study.~~ several parameters. According to the sensitivity analysis result, we defined ~~a set of possible aerosol extinction profiles and simulated the~~ an aerosol profile set which consists of 7,553 possible profiles and then simulated O_4 DSCDs with all the ~~possible profiles and~~ profiles and all possible observation geometries. In the retrieval of each measurement cycle, the simulated O_4 DSCDs corresponding to all the possible ~~profile~~ profiles are obtained from the look-up table. The cost functions (χ^2) are calculated for each possible profile according to the simulated and measured O_4 DSCDs as well as the mea-

surement uncertainties. A comprehensive error analysis ~~was performed to better~~ is performed to estimate the total uncertainty. ~~The errors from DOAS fitting, temperature, ground topography simplification, ground surface albedo, single scattering albedo, phase function and aerosols above retrieval height are considered.~~ Valid profiles are selected from the profile set according to the cost function. The optimal solution is defined as the weighted mean of the valid profiles. ~~Our analysis shows that the weighted mean profile is almost insensitive to the threshold of χ^2. The uncertainty of the solution is defined as the weighted standard deviation of the valid profiles.~~

One key result of our study is that an elevation dependent O_4 DSCD scaling factor is needed to bring ~~measurements and model results~~ measured and simulated O_4 DSCDs into agreement. Assuming the look-up table covers all ~~the~~ possible aerosol profiles under clear sky conditions, we determined the scaling factors based on the statistical analysis of the long-term ~~measurement. At the moment we have no clear explanation for this finding, it might be related to the specific properties of the high altitude station, e.g. the highly structured topography, horizontal gradients of the aerosol extinction and the systematic dependence of the surface albedo on altitude.~~ measurements. The agreement between measured and simulated O_4 DSCDs is greatly improved by ~~the~~ this correction.

In addition, we developed a simple cloud screening method which is based on the statistical analysis of the colour index. The developed cloud screening method is applied to the long-term ~~measurement~~ measurements to filter out data taken under cloudy conditions.

In order to test the effectiveness of the algorithm, we retrieved profiles from synthetic ~~measurement~~ data. The results indicate that our algorithm can well reproduce the true profile, and the retrieval is stable to measurement noise.

The ~~AODs~~ AOD retrieved from the long-term MAX-DOAS measurements ~~using our developed inversion technique are~~ was compared to the sun photometer observations at the UFS. The results show reasonable agreement with each other~~with correlation coefficients (R) of 0.733 and 0.798 for measurements at UV and VIS bands, respectively~~. However, especially in summer the sun photometer results are systematically larger (by about a factor of 2) than the MAX-DOAS results. This discrepancy is due to the different ~~definition of AODs~~ definitions of AOD measured by MAX-DOAS and sun photometer~~, and also probably related to the decreased sensitivity of the MAX-DOAS measurements at higher altitudes. It becomes relevant in cases of large AODs when Saharan dust was present or strong convection occurred~~. The larger difference in summer also coincides with the ceilometer measurements at the UFS which indicate larger aerosol extinctions at high altitude in summer. The long-term observation results show that the aerosol load at the UFS is higher in summer and lower in winter. Higher AOD in summer is mainly related to a higher frequency of extended mixing layers that allows ~~anthropogenic pollutants~~ particles to disperse from lower to upper altitudes. According to the MAX-DOAS measurements~~the~~, the mean aerosol extinction decreases with increasing altitude for all seasons~~. The Angstr~~, this agrees with the ceilometer measurements. The Ångström exponent derived from MAX-DOAS surface measurement is higher in summer and extremely low in winter, which implies a smaller particle size in summer. This might be due to a significant contribution from biogenic sources in summer.

The study demonstrated that the developed method is effective for MAX-DOAS measurements at the UFS. Since the profile set only consists of reasonable profiles ~~,~~ and the final ~~solutions are~~ solution is calculated from the weighted ~~means of all the~~ mean of all valid profiles, ~~as well as the~~ and from the fact that the retrieval does not rely on a priori profiles, many of the

limitations of ~~the~~ retrieval algorithms based on the optimal estimation method are overcome. In addition, as the O_4 DSCDs of all ~~the~~ possible profiles are pre-calculated, our method significantly reduces the computational time, so that real-time ~~retrieval is~~ retrievals should be possible.

Appendix A: Cloud screening method

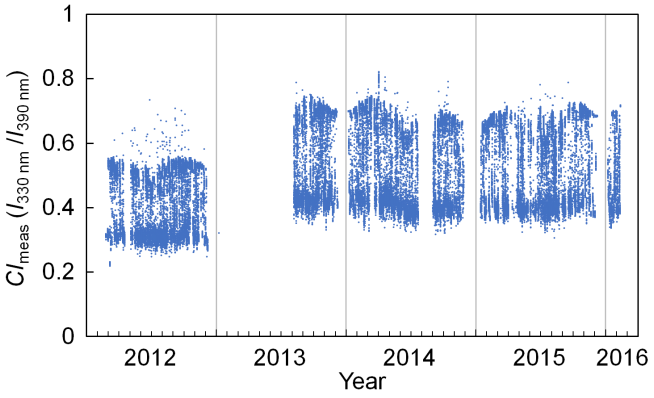

Figure A1. Time series of CI_{meas} calculated from the zenith UV spectra measured during the entire study with 30° < SZA < 70°.

In this study, the colour index (CI) is defined as the ratio of radiative intensities at 330 and 390 nm. Measured CIs (denoted as CI_{meas}) were calculated from the zenith UV spectra (offset and dark current corrected) by taking the ratio of the counts at 330 and 390 nm. Fig. A1 shows the time sereies of CI_{meas} calculated from all the zenith spectra with 30° < SZA (solar zenith angle) < 70° during the entire study. The result shows that the variation range of CI_{meas} is stable within the two periods. However, the optical throughput of the instrument in the UV spectral range has been enhanced after a regular maintenance of the optical system in 2013. Hence, the CI increased systematically in the second period. Therefore, calibration of CI_{meas} is necessary in order to make the CI_{meas} measured during the two periods comparable to each other. The calibration was done following the method suggested in Wagner et al. (2016). CI_{meas} measured under overcast skies were fitted to the simulated minimum CI. The correction factor was determined to be 2.70 and 2.06 for the periods of 02.2012~~1000~~ – 01.2013 and 08.2013~~1000~~ – 02.2016, respectively. CI_{meas} was subsequently converted to CI_{cal} (calibrated CI) by multiplying the corresponding correction factor.

Fig. A2 shows the frequency distribution of CI_{cal} measured with different SZAs. The CI_{cal} from the long-term ~~measurement~~ measurements were grouped by their SZA with a step size of 2°. The relative frequency distributions are colour coded. The result shows a bimodal frequency distribution of CI_{cal} for all SZAs. The peaks with lower and higher CI are corresponding to measurements under overcast and clear skies, respectively. This pattern is similar to the CI measured on Jungfraujoch, Switzerland (3570 m a.s.l.) reported in Gielen et al. (2014), and different from the results measured at the low-altitude sites reported in Gielen et al. (2014); Wagner et al. (2016). This is because the high altitude sites are seldom influenced by anthropogenic aerosols, hence the sky is either clear or covered by cloud or fog during most of the time. Based on this feature, we defined

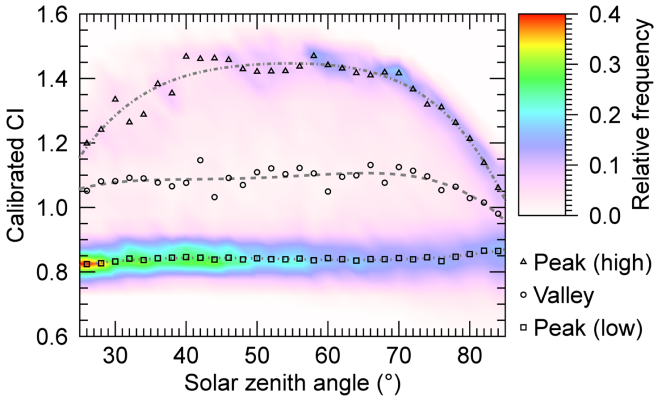

Figure A2. Distribution pattern of CI_{cal} during the entire study. Data were grouped by SZA with an interval of 2°. For each group, frequency was counted for bins of 0.05. Peak and valley values (shown as markers) were determined by Gaussian fit. The curves are the results of 4$^{\text{th}}$ order polynomial regressions of each data series.

the threshold for cloud screening as the CI_{cal} with the minimum probability between the two peaks (denoted as $CI_{\text{cal, valley}}$). The $CI_{\text{cal, valley}}$ was determined by fitting the probability density function to a Gaussian function. The circle markers shown in Fig. A2 indicates the determined $CI_{\text{cal, valley}}$. In order to minimize the noise, the $CI_{\text{cal, valley}}$ was fitted to a 4$^{\text{th}}$ order polynomial. The resulting smoothed $CI_{\text{cal, valley}}$ was used as the threshold (indicated as dashed curve in Fig. A2). Based on this approach, ∼60% of the zenith measurements were determined as cloudy scenes, and the corresponding scanning cycles were not used in the following analysis.

Appendix B: Result of the sensitivity studies

We investigated the sensitivity of O_4 absorption to surface albedo, single scattering albedo (SSA), scattering phase function, aerosol extinction at different altitude, aerosol extinction above retrieval height, and surface aerosol extinction. In the test for each parameter, O_4 DSCDs at 360 and 477 nm and at the six off-zenith elevations were simulated with ~~all other parameters fixed to their median values. In~~ the parameter being tested set as different values, while all the other parameters were fixed. In this section, we only present the results of the sensitivity tests under the common settings listed in Table B1. In the following subsections, all the ~~simulations, the surface was defined as a flat surface~~ unmentioned simulation parameters followed the common settings. The extreme and median values of each parameter are also discussed in the following subsections.

B1 Sensitivity to surface albedo

It is difficult to estimate the surface albedo around the measurement site. In other studies, the surface albedo at low altitude sites was usually estimated to be 0.05 – 0.1 (e.g., Irie et al., 2008; Ma et al., 2013; Wagner et al., 2011; Chan et al., 2017; Li et al., 2010; Clémer et al., 2010; Li et al., 2013; Wang et al., 2016), while at a high altitude site, it was estimated to be 0.2 (Franco

Table B1. The common settings for sensitivity studies.

Parameter	Value or definition
Topography	Flat surface at an altitude of 2,650 m a.s.l.
Solar zenith angle (SZA)	60°
Relative solar azimuth angle (RAA)	60°
Surface albedo	0.1
Single scattering albedo (SSA)	0.93 (see Section 3.3) . All the examples shown in this section were simulated with the solar position set as SZA
Phase function	The 'median' phase function defined in Appendix B3
Aerosol extinction profile	Box-shape profile with AOD = 60° and RAA0.12 and box-height = 60°, which are close to the median values of (i.e. $\sigma = 0.04\,km^{-1}$ for 2.65 – 5.65 km a.s.l. and $\sigma = 0$ for altitude > 5.65 km)
Climatology	US standard profiles for profile, temperature and trace gas profiles

et al., 2015). As for the UFS, on one hand, the snow covers and naked rocks are more reflective than the typical urban and rural surfaces; on the other hand, the deep valleys close to the site can significantly decrease the surface albedo. In addition, the measurements at different elevation angles are sensitive to different parts of surface. The effective surface albedo also depends on the observation geometry. The forming and melting of the snow cover can affect the surface albedo as well. However, the RTM can only assume a constant surface albedo. Therefore, we have to estimate a variation range of the surface albedo and consider the possible uncertainty in the retrieval. In this study, we empirically estimate that the surface albedo varies between 0.025 and 0.2 with a median value of 0.1 for both 360 and 477 nm.

In order to estimate the uncertainty of simulated O_4 DSCDs at 360 and 477 nm were simulated DSCD due to the surface albedo, we simulated O_4 DSCDs with extreme surface albedo values (0.025 and 0.2) and the median value (0.1). Simulations were done with both an aerosol-free profile and a , while the other parameters were fixed as the settings listed in Table B1. Besides the box-shape profile with AOD = 0.12and box height = 3 km. shows the , we also did a test with an aerosol-free profile. The relative differences of the O_4 DSCDs simulated with extreme surface albedo values compared to those simulated with the median value in the both studiesare shwon in Fig. B1.

The result shows that at both 360 and 477 nm, O_4 DSCDs of all the elevation angles slightly decrease with increasing surface albedo, and the variation rate differs with different elevation angle angles and different aerosol loadloads. Based on our estimation of the variation range of surface albedo, if the estimated median value (0.1) is used in the forward simulation, the uncertainty caused by the surface albedo assumption would be less than 3%, and the positive and negative errors are nearly equal. Our further simulations also show that the uncertainty caused by surface albedo depends on the observation geometry. In the following simulations hereafter, the surface albedo was set to 0.1 unless otherwise mentionedaerosol profile retrieval, we use a simple look-up table to determine the simulation error caused by surface albedo (see Section 3.7.2).

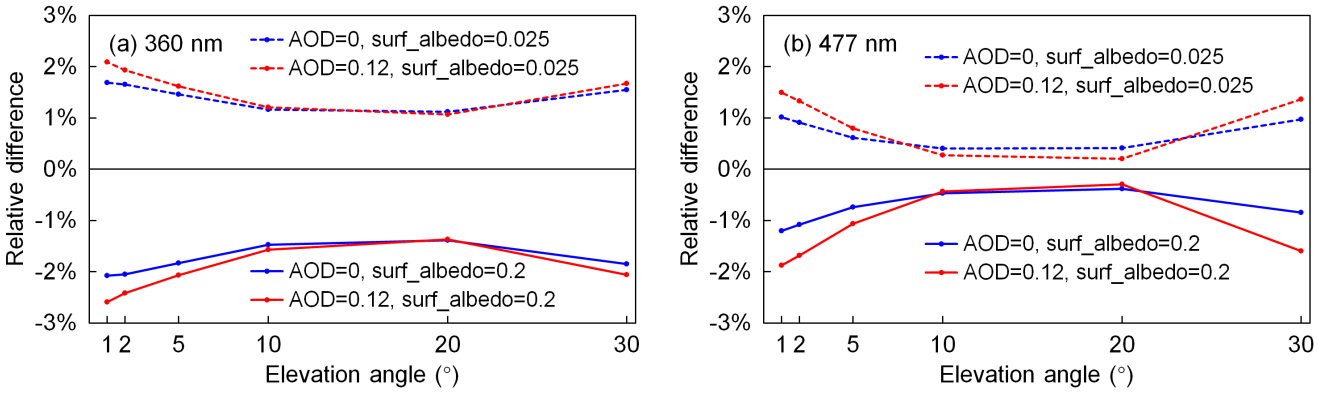

Figure B1. Relative differences of O_4 DSCDs at (a) 360 nm and (b) 477 nm simulated with extreme surface albedo values (solid lines for 0.2 and dashed lines for 0.025) compared to O_4 DSCDs simulated with the median value (0.1). Blue lines refer to the results under aerosol-free condition, while red lines refer to the results with a box-shape profile with AOD = 0.12 and box height = 3 km. The other simulation parameters followed the settings listed in Table B1.

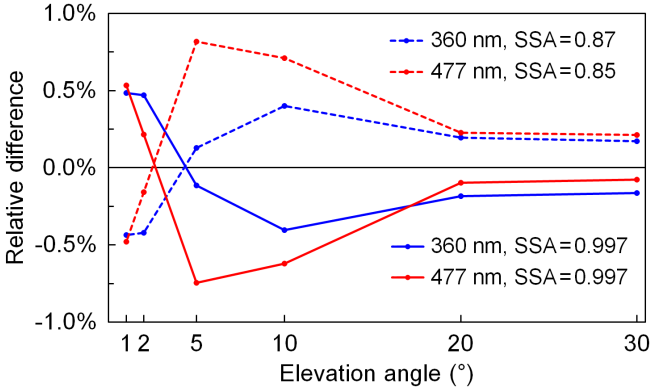

Figure B2. Relative differences of O_4 DSCDs at 360 nm (blue lines) and 477 nm (red lines) simulated with extreme single scattering albedo values (solid lines for larger extreme value and dashed lines for smaller extreme value) compared to O_4 DSCDs simulated with the median value (0.93 for 360 nm and 0.92 for 477 nm). The other simulation parameters followed the settings listed in Table B1.

B2 Sensitivity to single scattering albedo

As aerosol optical property data at the UFS are not available, and we use the AERONET data at Hohenpeißenberg instead. According to the long-term data, for the single scattering albedo (SSA) at 360 nm, 90% of the data vary between 0.87 and 0.997, and the median value is 0.93; for the SSA at 477 nm, 90% of the data vary between 0.85 and 0.997, and the median value is 0.92.

In order to estimate the uncertainty of simulated O_4 ~~DSCDs at 360 and 477 nm~~ DSCD due to the SSA, O_4 DSCDs were simulated with the median and extreme SSA values (0.87, 0.93 and 0.997 for 360 nm; 0.85, 09.2 and 0.997 for 477 nm)~~. In all the simulations, aerosol profile was defined as a box-shape profile with AOD = 0.12 and box height = 3 km~~, while the other parameters were fixed as the settings listed in Table B1. The relative differences between the O_4 DSCDs simulated with extreme and median SSA values are shown in Fig. B2.

The result indicates that using the median SSA in the forward simulation would result in less than 1% error in O_4 DSCDs in 90% of the cases. In addition, the positive and negative errors are mostly equal. Although the ~~measurement of SSA are taken from~~ measurements of SSA were taken at a much lower altitude site, the sensitivity result shows the error attributed to SSA is rather small (<1%). Therefore, using the SSA values from Hohenpeißenberg should not have a big influence on the retrieval. ~~From hereafter, all radiative transfer simulations assume SSA of 0.93 for 360 nm and 0.92 for 477 nm unless otherwise mentioned~~Since the simulation error caused by SSA can be influenced by the aerosol load as well as the observation geometry, it is determined using a simple look-up table in our aerosol profile retrieval (see Section 3.7.2).

B3 Sensitivity to scattering phase function

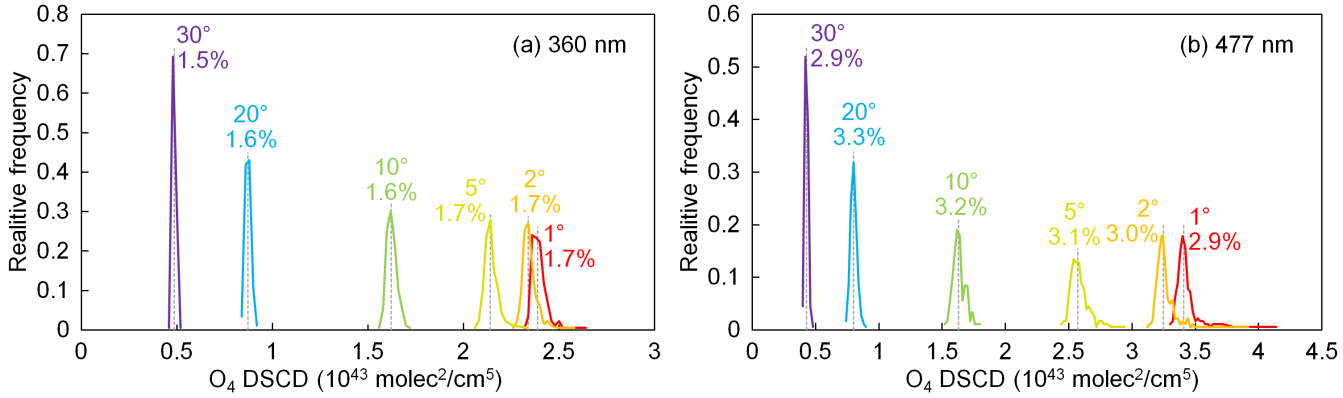

Figure B3. Frequency distribution of O_4 DSCDs at (a) 360 nm and (b) 477 nm simulated with all the phase functions during 2013 – 2014. The other simulation parameters followed the settings listed in Table B1. The percentage standard deviations of the simulated O_4 DSCDs at each elevation angle are labeled in the plots. The grey dashed lines represent the median values of simulated O_4 DSCDs at each elevation angle.

The ~~sensitivity of~~ estimation of the uncertainty of simulated O_4 ~~DSCDs~~ DSCD due to scattering phase function ~~was estimated by using all the phase functions measured by the AERONET station from 2013 to 2014 in the forward simulation of~~ is also based on the AERONET data at Hohenpeißenberg. Unlike most of the other simulation parameters which can be defined by a single number, the parameter of scattering phase function is defined by function values at different scattering angles. In order to estimate the uncertainty, we simulated O_4 DSCDs with ~~a fixed aerosol profile (a box-shape profile with AOD = 0.12 and~~

~~box height = 3 km)~~all the phase functions from 2013 to 2014 (altogether 179 available data), while the other parameters were fixed as the settings listed in Table B1. The frequency distributions of simulated O_4 DSCDs ~~at all elevation angles~~ are shown in Fig. B3. ~~The percentage standard deviations of the results are also indicated . The median values of the simulated O_4 DSCDs at each elevation angle are shown as grey dashed lines~~For each elevation angle, the percentage standard deviation is indicated beside the curve, and the gray dashed line shows the median value. The results ~~show that the distributions~~ indicate that the distribution of the simulated O_4 DSCDs ~~at all elevation angles~~ follow the normal distribution, and the ~~simulation uncertainty caused by phase function is larger than that caused by SSA. Similar to the SSA sensitivity analysis, using phase functions from Hohenpeißenberg should not have a significant impact on the aerosol retrieval. Hereafter~~standard deviation at 477 nm is larger comparing to 360 nm.

Based on the simulation results, the phase function with which the simulated O_4 DSCDs at all elevation angles are closest to the median values ~~are used in the forward simulation, and this phase function is denoted as the~~ is chosen as the so-called 'median' phase function ~~.~~ for each wavelength. In our aerosol profile retrieval, the error caused by scattering phase function is also determined using a simple look-up table (see Section 3.7.2).

B4 Sensitivity to aerosols at different altitude

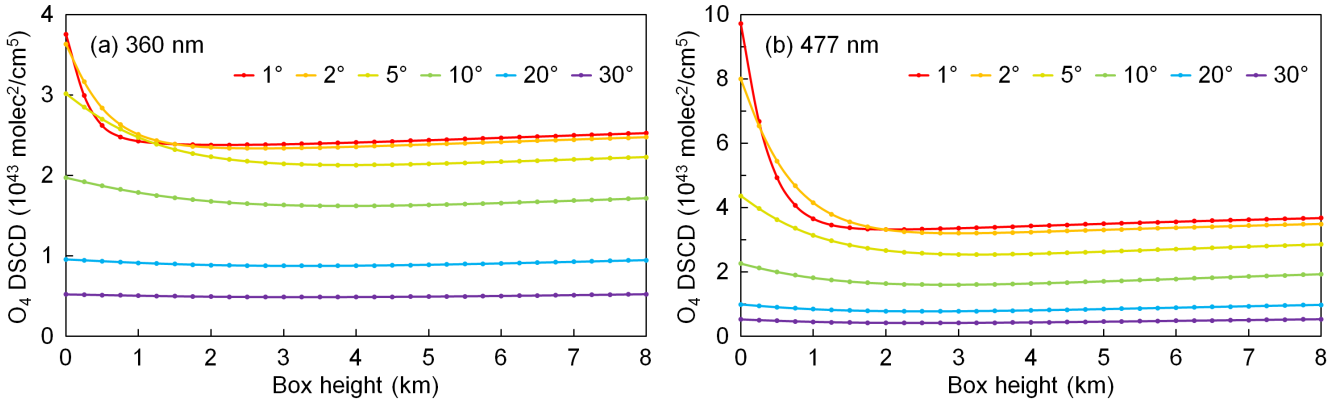

Figure B4. Simulated O_4 DSCDs at (a) 360 nm and (b) 477 nm for box-shape profiles with the same surface aerosol extinction coefficient of 0.04 km^{-1} and different box heights from 0 to 8 km. The other simulation parameters followed the settings listed in Table B1.

The sensitivity of O_4 DSCD to aerosol extinction at different altitude was estimated by simulating O_4 DSCDs with box-shape aerosol profiles with the same aerosol extinction coefficient of 0.04 km^{-1} and different box heights varying from 0 to 8 km. The other parameters were fixed as the settings listed in Table B1. Fig. B4 shows the simulated O_4 DSCDs at 360 and 477 nm for each elevation angle. The result indicates that the sensitivities of O_4 DSCDs at all elevation angles decrease rapidly with increasing box height (and also increasing AOD). Furthermore, O_4 DSCDs at all elevation angles are almost constant when the box height varies between 2 and 8 km, which indicates that O_4 absorption is almost insensitive to the aerosols above

2 km. Take the O_4 DSCD measured at 360 nm with elevation angle of 2° as an example, the sensitivity to aerosols at 2 km is lower than that at surface level by a factor of ∼40. In addition, measurements at lower elevation angles are more sensitive to aerosols close to the surface compared to higher elevations. According to the result, our retrieval of aerosol profiles would only focus on aerosols below 2 km.

This result coincides with the results reported in the MAX-DOAS studies based on the OEM (e.g., Frieß et al., 2006; Clémer et al., 2010; Frieß et al., 2016; Bösch et al., 2018). In these studies, the averaging kernels — which indicate the measurement sensitivity to aerosols at different altitude — are all close to zero at the altitudes above 2 km.

B5 Sensitivity to aerosols above retrieval height

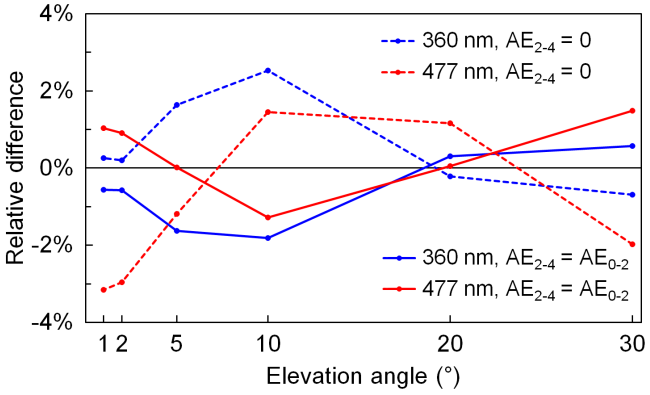

Figure B5. Relative differences of O_4 DSCDs at 360 nm (blue lines) and 477 nm (red lines) simulated with aerosol profiles with AE_{2-4} (aerosol extinction coefficient between 2 and 4 km above instrument) equals to 0% (dashed lines) and 100% (solid lines) of AE_{0-2} (aerosol extinction coefficient between 0 and 2 km above instrument) comparing to the O_4 DSCDs simulated with a profile with $AE_{2-4} = 50\% AE_{0-2}$. For all profiles, $AE_{0-2} = 0.04\ km^{-1}$. The other simulation parameters followed the settings listed in Table B1.

As discussed in Section B4, our aerosol profile retrieval would only focus on aerosols below 2 km. However, as the aerosol load on Zugspitze is usually very low and the aerosol extinction coefficient above 2 km is usually in the same order of magnitude with the one below 2 km. We estimate that the aerosol extinction coefficient between 2 and 4 km (denote as AE_{2-4}) varies from 0% to 100% of the aerosol below 2 km (denote as AE_{0-2}), and the median value is 50% of AE_{0-2}. In order to estimate the sensitivity of O_4 absorption to AE_{2-4}, O_4 DSCDs were simulated with profiles with the same aerosol extinction coefficient below 2 km ($AE_{0-2} = 0.04\ km^{-1}$) and AE_{2-4} equals to 0%, 50% and 100% of AE_{0-2}, and the other parameters were fixed as the settings listed in Table B1. The differences between the O_4 DSCDs simulated with extreme and median AE_{2-4} are shown in Fig. B5. The result indicates that the aerosols above 2 km can affect the O_4 DSCDs by up to ∼3%, which is similar to the surface albedo. Therefore, we consider the influence from the aerosols above 2 km as a kind of measurement uncertainty, and treat it in the same way as the errors caused by surface albedo, single scattering albedo and phase function uncertainties.

Similarly, the uncertainty caused by aerosols above retrieval height is de determined using a simple look-up table in our profile retrieval (see Section 3.7.2).

B6 Sensitivity to surface aerosol extinction

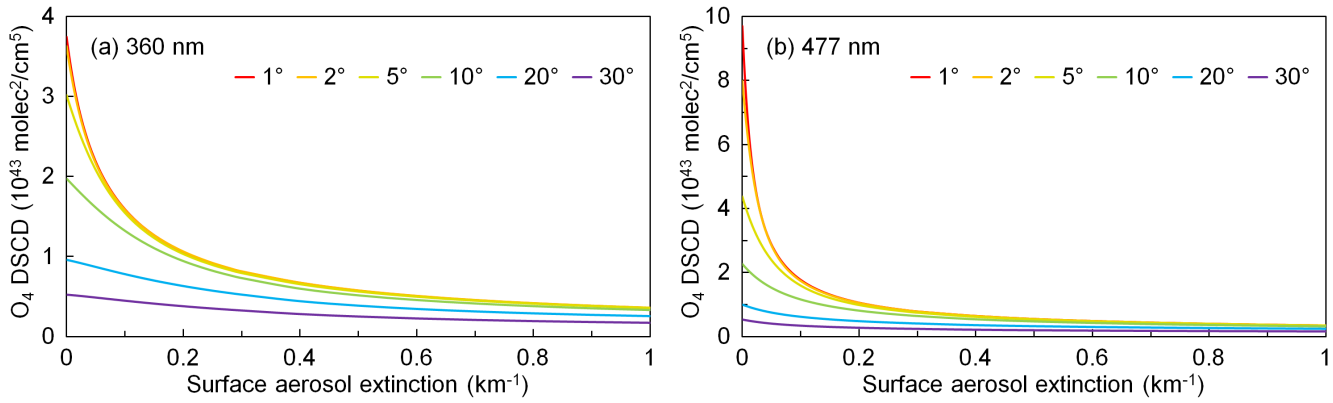

Figure B6. Simulated O_4 DSCDs at (a) 360 nm and (b) 477 nm for box-shape profiles with the same box height of 2 km and different surface aerosol extinction coefficients from 0 to 1 km^{-1}. The other simulation parameters followed the settings listed in Table B1. Note that the curves of 1° and 2° are quite close to each other.

~~The~~ In order to estimate the sensitivity of O_4 DSCD to surface aerosol extinction~~was estimated by forward radiative transfer simulation with box aerosol profiles . The aerosol profiles were parameterized with~~ , O_4 DSCDs were simulated with box-shape profiles with the constant box height of 2 km and aerosol extinction coefficient varies from 0 to 1 km^{-1}. The other ~~simulation settings were the same as those incicated in Section B4. shows the~~ parameters were fixed as the settings listed in Table B1. The simulated O_4 DSCDs ~~for each elevation angle and both (a) 360 nm and (b) 477 nm~~are shown in Fig. B6. The result ~~shows~~ indicates that the sensitivities of O_4 absorption at all elevation angles and both wavelength bands decrease with increasing aerosol extinction. Furthermore, the sensitivity is very low when the surface aerosol extinction coefficient exceeds 0.3 km^{-1}. The O_4 DSCDs at all elevation angles and both wavelengths decrease monotonically with increasing aerosol extinction. In addition, measurements at lower elevation angles are much more sensitive.

Competing interests. The authors declare that they have no conflict of interest.

Acknowledgements. This work is funded by the DLR-DAAD Research Fellowships 2014 (50019750) programme with reference number 91549461. We are thankful for the help from the colleagues of University of Heidelberg in installing the MAX-DOAS instrument at the UFS. We thank Ina Mattis and her colleagues at DWD for their effort in establishing and maintaining the AERONET site in Hohenpeißenberg.

The authors would also like to thank the Royal Belgian Institute for Space Aeronomy (BIRA-IASB) for the provision of the QDOAS software used in this study. We are grateful to Till Rehm and his colleagues at the UFS for the maintenance work. We thank the Bayrisches Umweltminsterium for supporting the UFS as part of their mission.

References

Aliwell, S. R., Roozendael, M. V., Johnston, P. V., Richter, A., Wagner, T., Arlander, D. W., Burrows, J. P., Fish, D. J., Jones, R. L., Tørnkvist, K. K., Lambert, J.-C., Pfeilsticker, K., and Pundt, I.: Analysis for BrO in zenith-sky spectra: An intercomparison exercise for analysis improvement, Journal of Geophysical Research: Atmospheres, 107, ACH 10–1–ACH 10–20, https://doi.org/10.1029/2001JD000329, 2002.

Almeida-Silva, M., Almeida, S. M., Freitas, M. C., Pio, C. A., Nunes, T., and Cardoso, J.: Impact of Sahara Dust Transport on Cape Verde Atmospheric Element Particles, Journal of Toxicology and Environmental Health, Part A, 76, 240–251, https://doi.org/10.1080/15287394.2013.757200, 2013.

Anderson, G. P., Clough, S. A., Kneizys, F., Chetwynd, J. H., and Shettle, E. P.: AFGL atmospheric constituent profiles (0.120 km), Tech. rep., AIR FORCE GEOPHYSICS LAB HANSCOM AFB MA, 1986.

Bäumer, D., Vogel, B., Versick, S., Rinke, R., Möhler, O., and Schnaiter, M.: Relationship of visibility, aerosol optical thickness and aerosol size distribution in an ageing air mass over South-West Germany, Atmospheric Environment, 42, 989 – 998, https://doi.org/https://doi.org/10.1016/j.atmosenv.2007.10.017, http://www.sciencedirect.com/science/article/pii/S1352231007008977, 2008.

Bellouin, N., Boucher, O., Haywood, J., and Reddy, M. S.: Global estimate of aerosol direct radiative forcing from satellite measurements, Nature, 438, 1138–1141, https://doi.org/doi:10.1038/nature04348, 2005.

Bogumil, K., Orphal, J., Homann, T., Voigt, S., Spietz, P., Fleischmann, O., Vogel, A., Hartmann, M., Kromminga, H., Bovensmann, H., Frerick, J., and Burrows, J.: Measurements of molecular absorption spectra with the SCIAMACHY pre-flight model: instrument characterization and reference data for atmospheric remote-sensing in the 230-2380 nm region, Journal of Photochemistry and Photobiology A: Chemistry, 157, 167–184, https://doi.org/http://dx.doi.org/10.1016/S1010-6030(03)00062-5, atmospheric Photochemistry, 2003.

Bösch, T., Rozanov, V., Richter, A., Peters, E., Rozanov, A., Wittrock, F., Merlaud, A., Lampel, J., Schmitt, S., de Haij, M., Berkhout, S., Henzing, B., Apituley, A., den Hoed, M., Vonk, J., Tiefengraber, M., Müller, M., and Burrows, J. P.: BOREAS – a new MAX-DOAS profile retrieval algorithm for aerosols and trace gases, Atmospheric Measurement Techniques, 11, 6833–6859, https://doi.org/10.5194/amt-11-6833-2018, https://www.atmos-meas-tech.net/11/6833/2018/, 2018.

Brook, R. D., Rajagopalan, S., Pope, C. A., Brook, J. R., Bhatnagar, A., Diez-Roux, A. V., Holguin, F., Hong, Y., Luepker, R. V., Mittleman, M. A., Peters, A., Siscovick, D., Smith, S. C., Whitsel, L., and Kaufman, J. D.: Particulate Matter Air Pollution and Cardiovascular Disease, Circulation, 121, 2331–2378, https://doi.org/10.1161/CIR.0b013e3181dbece1, 2010.

Cazorla, A., Casquero-Vera, J. A., Román, R., Guerrero-Rascado, J. L., Toledano, C., Cachorro, V. E., Orza, J. A. G., Cancillo, M. L., Serrano, A., Titos, G., Pandolfi, M., Alastuey, A., Hanrieder, N., and Alados-Arboledas, L.: Near-real-time processing of a ceilometer network assisted with sun-photometer data: monitoring a dust outbreak over the Iberian Peninsula, Atmospheric Chemistry and Physics, 17, 11 861–11 876, https://doi.org/10.5194/acp-17-11861-2017, https://www.atmos-chem-phys.net/17/11861/2017/, 2017.

Chan, K., Wiegner, M., Wenig, M., and Pöhler, D.: Observations of tropospheric aerosols and NO_2 in Hong Kong over 5 years using ground based MAX-DOAS, Science of The Total Environment, https://doi.org/https://doi.org/10.1016/j.scitotenv.2017.10.153, 2017.

Chan, K. L.: Biomass burning sources and their contributions to the local air quality in Hong Kong, Science of The Total Environment, 596-597, 212–221, https://doi.org/https://doi.org/10.1016/j.scitotenv.2017.04.091, 2017.

Chan, K. L. and Chan, K. L.: Aerosol optical depths and their contributing sources in Taiwan, Atmospheric Environment, 148, 364–375, https://doi.org/http://dx.doi.org/10.1016/j.atmosenv.2016.11.011, 2017.

Chan, K. L., Hartl, A., Lam, Y. F., Xie, P. H., Liu, W. Q., Cheung, H. M., Lampel, J., Pöhler, D., Li, A., Xu, J., Zhou, H. J., Ning, Z., and Wenig, M. O.: Observations of tropospheric NO_2 using ground based MAX-DOAS and OMI measurements during the Shanghai World Expo 2010, Atmospheric Environment, 119, 45–58, https://doi.org/http://dx.doi.org/10.1016/j.atmosenv.2015.08.041, 2015.

Chan, K. L., Wiegner, M., Flentje, H., Mattis, I., Wagner, F., Gasteiger, J., and Geiß, A.: Evaluation of ECMWF-IFS (version 41R1) operational model forecasts of aerosol transport by using ceilometer network measurements, Geoscientific Model Development, 11, 3807–3831, https://doi.org/10.5194/gmd-11-3807-2018, 2018.

Chan, K. L., Wang, Z., Ding, A., Heue, K.-P., Shen, Y., Wang, J., Zhang, F., Shi, Y., Hao, N., and Wenig, M.: MAX-DOAS measurements of tropospheric NO_2 and HCHO in Nanjing and a comparison to ozone monitoring instrument observations, Atmospheric Chemistry and Physics, 19, 10 051–10 071, https://doi.org/10.5194/acp-19-10051-2019, https://www.atmos-chem-phys.net/19/10051/2019/, 2019.

Chance, K. and Kurucz, R.: An improved high-resolution solar reference spectrum for earth's atmosphere measurements in the ultraviolet, visible, and near infrared, Journal of Quantitative Spectroscopy and Radiative Transfer, 111, 1289 – 1295, https://doi.org/https://doi.org/10.1016/j.jqsrt.2010.01.036, 2010.

Chance, K. and Orphal, J.: Revised ultraviolet absorption cross sections of H2CO for the HITRAN database, Journal of Quantitative Spectroscopy and Radiative Transfer, 112, 1509 – 1510, https://doi.org/https://doi.org/10.1016/j.jqsrt.2011.02.002, 2011.

Chance, K. V. and Spurr, R. J. D.: Ring effect studies: Rayleigh scattering, including molecular parameters for rotational Raman scattering, and the Fraunhofer spectrum, Appl. Opt., 36, 5224–5230, https://doi.org/10.1364/AO.36.005224, http://ao.osa.org/abstract.cfm?URI=ao-36-21-5224, 1997.

Clémer, K., Van Roozendael, M., Fayt, C., Hendrick, F., Hermans, C., Pinardi, G., Spurr, R., Wang, P., and De Mazière, M.: Multiple wavelength retrieval of tropospheric aerosol optical properties from MAXDOAS measurements in Beijing, Atmospheric Measurement Techniques, 3, 863–878, https://doi.org/10.5194/amt-3-863-2010, 2010.

Deutschmann, T.: Atmospheric radiative transfer modelling with Monte Carlo methods, Institute of environmental physics University of Heidelberg, p. 3935, 2008.

Dubovik, O., Holben, B., Eck, T. F., Smirnov, A., Kaufman, Y. J., King, M. D., Tanré, D., and Slutsker, I.: Variability of Absorption and Optical Properties of Key Aerosol Types Observed in Worldwide Locations, Journal of the Atmospheric Sciences, 59, 590–608, https://doi.org/10.1175/1520-0469(2002)059<0590:VOAAOP>2.0.CO;2, 2002.

Emeis, S., Forkel, R., Junkermann, W., Schäfer, K., Flentje, H., Gilge, S., Fricke, W., Wiegner, M., Freudenthaler, V., Groβ, S., Ries, L., Meinhardt, F., Birmili, W., Münkel, C., Obleitner, F., and Suppan, P.: Measurement and simulation of the 16/17 April 2010 Eyjafjallajökull volcanic ash layer dispersion in the northern Alpine region, Atmospheric Chemistry and Physics, 11, 2689–2701, https://doi.org/10.5194/acp-11-2689-2011, https://www.atmos-chem-phys.net/11/2689/2011/, 2011.

Fernald, F. G.: Analysis of atmospheric lidar observations: some comments, Appl. Opt., 23, 652–653, https://doi.org/10.1364/AO.23.000652, http://ao.osa.org/abstract.cfm?URI=ao-23-5-652, 1984.

Franco, B., Hendrick, F., Van Roozendael, M., Müller, J.-F., Stavrakou, T., Marais, E. A., Bovy, B., Bader, W., Fayt, C., Hermans, C., Lejeune, B., Pinardi, G., Servais, C., and Mahieu, E.: Retrievals of formaldehyde from ground-based FTIR and MAX-DOAS observations at the Jungfraujoch station and comparisons with GEOS-Chem and IMAGES model simulations, Atmospheric Measurement Techniques, 8, 1733–1756, https://doi.org/10.5194/amt-8-1733-2015, https://www.atmos-meas-tech.net/8/1733/2015/, 2015.

Frieß, U., Monks, P. S., Remedios, J. J., Rozanov, A., Sinreich, R., Wagner, T., and Platt, U.: MAX-DOAS O_4 measurements: A new technique to derive information on atmospheric aerosols: 2. Modeling studies, Journal of Geophysical Research: Atmospheres, 111, https://doi.org/10.1029/2005JD006618, 2006.

Frieß, U., Sihler, H., Sander, R., Pöhler, D., Yilmaz, S., and Platt, U.: The vertical distribution of BrO and aerosols in the Arctic: Measurements by active and passive differential optical absorption spectroscopy, Journal of Geophysical Research: Atmospheres, 116, https://doi.org/10.1029/2011JD015938, https://agupubs.onlinelibrary.wiley.com/doi/abs/10.1029/2011JD015938, 2011.

Frieß, U., Klein Baltink, H., Beirle, S., Clémer, K., Hendrick, F., Henzing, B., Irie, H., de Leeuw, G., Li, A., Moerman, M. M., van Roozendael, M., Shaiganfar, R., Wagner, T., Wang, Y., Xie, P., Yilmaz, S., and Zieger, P.: Intercomparison of aerosol extinction profiles retrieved from MAX-DOAS measurements, Atmospheric Measurement Techniques, 9, 3205–3222, https://doi.org/10.5194/amt-9-3205-2016, https://www.atmos-meas-tech.net/9/3205/2016/, 2016.

Gielen, C., Van Roozendael, M., Hendrick, F., Pinardi, G., Vlemmix, T., De Bock, V., De Backer, H., Fayt, C., Hermans, C., Gillotay, D., and Wang, P.: A simple and versatile cloud-screening method for MAX-DOAS retrievals, Atmospheric Measurement Techniques, 7, 3509–3527, https://doi.org/10.5194/amt-7-3509-2014, 2014.

Halla, J. D., Wagner, T., Beirle, S., Brook, J. R., Hayden, K. L., O'Brien, J. M., Ng, A., Majonis, D., Wenig, M. O., and McLaren, R.: Determination of tropospheric vertical columns of NO_2 and aerosol optical properties in a rural setting using MAX-DOAS, Atmospheric Chemistry and Physics, 11, 12 475–12 498, https://doi.org/10.5194/acp-11-12475-2011, 2011.

Hartl, A. and Wenig, M. O.: Regularisation model study for the least-squares retrieval of aerosol extinction time series from UV/VIS MAX-DOAS observations for a ground layer profile parameterisation, Atmospheric Measurement Techniques, 6, 1959–1980, https://doi.org/10.5194/amt-6-1959-2013, 2013.

Haywood, J. and Boucher, O.: Estimates of the direct and indirect radiative forcing due to tropospheric aerosols: A review, Reviews of Geophysics, 38, 513–543, https://doi.org/10.1029/1999RG000078, 2000.

Heald, C. L., Ridley, D. A., Kroll, J. H., Barrett, S. R. H., Cady-Pereira, K. E., Alvarado, M. J., and Holmes, C. D.: Contrasting the direct radiative effect and direct radiative forcing of aerosols, Atmospheric Chemistry and Physics, 14, 5513–5527, https://doi.org/10.5194/acp-14-5513-2014, 2014.

Hendrick, F., Müller, J.-F., Clémer, K., Wang, P., De Mazière, M., Fayt, C., Gielen, C., Hermans, C., Ma, J. Z., Pinardi, G., Stavrakou, T., Vlemmix, T., and Van Roozendael, M.: Four years of ground-based MAX-DOAS observations of HONO and NO_2 in the Beijing area, Atmospheric Chemistry and Physics, 14, 765–781, https://doi.org/10.5194/acp-14-765-2014, 2014.

Hinds, W. C.: Aerosol technology: properties, behavior, and measurement of airborne particles, John Wiley & Sons, 2012.

Holben, B., Eck, T., Slutsker, I., Tanre, D., Buis, J., Setzer, A., Vermote, E., Reagan, J., Kaufman, Y., Nakajima, T., Lavenu, F., Jankowiak, I., and Smirnov, A.: AERONET - A Federated Instrument Network and Data Archive for Aerosol Characterization, Remote Sensing of Environment, 66, 1–16, https://doi.org/http://dx.doi.org/10.1016/S0034-4257(98)00031-5, 1998.

Hönninger, G., von Friedeburg, C., and Platt, U.: Multi axis differential optical absorption spectroscopy (MAX-DOAS), Atmospheric Chemistry and Physics, 4, 231–254, https://doi.org/10.5194/acp-4-231-2004, 2004.

Irie, H., Kanaya, Y., Akimoto, H., Iwabuchi, H., Shimizu, A., and Aoki, K.: First retrieval of tropospheric aerosol profiles using MAX-DOAS and comparison with lidar and sky radiometer measurements, Atmospheric Chemistry and Physics, 8, 341–350, https://doi.org/10.5194/acp-8-341-2008, 2008.

Irie, H., Takashima, H., Kanaya, Y., Boersma, K. F., Gast, L., Wittrock, F., Brunner, D., Zhou, Y., and Van Roozendael, M.: Eight-component retrievals from ground-based MAX-DOAS observations, Atmospheric Measurement Techniques, 4, 1027–1044, https://doi.org/10.5194/amt-4-1027-2011, https://www.atmos-meas-tech.net/4/1027/2011/, 2011.

Irie, H., Nakayama, T., Shimizu, A., Yamazaki, A., Nagai, T., Uchiyama, A., Zaizen, Y., Kagamitani, S., and Matsumi, Y.: Evaluation of MAX-DOAS aerosol retrievals by coincident observations using CRDS, lidar, and sky radiometer inTsukuba, Japan, Atmospheric Measurement Techniques, 8, 2775–2788, https://doi.org/10.5194/amt-8-2775-2015, https://www.atmos-meas-tech.net/8/2775/2015/, 2015.

Jin, J., Ma, J., Lin, W., Zhao, H., Shaiganfar, R., Beirle, S., and Wagner, T.: MAX-DOAS measurements and satellite validation of tropospheric NO_2 and SO_2 vertical column densities at a rural site of North China, Atmospheric Environment, 133, 12–25, https://doi.org/http://dx.doi.org/10.1016/j.atmosenv.2016.03.031, 2016.

Junker, C. and Liousse, C.: A global emission inventory of carbonaceous aerosol from historic records of fossil fuel and biofuel consumption for the period 1860–1997, Atmospheric Chemistry and Physics, 8, 1195–1207, https://doi.org/10.5194/acp-8-1195-2008, https://www.atmos-chem-phys.net/8/1195/2008/, 2008.

Karanasiou, A., Moreno, N., Moreno, T., Viana, M., de Leeuw, F., and Querol, X.: Health effects from Sahara dust episodes in Europe: Literature review and research gaps, Environment International, 47, 107 – 114, https://doi.org/https://doi.org/10.1016/j.envint.2012.06.012, http://www.sciencedirect.com/science/article/pii/S0160412012001390, 2012.

Klett, J. D.: Stable analytical inversion solution for processing lidar returns, Appl. Opt., 20, 211–220, https://doi.org/10.1364/AO.20.000211, http://ao.osa.org/abstract.cfm?URI=ao-20-2-211, 1981.

Kreher, K., Van Roozendael, M., Hendrick, F., Apituley, A., Dimitropoulou, E., Frieß, U., Richter, A., Wagner, T., Abuhassan, N., Ang, L., Anguas, M., Bais, A., Benavent, N., Bösch, T., Bognar, K., Borovski, A., Bruchkouski, I., Cede, A., Chan, K. L., Donner, S., Drosoglou, T., Fayt, C., Finkenzeller, H., Garcia-Nieto, D., Gielen, C., Gómez-Martín, L., Hao, N., Herman, J. R., Hermans, C., Hoque, S., Irie, H., Jin, J., Johnston, P., Khayyam Butt, J., Khokhar, F., Koenig, T. K., Kuhn, J., Kumar, V., Lampel, J., Liu, C., Ma, J., Merlaud, A., Mishra, A. K., Müller, M., Navarro-Comas, M., Ostendorf, M., Pazmino, A., Peters, E., Pinardi, G., Pinharanda, M., Piters, A., Platt, U., Postylyakov, O., Prados-Roman, C., Puentedura, O., Querel, R., Saiz-Lopez, A., Schönhardt, A., Schreier, S. F., Seyler, A., Sinha, V., Spinei, E., Strong, K., Tack, F., Tian, X., Tiefengraber, M., Tirpitz, J.-L., van Gent, J., Volkamer, R., Vrekoussis, M., Wang, S., Wang, Z., Wenig, M., Wittrock, F., Xie, P. H., Xu, J., Yela, M., Zhang, C., and Zhao, X.: Intercomparison of NO_2, O_4, O_3 and HCHO slant column measurements by MAX-DOAS and zenith-sky UV-Visible spectrometers during the CINDI-2 campaign, Atmospheric Measurement Techniques Discussions, 2019, 1–58, https://doi.org/10.5194/amt-2019-157, https://www.atmos-meas-tech-discuss.net/amt-2019-157/, 2019.

Lee, H., Irie, H., Kim, Y. J., Noh, Y., Lee, C., Kim, Y., and Chun, K. J.: Retrieval of Aerosol Extinction in the Lower Troposphere Based on UV MAX-DOAS Measurements, Aerosol Science and Technology, 43, 502–509, https://doi.org/10.1080/02786820902769691, https://doi.org/10.1080/02786820902769691, 2009.

Lee, Y. C., Lam, Y. F., Kuhlmann, G., Wenig, M. O., Chan, K. L., Hartl, A., and Ning, Z.: An integrated approach to identify the biomass burning sources contributing to black carbon episodes in Hong Kong, Atmospheric Environment, 80, 478–487, https://doi.org/http://dx.doi.org/10.1016/j.atmosenv.2013.08.030, 2013.

Levy II, H., Horowitz, L. W., Schwarzkopf, M. D., Ming, Y., Golaz, J.-C., Naik, V., and Ramaswamy, V.: The roles of aerosol direct and indirect effects in past and future climate change, Journal of Geophysical Research: Atmospheres, 118, 4521–4532, https://doi.org/10.1002/jgrd.50192, https://agupubs.onlinelibrary.wiley.com/doi/abs/10.1002/jgrd.50192, 2013.

Li, X., Brauers, T., Shao, M., Garland, R. M., Wagner, T., Deutschmann, T., and Wahner, A.: MAX-DOAS measurements in southern China: retrieval of aerosol extinctions and validation using ground-based in-situ data, Atmospheric Chemistry and Physics, 10, 2079–2089, https://doi.org/10.5194/acp-10-2079-2010, 2010.

Li, X., Brauers, T., Hofzumahaus, A., Lu, K., Li, Y. P., Shao, M., Wagner, T., and Wahner, A.: MAX-DOAS measurements of NO_2, HCHO and CHOCHO at a rural site in Southern China, Atmospheric Chemistry and Physics, 13, 2133–2151, https://doi.org/10.5194/acp-13-2133-2013, 2013.

Li, Z. and Kou, L.: The direct radiative effect of smoke aerosols on atmospheric absorption of visible sunlight, Tellus B, 50, 2011.

Liu, S. C., McKeen, S. A., and Madronich, S.: Effect of anthropogenic aerosols on biologically active ultraviolet radiation, Geophysical Research Letters, 18, 2265–2268, https://doi.org/10.1029/91GL02773, https://agupubs.onlinelibrary.wiley.com/doi/abs/10.1029/91GL02773, 1991.

Ma, J. Z., Beirle, S., Jin, J. L., Shaiganfar, R., Yan, P., and Wagner, T.: Tropospheric NO_2 vertical column densities over Beijing: results of the first three years of ground-based MAX-DOAS measurements (2008-2011) and satellite validation, Atmospheric Chemistry and Physics, 13, 1547–1567, https://doi.org/10.5194/acp-13-1547-2013, 2013.

Pappalardo, G., Amodeo, A., Apituley, A., Comeron, A., Freudenthaler, V., Linné, H., Ansmann, A., Bösenberg, J., D'Amico, G., Mattis, I., Mona, L., Wandinger, U., Amiridis, V., Alados-Arboledas, L., Nicolae, D., and Wiegner, M.: EARLINET: towards an advanced sustainable European aerosol lidar network, Atmospheric Measurement Techniques, 7, 2389–2409, https://doi.org/10.5194/amt-7-2389-2014, https://www.atmos-meas-tech.net/7/2389/2014/, 2014.

Platt, U. and Stutz, J.: Differential optical absorption spectroscopy - principles and applications, Springer, 2008.

Platt, U., Perner, D., and Patz, H. W.: Simultaneous measurement of atmospheric CH_2O, O_3, and NO_2 by differential optical absorption, Journal of Geophysical Research: Oceans, 84, 6329–6335, https://doi.org/10.1029/JC084iC10p06329, 1979.

Risius, S., Xu, H., Di Lorenzo, F., Xi, H., Siebert, H., Shaw, R. A., and Bodenschatz, E.: Schneefernerhaus as a mountain research station for clouds and turbulence, Atmospheric Measurement Techniques, 8, 3209–3218, https://doi.org/10.5194/amt-8-3209-2015, 2015.

Rodgers, C. D.: Inverse methods for atmospheric sounding: Theory and practice, vol. 2, World scientific, 2000.

Rothman, L., Gordon, I., Barber, R., Dothe, H., Gamache, R., Goldman, A., Perevalov, V., Tashkun, S., and Tennyson, J.: HITEMP, the high-temperature molecular spectroscopic database, Journal of Quantitative Spectroscopy and Radiative Transfer, 111, 2139 – 2150, https://doi.org/https://doi.org/10.1016/j.jqsrt.2010.05.001, 2010.

Schäfer, K., Thomas, W., Peters, A., Ries, L., Obleitner, F., Schnelle-Kreis, J., Birmili, W., Diemer, J., Fricke, W., Junkermann, W., Pitz, M., Emeis, S., Forkel, R., Suppan, P., Flentje, H., Gilge, S., Wichmann, H. E., Meinhardt, F., Zimmermann, R., Weinhold, K., Soentgen, J., Münkel, C., Freuer, C., and Cyrys, J.: Influences of the 2010 Eyjafjallajökull volcanic plume on air quality in the northern Alpine region, Atmospheric Chemistry and Physics, 11, 8555–8575, https://doi.org/10.5194/acp-11-8555-2011, https://www.atmos-chem-phys.net/11/8555/2011/, 2011.

Serdyuchenko, A., Gorshelev, V., Weber, M., Chehade, W., and Burrows, J. P.: High spectral resolution ozone absorption cross-sections - Part 2: Temperature dependence, Atmospheric Measurement Techniques, 7, 625–636, https://doi.org/10.5194/amt-7-625-2014, 2014.

Sinreich, R., Merten, A., Molina, L., and Volkamer, R.: Parameterizing radiative transfer to convert MAX-DOAS dSCDs into near-surface box-averaged mixing ratios, Atmospheric Measurement Techniques, 6, 1521–1532, https://doi.org/10.5194/amt-6-1521-2013, https://www.atmos-meas-tech.net/6/1521/2013/, 2013.

Spurr, R.: LIDORT and VLIDORT: linearized pseudo-spherical scalar and vector discrete ordinate radiative transfer models for use in remote sensing retrieval problems, Light scattering reviews, 3, 229–75, 2008.

Spurr, R., Kurosu, T., and Chance, K.: A linearized discrete ordinate radiative transfer model for atmospheric remote-sensing retrieval, Journal of Quantitative Spectroscopy and Radiative Transfer, 68, 689 – 735, https://doi.org/https://doi.org/10.1016/S0022-4073(00)00055-8, http://www.sciencedirect.com/science/article/pii/S0022407300000558, 2001.

Stocker, T. F., Qin, D., Plattner, G.-K., Tignor, M., Allen, S. K., Boschung, J., Nauels, A., Xia, Y., Bex, B., and Midgley, B.: IPCC, 2013: climate change 2013: the physical science basis. Contribution of working group I to the fifth assessment report of the intergovernmental panel on climate change, 2013.

Thalman, R. and Volkamer, R.: Temperature dependent absorption cross-sections of O_2-O_2 collision pairs between 340 and 630 nm and at atmospherically relevant pressure, Phys. Chem. Chem. Phys., 15, 15 371–15 381, https://doi.org/10.1039/C3CP50968K, 2013.

Tirpitz, J.-L., Frieß, U., Hendrick, F., Alberti, C., Allaart, M., Apituley, A., Bais, A., Beirle, S., Berkhout, S., Bognar, K., Bösch, T., Bruchkouski, I., Cede, A., Chan, K. L., den Hoed, M., Donner, S., Drosoglou, T., Fayt, C., Friedrich, M. M., Frumau, A., Gast, L., Gielen, C., Gomez-Martín, L., Hao, N., Hensen, A., Henzing, B., Hermans, C., Jin, J., Kreher, K., Kuhn, J., Lampel, J., Li, A., Liu, C., Liu, H., Ma, J., Merlaud, A., Peters, E., Pinardi, G., Piters, A., Platt, U., Puentedura, O., Richter, A., Schmitt, S., Spinei, E., Stein Zweers, D., Strong, K., Swart, D., Tack, F., Tiefengraber, M., van der Hoff, R., van Roozendael, M., Vlemmix, T., Vonk, J., Wagner, T., Wang, Y., Wang, Z., Wenig, M., Wiegner, M., Wittrock, F., Xie, P., Xing, C., Xu, J., Yela, M., Zhang, C., and Zhao, X.: Intercomparison of MAX-DOAS vertical profile retrieval algorithms: studies on field data from the CINDI-2 campaign, Atmospheric Measurement Techniques Discussions, 2020, 1–49, https://doi.org/10.5194/amt-2019-456, https://www.atmos-meas-tech-discuss.net/amt-2019-456/, 2020.

Toledano, C., Wiegner, M., Garhammer, M., Seefeldner, M., Gasteiger, J., Müller, D., and Koepke, P.: Spectral aerosol optical depth characterization of desert dust during SAMUM 2006, Tellus B, 61, 216–228, https://doi.org/10.1111/j.1600-0889.2008.00382.x, 2009.

Toledano, C., Wiegner, M., Gro, S., Freudenthaler, V., Gasteiger, J., Müller, D., Müller, T., Schladitz, A., Weinzierl, B., Torres, B., et al.: Optical properties of aerosol mixtures derived from sun-sky radiometry during SAMUM-2, Tellus B, 63, 635–648, https://doi.org/10.1111/j.1600-0889.2011.00573.x, https://onlinelibrary.wiley.com/doi/abs/10.1111/j.1600-0889.2011.00573.x, 2011.

Valavanidis, A., Fiotakis, K., and Vlachogianni, T.: Airborne Particulate Matter and Human Health: Toxicological Assessment and Importance of Size and Composition of Particles for Oxidative Damage and Carcinogenic Mechanisms, Journal of Environmental Science and Health, Part C, 26, 339–362, https://doi.org/10.1080/10590500802494538, 2008.

Viana, M., Pey, J., Querol, X., Alastuey, A., de Leeuw, F., and Lükewille, A.: Natural sources of atmospheric aerosols influencing air quality across Europe, Science of The Total Environment, 472, 825 – 833, https://doi.org/https://doi.org/10.1016/j.scitotenv.2013.11.140, http://www.sciencedirect.com/science/article/pii/S0048969713014447, 2014.

Vlemmix, T., Piters, A. J. M., Berkhout, A. J. C., Gast, L. F. L., Wang, P., and Levelt, P. F.: Ability of the MAX-DOAS method to derive profile information for NO_2: can the boundary layer and free troposphere be separated?, Atmospheric Measurement Techniques, 4, 2659–2684, https://doi.org/10.5194/amt-4-2659-2011, https://www.atmos-meas-tech.net/4/2659/2011/, 2011.

Volkamer, R., Spietz, P., Burrows, J., and Platt, U.: High-resolution absorption cross-section of glyoxal in the UV-Vis and IR spectral ranges, Journal of Photochemistry and Photobiology A: Chemistry, 172, 35–46, https://doi.org/http://dx.doi.org/10.1016/j.jphotochem.2004.11.011, 2005.

Wagner, T., Dix, B., Friedeburg, C. v., Fries, U., Sanghavi, S., Sinreich, R., and Platt, U.: MAX-DOAS O_4 measurements: A new technique to derive information on atmospheric aerosols - Principles and information content, Journal of Geophysical Research: Atmospheres, 109, https://doi.org/10.1029/2004JD004904, 2004.

Wagner, T., Burrows, J. P., Deutschmann, T., Dix, B., von Friedeburg, C., Frieß, U., Hendrick, F., Heue, K.-P., Irie, H., Iwabuchi, H., Kanaya, Y., Keller, J., McLinden, C. A., Oetjen, H., Palazzi, E., Petritoli, A., Platt, U., Postylyakov, O., Pukite, J., Richter, A., van Roozendael, M., Rozanov, A., Rozanov, V., Sinreich, R., Sanghavi, S., and Wittrock, F.: Comparison of box-air-mass-factors and radiances for Multiple-Axis Differential Optical Absorption Spectroscopy (MAX-DOAS) geometries calculated from different UV/visible radiative transfer

models, Atmospheric Chemistry and Physics, 7, 1809–1833, https://doi.org/10.5194/acp-7-1809-2007, https://www.atmos-chem-phys.net/7/1809/2007/, 2007.

Wagner, T., Deutschmann, T., and Platt, U.: Determination of aerosol properties from MAX-DOAS observations of the Ring effect, Atmospheric Measurement Techniques, 2, 495–512, https://doi.org/10.5194/amt-2-495-2009, 2009.

Wagner, T., Beirle, S., Brauers, T., Deutschmann, T., Frieß, U., Hak, C., Halla, J. D., Heue, K. P., Junkermann, W., Li, X., Platt, U., and Pundt-Gruber, I.: Inversion of tropospheric profiles of aerosol extinction and HCHO and NO_2 mixing ratios from MAX-DOAS observations in Milano during the summer of 2003 and comparison with independent data sets, Atmospheric Measurement Techniques, 4, 2685–2715, https://doi.org/10.5194/amt-4-2685-2011, https://www.atmos-meas-tech.net/4/2685/2011/, 2011.

Wagner, T., Apituley, A., Beirle, S., Dörner, S., Friess, U., Remmers, J., and Shaiganfar, R.: Cloud detection and classification based on MAX-DOAS observations, Atmospheric Measurement Techniques, 7, 1289–1320, https://doi.org/10.5194/amt-7-1289-2014, 2014.

Wagner, T., Beirle, S., Remmers, J., Shaiganfar, R., and Wang, Y.: Absolute calibration of the colour index and O_4 absorption derived from Multi AXis (MAX-)DOAS measurements and their application to a standardised cloud classification algorithm, Atmospheric Measurement Techniques, 9, 4803–4823, https://doi.org/10.5194/amt-9-4803-2016, 2016.

Wagner, T., Beirle, S., Benavent, N., Bösch, T., Chan, K. L., Donner, S., Dörner, S., Fayt, C., Frieß, U., García-Nieto, D., Gielen, C., González-Bartolome, D., Gomez, L., Hendrick, F., Henzing, B., Jin, J. L., Lampel, J., Ma, J., Mies, K., Navarro, M., Peters, E., Pinardi, G., Puentedura, O., Pukite, J., Remmers, J., Richter, A., Saiz-Lopez, A., Shaiganfar, R., Sihler, H., Van Roozendael, M., Wang, Y., and Yela, M.: Is a scaling factor required to obtain closure between measured and modelled atmospheric O_4 absorptions? – A case study for two days during the MADCAT campaign, Atmospheric Measurement Techniques Discussions, 2018, 1–85, https://doi.org/10.5194/amt-2018-238, https://www.atmos-meas-tech-discuss.net/amt-2018-238/, 2018.

Wagner, T., Beirle, S., Benavent, N., Bösch, T., Chan, K. L., Donner, S., Dörner, S., Fayt, C., Frieß, U., García-Nieto, D., Gielen, C., González-Bartolome, D., Gomez, L., Hendrick, F., Henzing, B., Jin, J. L., Lampel, J., Ma, J., Mies, K., Navarro, M., Peters, E., Pinardi, G., Puentedura, O., Pukite, J., Remmers, J., Richter, A., Saiz-Lopez, A., Shaiganfar, R., Sihler, H., Van Roozendael, M., Wang, Y., and Yela, M.: Is a scaling factor required to obtain closure between measured and modelled atmospheric O_4 absorptions? An assessment of uncertainties of measurements and radiative transfer simulations for 2 selected days during the MAD-CAT campaign, Atmospheric Measurement Techniques, 12, 2745–2817, https://doi.org/10.5194/amt-12-2745-2019, https://www.atmos-meas-tech.net/12/2745/2019/, 2019.

Wang, S., Cuevas, C. A., Frieß, U., and Saiz-Lopez, A.: MAX-DOAS retrieval of aerosol extinction properties in Madrid, Spain, Atmospheric Measurement Techniques, 9, 5089–5101, https://doi.org/10.5194/amt-9-5089-2016, 2016.

Wang, T., Hendrick, F., Wang, P., Tang, G., Clémer, K., Yu, H., Fayt, C., Hermans, C., Gielen, C., Müller, J.-F., Pinardi, G., Theys, N., Brenot, H., and Van Roozendael, M.: Evaluation of tropospheric SO_2 retrieved from MAX-DOAS measurements in Xianghe, China, Atmospheric Chemistry and Physics, 14, 11 149–11 164, https://doi.org/10.5194/acp-14-11149-2014, https://www.atmos-chem-phys.net/14/11149/2014/, 2014a.

Wang, Y., Sartelet, K. N., Bocquet, M., Chazette, P., Sicard, M., D'Amico, G., Léon, J. F., Alados-Arboledas, L., Amodeo, A., Augustin, P., Bach, J., Belegante, L., Binietoglou, I., Bush, X., Comerón, A., Delbarre, H., García-Vízcaino, D., Guerrero-Rascado, J. L., Hervo, M., Iarlori, M., Kokkalis, P., Lange, D., Molero, F., Montoux, N., Muñoz, A., Muñoz, C., Nicolae, D., Papayannis, A., Pappalardo, G., Preissler, J., Rizi, V., Rocadenbosch, F., Sellegri, K., Wagner, F., and Dulac, F.: Assimilation of lidar signals: application to aerosol forecasting in the western Mediterranean basin, Atmospheric Chemistry and Physics, 14, 12 031–12 053, https://doi.org/10.5194/acp-14-12031-2014, https://www.atmos-chem-phys.net/14/12031/2014/, 2014b.

Warren, E., Charlton-Perez, C., Kotthaus, S., Lean, H., Ballard, S., Hopkin, E., and Grimmond, S.: Evaluation of forward-modelled attenuated backscatter using an urban ceilometer network in London under clear-sky conditions, Atmospheric Environment, 191, 532 – 547, https://doi.org/https://doi.org/10.1016/j.atmosenv.2018.04.045, http://www.sciencedirect.com/science/article/pii/S1352231018302760, 2018.

Wiegner, M. and Geiß, A.: Aerosol profiling with the Jenoptik ceilometer CHM15kx, Atmospheric Measurement Techniques, 5, 1953–1964, https://doi.org/10.5194/amt-5-1953-2012, https://www.atmos-meas-tech.net/5/1953/2012/, 2012.

Wiegner, M., Groß, S., Freudenthaler, V., Schnell, F., and Gasteiger, J.: The May/June 2008 Saharan dust event over Munich: Intensive aerosol parameters from lidar measurements, Journal of Geophysical Research: Atmospheres, 116, https://doi.org/10.1029/2011JD016619, d23213, 2011.

Wiegner, M., Madonna, F., Binietoglou, I., Forkel, R., Gasteiger, J., Geiß, A., Pappalardo, G., Schäfer, K., and Thomas, W.: What is the benefit of ceilometers for aerosol remote sensing? An answer from EARLINET, Atmospheric Measurement Techniques, 7, 1979–1997, https://doi.org/10.5194/amt-7-1979-2014, 2014.

Xin, J., Wang, Y., Li, Z., Wang, P., Hao, W. M., Nordgren, B. L., Wang, S., Liu, G., Wang, L., Wen, T., Sun, Y., and Hu, B.: Aerosol optical depth (AOD) and Ångström exponent of aerosols observed by the Chinese Sun Hazemeter Network from August 2004 to September 2005, Journal of Geophysical Research: Atmospheres, 112, https://doi.org/10.1029/2006JD007075, 2007.

Zhang, J., Wang, S., Guo, Y., Zhang, R., Qin, X., Huang, K., Wang, D., Fu, Q., Wang, J., and Zhou, B.: Aerosol vertical profile retrieved from ground-based MAX-DOAS observation and characteristic distribution during wintertime in Shanghai, China, Atmospheric Environment, 192, 193 – 205, https://doi.org/https://doi.org/10.1016/j.atmosenv.2018.08.051, http://www.sciencedirect.com/science/article/pii/S1352231018305727, 2018.

Zhang, Z., Wenig, M., Zhou, W., Diehl, T., Chan, K. L., and Wang, L.: The contribution of different aerosol sources to the Aerosol Optical Depth in Hong Kong, Atmospheric Environment, 83, 145–154, https://doi.org/http://dx.doi.org/10.1016/j.atmosenv.2013.10.047, 2014.